# Growth and Characterization of Epitaxial Al Layers on GaAs and Si Substrates for Superconducting CPW Resonators in Scalable Quantum Computing Systems

by

Julie Tournet

A thesis
presented to the University of Waterloo
in fulfillment of the
thesis requirement for the degree of
Master of Applied Science
in
Electrical and Computer Engineering

Waterloo, Ontario, Canada, 2015

© Julie Tournet 2015

I hereby declare that I am the sole author of this thesis. This is a true copy of the thesis, including any required final revisions, as accepted by my examiners.

I understand that my thesis may be made electronically available to the public.

## Abstract

The growth of Aluminum ($Al$) on semiconductors and dielectrics is a cornerstone in the quest for scalable quantum computing systems. Indeed the electrical properties of $Al$ make it an exceptional candidate for the realization of superconducting resonators, pivotal tools for understanding and operating superconducting qubits. Such resonators have been fabricated recently on Sapphire substrates, using Molecular Beam Epitaxy (MBE), and displayed quality factors above a million. Complementary studies of these resonators have demonstrated that the metal-substrate interface was the primary source of decoherence and losses, highlighting the importance of pristine interfaces (free of contaminants), and high quality epitaxial growth in order to minimize the native defects level. In this work we investigate different substrate materials in order to yield equivalent or higher quality factor resonators. Gallium Arsenide ($GaAs$) and Silicon ($Si$) were selected for their good dielectric properties, well-established processing techniques and a potential on-chip integration. After thermal substrate annealing, and in some cases deposition of a buffer structure, $Al$ was grown on both substrates at low temperature, using MBE. In view of the extreme sensitivity of the resulting $Al$ crystal orientation to the initial surface conditions, different starting surface reconstructions were investigated. Growth evolution was studied with reflection high energy electron diffraction simultaneously at several azimuths during deposition on rotating substrates. The substrate temperature, the system background pressure and possible sources of contamination were monitored carefully to ensure the reproducibility of the results. Resulting layers were subsequently characterized with X-Ray Diffraction (XRD) to confirm their epitaxial nature and crystallographic orientation. Finally, atomic force microscopy was used to assess the layers morphology. Different growth modes were observed depending on the material: $Al$ grew in a Stranski-Krastanov mode on $GaAs(001)$ surfaces, in a Frank-van-der-Merwe mode on $Si(111)$ surfaces and in a Volmer-Weber mode on $Si(001)$ surfaces. All yielded crystalline structures. Targeting atomically smooth single crystalline materials, best results were obtained for $Al(110)$ deposited on $GaAs(001)-(2\times4)$ substrates with surfaces showing Root Mean Square (RMS) roughness of 0.552nm. While the epitaxy on $Si(111)-(\text{“}1\times1\text{”})$ led to single-crystalline $Al(111)$ layers with a RMS roughness of only 0.487nm, a detailed XRD study indicated a possible misalignment of the crystallites that could induce defects in the material. Simi-

larly, epitaxy on $Si(111) - (7 \times 7)$ substrates yielded $Al(111)$ layers of a RMS roughness of 0.519nm that, however, appeared rougher under the Nomarski microscope, likely due to the surface preparation prior to $Al$ deposition. The deposition on $Si(001) - (2 \times 1)$ substrates led to bi-crystals of $Al(110)$ of higher RMS roughness (0.719nm). Finally, the growth on $GaAs(001) - (4 \times 4)$ reconstruction led to polycrystalline materials with mixed $Al(100)$, $Al(110)$ and $Al(111)$ ofRMS roughness 1.20nm. Moreover, the composition of the layers grown on the $GaAs(001) - (4 \times 4)$ reconstruction was inconsistent across multiple growths.

## Acknowledgements

I would like to thank all the people who made this possible. First of all, my supervisor, Dr. Wasilewski, for believing in me in spite of my lack of experience in the domain and always pushing me to give my personal best. I am thankful for him passing on his love of research and MBE. Setting up the lab was a real challenge and I am incredibly grateful for all the hours he spent sharing his knowledge with us. There is probably no better way to learn than being involved in the set-up of a lab, and I realize how lucky I have been to be part of this. Dr. Denise Gosselink deserves a million thanks as well for her incredible help over the past two years. Not only has she been amazingly helpful and knowledgeable in my research, but her life lessons and her moral support have also played a major role in my life as a grad student. The MBE Lab would not be what it is today if she had not been here, overcoming calmly and cheerfully every obstacle on our path. She is a true reference for young engineers. I would also like to thank Dr. Mariantoni for the knowledge and equipment generously provided. I am pleased he introduced me to his research team, making the collaboration on this project possible. His help was not the only contribution from the Institute for Quantum Computing and I would like to acknowledge Dr. Miao and Dr. Deler Langenberg for the hours they dedicated to this project and all the knowledge they were kind enough to offer. I would like to thank the readers of this thesis for the time and effort put into improving it and making it a faithful summary of my work in the MBE Lab. I am deeply grateful to the University of Waterloo and more particularly the department of Electrical and Computer Engineering for offering me the opportunity to pursue my studies in a world-class institution with incredible facilities. Of course, I would like to thank NSERC who funded this research project and all Canadian institutions and persons who made my stay in this country enjoyable and worry-free. Finally I would like to express my appreciation to all the people of Canada who made this such an enriching experience. I am happy I had the opportunity to discover so many different cultures and learn from so many life stories. On top of the scientific knowledge I acquired, this stay was a mind-opener on the challenges our world faces today. I am grateful for all the role models Canada put on my way and have many golden standards to try to live to from this point forward. Finally, I am deeply indebted to my family and friends, and especially my love, Stéphane Labruyère, who supported me through all this and gave me the energy to

achieve my ambitions. I could not have done it without you and I will never thank you enough for believing in me at any times, even the times I wanted to give up. And as a very last thank-you note, I would like to thank the MBE gods for treating me well during this initiating experience!

# Table of Contents

**List of Tables** xi

**List of Figures** xii

**List of Acronyms** xvi

**1 Introduction** 1

1.1 Motivation . . . 1

1.2 Superconducting resonators made by molecular beam epitaxy . . . 2

1.3 Materials choice . . . 5

1.4 Layout of the thesis . . . 6

**2 Background Theory** 7

2.1 Superconducting resonators . . . 7

2.1.1 Lossy media . . . 7

2.1.2 Structure of a microwave Co-Planar Waveguide (CPW) resonator . 8

2.1.3 Evaluating a Co-Planar Waveguide (CPW) resonator performance: the quality factor . . . 11

2.1.4 Components of a CPW resonator . . . 12

2.2 Surface science and epitaxy . . . . . . . . . . 15
2.2.1 Crystals geometry . . . . . . . . . . 15
2.2.2 Surface reconstructions . . . . . . . . . . 18
2.2.3 Growth processes . . . . . . . . . . 22
2.2.4 Growth modes . . . . . . . . . . 24
2.2.5 Heteroepitaxy . . . . . . . . . . 26
2.3 State of the art techniques . . . . . . . . . . 29
2.3.1 Cleaning methods . . . . . . . . . . 29
2.3.2 *Al* epitaxy on *GaAs* substrates . . . . . . . . . . 36
2.3.3 *Al* epitaxy on *Si* substrates . . . . . . . . . . 40

**3 Equipment and techniques** **44**
3.1 Molecular Beam Epitaxy . . . . . . . . . . 44
3.1.1 The need for Ultra-High Vacuum (UHV) . . . . . . . . . . 44
3.1.2 Description of the GEN10 system . . . . . . . . . . 45
3.2 Characterization techniques . . . . . . . . . . 49
3.2.1 *In-situ* metrology . . . . . . . . . . 49
3.2.2 *Ex-situ* metrology . . . . . . . . . . 54
3.3 Experimental procedure . . . . . . . . . . 61
3.3.1 Preparation of the substrates . . . . . . . . . . 61
3.3.2 Thermal cleaning . . . . . . . . . . 61
3.3.3 Buffer layer deposition (case of the *GaAs* wafers) . . . . . . . . . . 64
3.3.4 Cooling down . . . . . . . . . . 64
3.3.5 *Al* epitaxy . . . . . . . . . . 67

**4 Results** **69**

4.1 Preliminary observations . . . . . 69

4.1.1 Study of the wet cleaning techniques . . . . . 69

4.1.2 Effect of the *in-situ* contaminants . . . . . 70

4.2 $Al$ epitaxy on $GaAs$ . . . . . 73

4.2.1 $Al$ epitaxy on $GaAs(001) - (2 \times 4)$ . . . . . 73

4.2.2 $Al$ epitaxy on $GaAs(001) - (4 \times 4)$ . . . . . 84

4.2.3 Other parameters . . . . . 89

4.3 $Al$ epitaxy on $Si$ . . . . . 95

4.3.1 $Al$ epitaxy on $Si(111) - (\text{“}1 \times 1\text{”})$ . . . . . 95

4.3.2 $Al$ epitaxy on $Si(111) - (7 \times 7)$ . . . . . 102

4.3.3 $Al$ epitaxy on $Si(001) - (2 \times 1)$ . . . . . 107

4.3.4 Growth at higher temperature . . . . . 112

**5 Conclusion** **113**

5.1 Summary of findings . . . . . 113

5.2 Future directions of research . . . . . 115

5.2.1 Resonators performance . . . . . 115

5.2.2 Estimation of the sharpness of the interfaces . . . . . 115

5.2.3 Cleaning study . . . . . 116

**APPENDICES** **117**

**A MATLAB Calculator** **118**

**B Miller indices and reciprocal space** **124**

C Ewald sphere and Reflection High Energy Electron Diffraction (RHEED) streaks spacing 128

D XRD Calculator 131

References 135

# List of Tables


1.1 Quality factors of superconducting resonators made by different deposition techniques . . . 5

2.1 Lattice constants . . . 16

2.2 Lattice mismatch between $Al$ and the substrate and thermal expansion coefficients (at room temperature). . . . 26

4.1 Lattice parameters computed from RHEED observations for the epitaxy on $GaAs(001)-(2\times4)$ . . . 76

4.2 Lattice parameters computed from RHEED observations for the epitaxy on $GaAs(001)-(4\times4)$ . . . 86

4.3 Lattice parameters computed from RHEED observations for the epitaxy on $Si(111)-(7\times7)$ . . . 102

4.4 Lattice parameters computed from RHEED observations for the epitaxy on $Si(001)-(2\times1)$ . . . 109

# List of Figures


1.1 Types of materials . . . . . . . . . . . . . . . . . . . . . . . . . . . . 2

1.2 Boundaries in polycrystalline materials . . . . . . . . . . . . . . . . . . . 3

1.3 Interdiffusion phenomenon . . . . . . . . . . . . . . . . . . . . . . . . . 3

2.1 The coplanar waveguide (CPW) structure . . . . . . . . . . . . . . . . . . 9

2.2 Graphical representation of the quality factor . . . . . . . . . . . . . . . . 12

2.3 Face-centered cubic and Zinc-Blende geometry . . . . . . . . . . . . . . . . 17

2.4 Crystallographic planes of the face-centered structure . . . . . . . . . . . . 18

2.5 $Si(001) - (2 \times 1)$ reconstruction . . . . . . . . . . . . . . . . . . . . . . 19

2.6 Surface reconstructions prepared for $Al$ epitaxy on $GaAs(001)$ . . . . . . . 20

2.7 Surface reconstructions prepared for $Al$ epitaxy on $Si(111)$ . . . . . . . . . 21

2.8 Growth processes in epitaxy . . . . . . . . . . . . . . . . . . . . . . . . 22

2.9 The three growth modes of epitaxy . . . . . . . . . . . . . . . . . . . . . 25

2.10 Possible matching of $Al(001)$ on $GaAs(001)$ . . . . . . . . . . . . . . . . 27

2.11 Possible defects in heteroepitaxy . . . . . . . . . . . . . . . . . . . . . . 28

2.12 Thermal expansion coefficients of $Al$, $GaAs$ and $Si$ . . . . . . . . . . . . . 30

2.13 Two-step model for Silicon oxide desorption . . . . . . . . . . . . . . . . . 33

2.14 Observation of the Stranski-Krastanoz growth of $Al$ on $GaAs$ . . . . . . . 38

3.1 Veeco GEN10 Molecular Beam Epitaxy system . . . . . . . . . . . . . . . . 46
3.2 Growth Module . . . . . . . . . . . . . . . . . . . . . . . . . . . . . . . . 48
3.3 Correlation between the RHEED pattern and the surface morphology . . . 51
3.4 RHEED intensity oscillations . . . . . . . . . . . . . . . . . . . . . . . . 52
3.5 BandiT set up . . . . . . . . . . . . . . . . . . . . . . . . . . . . . . . . 53
3.6 XRD principle . . . . . . . . . . . . . . . . . . . . . . . . . . . . . . . . 56
3.7 Ewald sphere and diffraction . . . . . . . . . . . . . . . . . . . . . . . . 56
3.8 XRD set up . . . . . . . . . . . . . . . . . . . . . . . . . . . . . . . . . 58
3.9 AFM set up . . . . . . . . . . . . . . . . . . . . . . . . . . . . . . . . . 60
3.10 Loading of the substrates . . . . . . . . . . . . . . . . . . . . . . . . . . 62
3.11 $Si$ oxide desorption . . . . . . . . . . . . . . . . . . . . . . . . . . . . 63
3.12 $GaAs(001)$ surface reconstructions . . . . . . . . . . . . . . . . . . . . 65
3.13 $Si$ surface reconstructions . . . . . . . . . . . . . . . . . . . . . . . . . 66

4.1 Effect of the *in-situ* contamination on the RHEED pattern . . . . . . . . . 72
4.2 $Al$ nucleation on $GaAs(001) - (2 \times 4)$ observed by RHEED . . . . . . . . . 74
4.3 $Al$ islands coalescence on $GaAs(001) - (2 \times 4)$ observed by RHEED . . . . 75
4.4 $3D$ representation of the $GaAs(001) - (2 \times 4)$ reconstruction . . . . . . . . 76
4.5 $Al(011)$ matching to $GaAs(001)$ . . . . . . . . . . . . . . . . . . . . . . 77
4.6 $Al(100)$ and $Al(110)$ angles . . . . . . . . . . . . . . . . . . . . . . . . 78
4.7 XRD results for $Al/GaAs(001) - 2 \times 4$ epitaxy . . . . . . . . . . . . . . . 80
4.8 $\Phi$ scan . . . . . . . . . . . . . . . . . . . . . . . . . . . . . . . . . . . 81
4.9 Nomarski observations for Al/GaAs-($2 \times 4$) . . . . . . . . . . . . . . . . . 82
4.10 AFM scan of $Al/GaAs(001) - (2 \times 4)$ epitaxy . . . . . . . . . . . . . . . 83

4.11 $3D$ reconstruction of the $Al/GaAs(001)-(2\times 4)$ surface . . . . . . . . . . 83
4.12 $Al$ epitaxy on $GaAs(001)-(4\times 4)$ observed by RHEED . . . . . . . . . . 85
4.13 XRD analysis of $Al$ epitaxy on $GaAs(001)-(4\times 4)$ . . . . . . . . . . . . . 87
4.14 AFM scan of $Al/GaAs(001)-(4\times 4)$ epitaxy . . . . . . . . . . . . . . . . . 87
4.15 Nomarski observations for $Al/GaAs-(4\times 4)$ . . . . . . . . . . . . . . . . . 88
4.16 XRD analysis of $Al$ epitaxy on a simple buffer structure on a $GaAs$ substrate. 89
4.17 Microscope observation of an $Al/Si$ sample grown at 100°C . . . . . . . . . 90
4.18 Intensity profile 1st spot . . . . . . . . . . . . . . . . . . . . . . . . . . . 91
4.19 Intensity profile 2nd spot . . . . . . . . . . . . . . . . . . . . . . . . . . . 92
4.20 Intensity profile lateral spot . . . . . . . . . . . . . . . . . . . . . . . . . 93
4.21 Microscope observation of an $Al/GaAs$ sample grown at 50°C . . . . . . . 94
4.22 $Al$ epitaxy on $Si(111)-(``1\times 1")$ observed by RHEED . . . . . . . . . . . 96
4.23 XRD results for $Al/Si(111)-(``1\times 1")$ epitaxy . . . . . . . . . . . . . . . 98
4.24 XRD results for $Al/Si(111)-(``1\times 1")$ epitaxy . . . . . . . . . . . . . . . 99
4.25 AFM scan of $Al/Si(111)-(``1\times 1")$ epitaxy . . . . . . . . . . . . . . . . . 100
4.26 Nomarski micrographies for $Al/Si(111)-(``1\times 1")$ . . . . . . . . . . . . . 101
4.27 $Al$ epitaxy on $Si(111)-7\times 7$ observed by RHEED . . . . . . . . . . . . . 103
4.28 XRD results for $Al/Si(111)-(7\times 7)$ epitaxy . . . . . . . . . . . . . . . . 104
4.29 AFM scan of $Al/Si(111)-(7\times 7)$ epitaxy . . . . . . . . . . . . . . . . . . 105
4.30 Nomarski observations for $Al/Si(111)-(7\times 7)$ . . . . . . . . . . . . . . . 106
4.31 $Al$ epitaxy on $Si(001)-(2\times 1)$ observed by RHEED . . . . . . . . . . . . 108
4.32 XRD results for $Al/Si(001)-2\times 1$ epitaxy . . . . . . . . . . . . . . . . . 109
4.33 AFM scan of $Al/Si(001)-(2\times 1)$ epitaxy . . . . . . . . . . . . . . . . . . 110
4.34 Nomarski observations for $Al/Si(001)-(2\times 1)$ . . . . . . . . . . . . . . . 111

4.35 Microscope observation of an $Al/Si$ sample grown at 100°C . . . . . . . . . . 112

B.1 Common planes and their Miller indices . . . . . . . . . . . . . . . . . . . . 125

B.2 Reciprocal space basis vectors. . . . . . . . . . . . . . . . . . . . . . . . . . 126

B.3 Cubic reciprocal lattice . . . . . . . . . . . . . . . . . . . . . . . . . . . . . 127

C.1 Ewald sphere for RHEED . . . . . . . . . . . . . . . . . . . . . . . . . . . . 129

# List of Acronyms

**ABES** Absorption Band-Edge Spectroscopy. 51

**AES** Auger Electron Spectroscopy. 37, 41, 68, 115

**AFM** Atomic Force Microscopy. 35, 39, 53, 58, 59, 80, 82, 85, 86, 93, 99, 104, 109

**BET** Band-Edge Thermometry. 51–53, 66

**CPW** Co-Planar Waveguide. 8–12, 117

**CT** Cluster Tool. 45, 46

**DAS** Dimer Adatom Stacking fault. 19

**DIC** Differential Interference Contrast. 53, 57, 80, 85

**GM** Growth Module. 45, 46, 60

**HRXRD** High Resolution X-Ray Diffraction. 53, 54, 78, 85, 103, 106

**ICB** Ionized Cluster Beam. 40

**LL** Load-Lock. 5, 45, 60, 61, 69

**MBE** Molecular Beam Epitaxy. iii, v, vi, 1, 4–6, 26, 36, 40, 41, 43–45, 47–49, 51–53, 69, 93, 112, 115

**ML** monolayer. 16, 37, 41, 42, 44, 49, 72, 76, 80, 83, 101, 106

**PM** Preparation Module. 45, 46

**RGA** Residual Gas Analyzer. 53, 61, 62, 66

**RHEED** Reflection High Energy Electron Diffraction. 36–38, 41, 42, 49, 50, 61–66, 70–72, 74–77, 80, 83–85, 89, 94, 95, 101, 102, 106–109, 112, 113, 127–129

**RMS** Root Mean Square. iii, iv, 42, 80, 85, 99, 104, 109, 112, 113

**SIMS** Secondary Ion Mass Spectrometry. 68, 69

**STM** Scanning Tunneling Microscopy. 42

**TEM** Transmission Electron Microscopy. 36, 39, 49, 93, 114

**TLS** Two-Level System. 15, 85, 93, 114

**UHV** Ultra-High Vacuum. 43, 44, 53, 69

**XPS** X-Ray Photoelectron Spectroscopy. 68, 115

**XRD** X-Ray Diffraction. iii, 39, 54, 56, 72, 79, 83, 85, 88, 93, 94, 96, 97, 103, 106, 108, 111, 113, 130

# Chapter 1

# Introduction

## 1.1 Motivation

Superconducting resonators are vital components of a wide range of micro-electronic devices whose application fields include astronomy and quantum computing. Indeed, they act as radiation detectors from microwave frequencies to gamma rays and can serve as pixels in sub-millimeter wavelength, energy-resolved telescopes [1] [2]. Superconducting microwave resonators are also pivotal in implementing long-lived qubits[1], since they provide a standard to benchmark the considered materials. Moreover, they can act as quantum buses connecting elements between qubits and are a reliable measurement device of a qubit state. Superconducting resonators have therefore become crucial in understanding and operating superconducting qubits.

Superconducting resonators, by their nature, minimize resistive losses. By fabricating them on substrates of low intrinsic loss tangent, such as Sapphire or Silicon [3], one can also reduce the dielectric losses, therefore limiting total energy losses and dissipation. Very recent work have shown Aluminum $Al$ to be the optimal choice for the over-coating metal, provided it is grown by MBE to minimize the amount of native defects [4]. Additional defects are known to stem from impurities at the substrate surface and can enhance unwanted

[1]Quantum bits, units of quantum information, analogous to digital bits in current computing systems.

dissipative and dispersive processes. Wisbey *et al* [5] pointed to the metal-substrate interface as the main source of losses. This justifies the quest for more careful preparation and fabrication processes.

## 1.2 Superconducting resonators made by molecular beam epitaxy

The need for sharp, clean and defect-free interfaces directs the fabrication of the superconducting resonators towards the use of epitaxial techniques. From the Greek roots *epi*, meaning "over" and *taxis*, meaning "an ordered manner", epitaxy refers to the ordered growth of an overlayer in good registry with a substrate. An epitaxial growth yields a well-defined orientation of the epilayers (layers grown by epitaxy) with respect to the starting surface, in opposition to polycrystalline or amorphous materials that do not show any structural long-range order (see Figure 1.1). Single crystalline materials typically display lower levels of defects and a smoother topography. This stems from the fact that, by maintaining the same order (growth orientation) over the whole material, they do not have boundaries between different domains in poor registry where stress or material defects could be created (see Figure 1.2). In addition to the structural defects, the interdiffusion phenomenon (diffusion of bulk atoms into the growing layer or the opposite) is favored in polycrystalline and amorphous materials where the bonding is less regular, leading to less sharp interfaces, as shown in Figure 1.3.

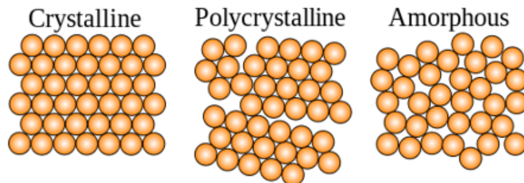


Figure 1.1: The different types of materials: single crystals exhibit short and long-term order, polycrystals exhibit only short term order but no long-term order and amorphous materials exhibit neither short nor long-term order. Source: [6].

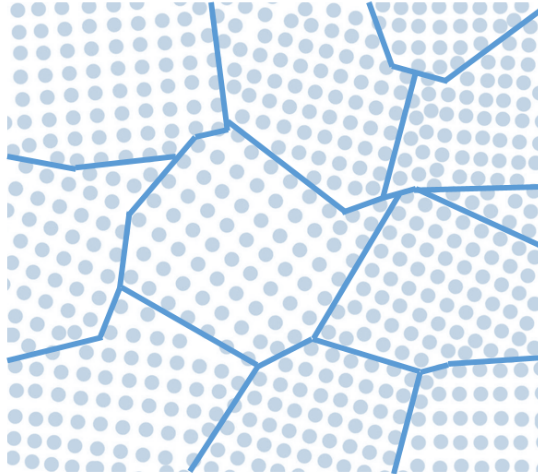

Figure 1.2: Different crystallites (grains) and their grain boundaries (blue solid lines) in a polycrystalline material. Adapted from: [7].

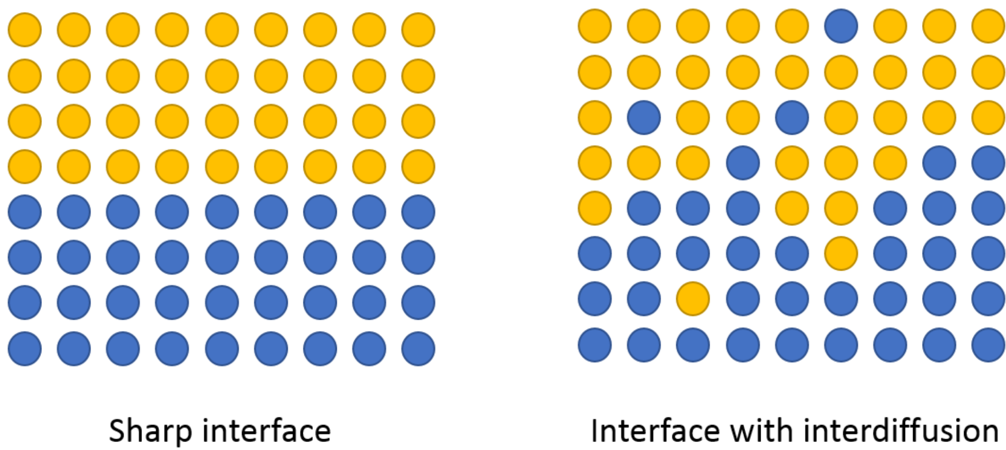


Figure 1.3: Schematics of the interdiffusion phenomenon.

Various epitaxial deposition techniques are available for the fabrication of superconducting resonators. A thorough study by Megrant *et al* [4] demonstrated that, among them, MBE yielded the highest quality factor resonators (see Table 1.1), which is the starting point of this project. MBE is a powerful and versatile technique that allows scientists to grow thin films with extremely high control and precision (thickness, stoichiometry, growth rate). This technique, as the New York Times described it, is roughly like spray-painting a surface slowly with atoms [8]. Sources of ultra-pure elements are heated in effusion cells until the melt surface atoms evaporate. The molecular beam originating from the cell is directed towards the substrate surface where the atoms adsorb in an ultra-high vacuum environment. Its flux (rate of atoms impinging the surface) can be controlled very accurately with the help of shutters and manipulators. This technology allows scientists to grow a crystal, atomic layer by atomic layer and leads to superior crystalline quality, extremely low levels of contamination (and therefore material point defects) and sharp interfaces. MBE creation and development has indeed been pushed forward by the need for fabrication of always smaller and defect-free components. The first MBE systems were developed in parallel at IBM (L. Esaki, R. Tsu and L. Chang) and Bell labs (J. R. Arthur and A. Y. Cho) between 1968 and 1973. Thanks to the unprecedented results demonstrated by both research groups [9] [10] [11], the scientific community grew interest for the technique. Further technological development in the following decades, combined with the integration of many *in-situ* monitoring tools made MBE a technology of choice for the growth of high purity, custom-designed materials with elemental composition precisely controlled from atomic layer to atomic layer. The computerization of the systems further enhanced the level of accuracy and reproducibility of the growth processes, which could not be attained with other technologies. These reasons account for the choice of MBE as the growth technique in this project where the quality and sharpness of the interface is pivotal to the final device performance.

Table 1.1: Sample process information from [4]: $f_0$ is the resonant frequency, $Q_i - H$ and $Q_i - L$ are the internal quality factors at high power and low power, respectively. $O_2$* refers to activated Oxygen generated from a radio frequency plasma source. The Load-Lock (LL) anneal was made at 200°C.

| Process | $f_0$ (GHz) | $Q_i - H \times 10^6$ | $Q_i - L \times 10^6$ |
|---|---|---|---|
| 100 eV $Ar^+$ mill for 2 min and sputter | 3.833 | 4.3 | 0.2 |
| | 6.129 | 4.5 | 0.4 |
| 60 eV $Ar^+$ mill for 10s and E-beam | 3.810 | 9.9 | 0.7 |
| | 6.089 | 4.4 | 0.7 |
| No *in vacuo* cleaning and MBE | 4.973 | 5.7 | 0.5 |
| | 6.120 | 4.3 | 0.8 |
| LL anneal and MBE | 3.773 | 6.6 | 0.8 |
| | 6.125 | 5.4 | 0.8 |
| LL and 850° anneal and MBE | 3.876 | 10.1 | 1.2 |
| | 6.127 | 6.4 | 0.9 |
| LL and 850°C anneal in $O_2$* and MBE | 3.767 | 12.7 | 1.1 |
| | 6.121 | 8.5 | 1.7 |

## 1.3 Materials choice

On top of its importance for electronic interconnects and its application to the processing of nanoscale patterns, *Al* is a superconductor at temperatures below 1.2K. Its other advantages include a good thermal conductivity and its robust native oxide which provides excellent protection to corrosion. *Al* has been proven to be the optimal metallic material for the conducting elements of the resonator [4], therefore other options for these components are not considered herein. On the other hand, the optimal substrate for the resonator, as well as the quality of *Al* epitaxial layers on this substrate, need further research. This thesis focuses on two semiconductors, namely Silicon (*Si*) and Gallium Arsenide (*GaAs*), as alternative substrates to Sapphire for the epitaxial growth of *Al*.

*Si* is the most widely used material in various application fields of nanotechnology,

especially for integrated circuits. It is a readily available and low price substrate of well-established processing techniques. Like *Al*, it has a relatively high thermal conductivity. It is also rather inert, making it a robust structure. Finally, it has a high resistivity and dielectric constant.

*GaAs* is a very technologically important material in photonics, particularly laser diodes, due to its direct bandgap. Its high resistivity (even higher in the case of semi-insulating *GaAs*), high dielectric constant and high electron mobilities made it a pivotal substrate for high performance electronics. It is also nowadays a quite common substrate in MBE owing to the mass production of smartphones in which it is used as a substrate in 50% of the chips fabrication. Finally, the MBE reactor used for this work allowed epitaxy of clean *GaAs* buffers, yielding clean starting surface for *Al* epitaxy. Successful *Al* epitaxy has been realized on both substrates.

## 1.4 Layout of the thesis

This work is part of a joint project between the Waterloo Institute for Nanotechnology and the Institute for Quantum Computing at the University of Waterloo. It endeavors to further improve the three pivotal steps of superconducting resonators conception: first of all select an appropriate substrate; secondly set up the optimal preparation process (cleaning) of the materials; finally optimize the growth conditions to obtain possibly low level of defects (implying the best registry between the metallic phase and the substrate). These steps aim at producing pristine devices and ensure their reproducibility. Chapter 2 presents a brief overview of superconducting resonators, epitaxial growth processes and a state of the art on *Al* epitaxy. Chapter 3 describes the main features of MBE and the associated metrology tools for sample characterization used in this project. The reader will also find the experimental procedures detailed in this chapter. The structural and morphological analysis of the grown *Al* layers are presented in Chapter 4. Finally, in Chapter 5, the findings of this project are summarized, followed by a discussion of future research directions.

# Chapter 2

# Background Theory

This chapter reviews the basics of superconducting resonators, epitaxy as well as state of the art substrate preparation, growth of $Al$ on $GaAs$ and growth of $Al$ on $Si$.

## 2.1 Superconducting resonators

Materials used in quantum circuits are required to be as loss-less and dispersion-less as possible to ensure the fidelity of the information transmission. Resonators provide a standard to benchmark materials for the implementation of long-lived qubits. Their quality factor in particular is a good measurement of the material's ability to transmit a signal optimally. In this section, the structure, components and properties of the application device of the project are presented.

### 2.1.1 Lossy media

Before tackling the resonators structure and properties, this paragraph reviews basic electric properties of the materials. Lossy materials, which are really any "real" material, have a complex permittivity $\epsilon$ whose real part is noted $\epsilon'$ and its imaginary part $\epsilon''$:

$$\epsilon = \epsilon' - j\epsilon'' \tag{2.1}$$

For dielectric materials the real relative permittivity $\epsilon_r$, also known as the dielectric constant, is defined by:

$$\epsilon' = \epsilon_r \epsilon_0 \tag{2.2}$$

where $\epsilon_0$ is the vacuum permittivity. The materials are characterized by their loss tangent $\tan\delta$ which is equal to:

$$\tan\delta = \frac{\omega\epsilon'' + \sigma}{\omega\epsilon'} \tag{2.3}$$

with $\sigma$ the conductivity of the material and $\omega$ the angular frequency. One can then express the complex permittivity in terms of the dielectric constant and the loss tangent:

$$\epsilon = \epsilon_0 \epsilon_r (1 - j\tan\delta) \tag{2.4}$$

### 2.1.2 Structure of a microwave Co-Planar Waveguide (CPW) resonator

While the resonators design and choice of geometry is out of this thesis scope, the following aims at providing the reader with a general understanding of CPW resonators which are a popular choice of structure in quantum electrodynamics. It is largely inspired by the work of Mohebbi and Majedi [12]. A CPW can be considered as a coupled slotline. Only conventional CPW will be presented in this section, but hybrid designs exist, such as Conductor-Backed CPW [13]. A CPW consists of a thin conductor strip where the signal is applied, on top of a dielectric and surrounded by ground planes. The conductor strip and the ground are in the same plane, hence the name "coplanar" waveguide. They are separated by gaps. A conventional CPW structure is shown in Figure 2.1.

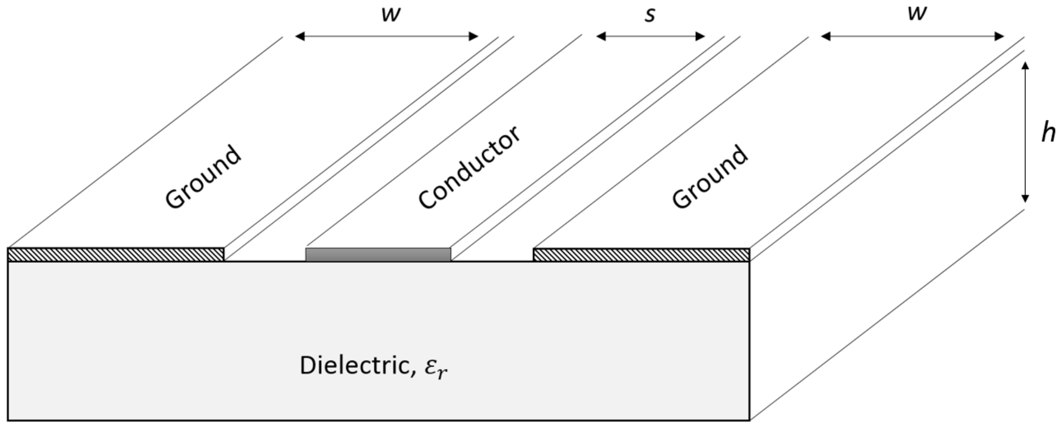


Figure 2.1: Structure of a conventional CPW $w$ is the gap width, $s$ the conductor strip width and $h$ the dielectric thickness.

The quasi-static approximation uses the conformal mapping method to transform the problem geometry for an easier analysis. The structure can indeed be mapped into a parallel plate capacitor filled with a dielectric of effective permittivity $\epsilon_e$, given by:

$$\epsilon_e = 1 + q \times (\epsilon_r - 1) \tag{2.5}$$

with

$$q = \frac{1}{2} \times \frac{K(k_1)K(k_0')}{K(k_1')K(k_0)}$$

where $K(k)$ is the complete elliptical integral of the first kind and the quantities $k_0$, $k_0^rime$, $k_1$ and $k_1'$ are defined by:

$$k_0 = \frac{s}{s + 2w}$$

$$k_0' = \sqrt{1 - k_0^2}$$

$$k_1 = \frac{\sinh\left(\frac{\pi s}{4h}\right)}{\sinh\left(\frac{\pi(s+2w)}{4h}\right)}$$

$$k_1' = \sqrt{1-k_1^2}$$

$q$ is called the filling factor and indicates how much of the electric field penetrates through the substrate. Another rougher approximation is often used:

$$\epsilon_e = \frac{\epsilon_r + 1}{2} \tag{2.6}$$

which represents the case of an infinitely deep substrate ($h \to \infty$). Since only relatively low frequencies (1 to 10GHz) are of interest in this project, the efficient permittivity can be considered independent on the frequency.

Finally, the characteristic impedance is given by:

$$Z_0 = \frac{30\pi}{\sqrt{\epsilon_e}} \frac{K(k_0')}{K(k_0)} \tag{2.7}$$

A CPW has dielectric losses originating from the substrate and conductor losses in the central strip and the ground planes. Dielectric losses are defined by:

$$\alpha_d = \frac{(k_0 \epsilon_r (\epsilon_e - 1) \tan\delta)}{2\sqrt{\epsilon_e}(\epsilon_r - 1)} \tag{2.8}$$

The conductor losses are defined in [14] by:

$$\alpha_c = \frac{R_s\sqrt{\epsilon_e}}{480\pi K(k_0)K(k_0\prime)(1-k_0^2)} \left[\frac{2}{s}\left(\pi + \ln\frac{4\pi s(1-k_0)}{t(1+k_0)}\right) + \frac{1}{w+s/2}\left(\ln\frac{8\pi(w+s/2)(1-k_0)}{t(1+k_0)}\right)\right] \tag{2.9}$$

where $t$ is the thickness of the conductor.

Losses at the interface are discussed in the next section.

### 2.1.3 Evaluating a CPW resonator performance: the quality factor

An important parameter evaluating both loss-less and dispersion-less properties of a resonator is its quality factor $Q$. It is defined as:

$$Q = \frac{\omega \times (time - average\ energy\ stored\ in\ system)}{energy\ loss\ per\ second\ in\ system} \tag{2.10}$$

The energy loss per second corresponds to the power loss of the system. $Q$ characterizes the frequency selectivity of the system and its performance in general. In the vicinity of resonance (*i.e.* $\omega = \omega_0 + \delta\omega$ where $\omega_0$ is the resonance frequency), $Q$ can be approximated by:

$$Q = \frac{1}{2}\frac{\omega_0}{\delta\omega} \tag{2.11}$$

A graphical interpretation of the quality factor is often used. If $Z_in$ is the input impedance of the system, on a plot of $|Z_in|$ in function of $\frac{\omega_0}{\delta\omega}$, the fractional bandwidth ($BW$) is defined as the distance between the curve points where $|Z_in|$ has fallen to 0.707 of its maximum value (see Figure 2.2). $Q$ can then be expressed as:

$$Q = \frac{1}{BW} \tag{2.12}$$

For a superconducting CPW resonator, the quality factor is determined by [16]:

$$Q = \frac{\beta}{2\alpha} \tag{2.13}$$

where the attenuation constant $\alpha$ corresponds to the sum of the attenuation due to dielectric losses in the substrate and the attenuation due to the conductor losses in the strip and the ground planes ($\alpha = \alpha_d + \alpha_c$) defined in 2.9 and 2.8. $\beta$ is the phase constant defined as

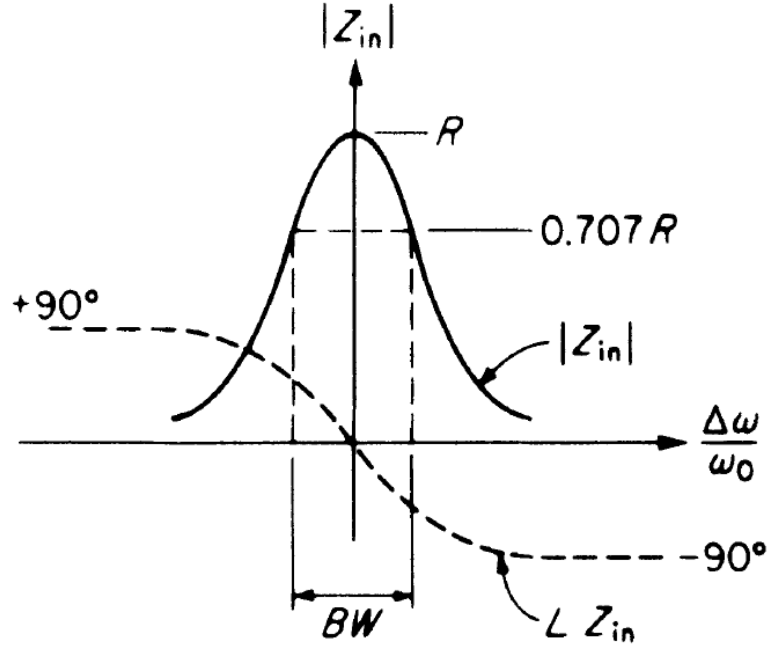


Figure 2.2: Graphical representation of the quality factor for a parallel resonant circuit. Adapted from [15].

$$\beta = \frac{\omega}{c}\sqrt{\epsilon_e}\ rad/m \tag{2.14}$$

with $c$ the velocity of light in vacuum. It can be seen from this approximation that a high quality factor corresponds to a high efficient permittivity hence dielectric constant and to low attenuation.

### 2.1.4 Components of a CPW resonator

#### Superconductors

In the prospect of achieving loss-less resonators, superconducting elements are heavily used in quantum experiments. Superconductivity was discovered in 1911 by Heike Kamerlingh

Onnes. This Dutch physicist realized that, cooled below a certain critical temperature, and using low power input, some materials show zero electrical resistance (infinite conductivity). This phenomenon is very important to microwave and radio frequency engineers since it offers materials with no conductor losses, and suppresses a source of decoherence and errors for the signal. Another reason for the importance of this low temperature and low power regime, is related to the application of the resonators to quantum information processing. Indeed, qubits, the units of quantum information, are typically two-state quantum mechanical systems. They have a ground state and an excited state which define a natural basis in which they can be measured. However, while classical bits can only be in one of the two states (0 and 1), qubits can be in any quantum superposition of the two. Qubits are stable in their ground state as long as they are not provided with an energy sufficient to drive the transition to the excited state. If this transition occurs at a frequency, say, $\nu_{tr} = 6$GHz [17], the energy of transition will be

$$E_{tr} = h\nu_{tr} \tag{2.15}$$

where $h$ is the Planck constant $h = 4.136 \times 10^{-15}$eV·s. This results in a transition energy $E_{tr}$ of $2.482 \times 10^{-5}$eV.

It is therefore important to keep the thermal energy

$$E_{th} = k_B \times T \tag{2.16}$$

with $k_B = 8.617 \times 10^{-5}$eV·K$^{-1}$ the Boltzmann constant and $T$ the absolute temperature in Kelvins, below this critical energy $E_{tr}$ if the signal has to be stable, which sets an upper limit of $T_{max} = 2.880 \times 10^{-1}$K on the temperature. In experiments the temperature used is around 7mK [18] which leaves us well below $T_{max}$. The thermal energy available is therefore too low to change the qubit state. The electrical power provided to the resonator should not add enough energy to the system to drive the transition either.

### High dielectric constant materials

To overcome the dispersion problem, engineers use very high dielectric constant materials such as $Si$ (relative permittivity $\epsilon_{r,Si} = 11.9$), $GaAs$ ($\epsilon_{r,GaAs} = 12.85$) or Sapphire ($\epsilon_{r,Sa} = 11.1$) in the fabrication of resonators. Indeed, the higher the relative permittivity the less significant the change of effective permittivity $\epsilon_e$ with frequency $f$:

$$\epsilon_e(f) = \epsilon_r - \frac{\epsilon_r - \epsilon_e(0)}{1 + G(f)} \tag{2.17}$$

where

$$G(f) = g \times \left(\frac{f}{f_p}\right)^2 \tag{2.18}$$

with

$$g = 0.6 + 0.0009Z_0 \tag{2.19}$$

and

$$f_p = \frac{Z_0}{8\pi h} \tag{2.20}$$

$Z_0$ is the characteristic impedance and $h$ the thickness of the dielectric.

For high relative permittivity values, the first threshold frequency can be computed. Below this frequency, surface wave effects, transverse resonant effects and parallel plate-type waveguide excitation mode effects (all causing dispersion) are negligible. The threshold frequency is 60.782GHz, 58.356GHz, 62.888GHz for $Si$, $GaAs$ and Sapphire, respectively (see Appendix A). These frequencies are much higher than the frequencies used by the resonators (1 to 10GHz) hence we can conclude that parasitic effects and modes will not affect our devices and do not have to be taken into account in the analysis of the materials selected for this project. Finally, it is worth mentioning that high dielectric constant materials tend to confine the field inside the dielectric and minimize radiation outside of the resonator hence show reduced losses, which is another advantage.

**Dielectric losses at low temperature**

As seen in Equation 2.8, dielectric losses are determined by the loss tangent value of the material. While these values are well known for most materials at room temperature, they are poorly known for the low temperatures used for quantum circuits. The most commonly accepted theory is that dielectric losses in superconductors stem from Two-Level System (TLS) that act as spurious two-level microwave resonators [19]. It was first noticed by Martinis that an unexpected dissipation arose in Josephson junction qubits [20] but it has been observed since in other types of qubits [4] [18]. Identifying the TLS and understanding how they function is still a hot topic in research but the use of crystalline over amorphous materials seems to be a good direction for improvement [3]. TLS are believed to originate partly from defects in the material or inter-diffusion of the atoms at the interface (non-abrupt interface). These interface losses are the most important in the superconducting regime and depend on the growth conditions, which explains the focus of this work on the quality of the metal-substrate interface.

## 2.2 Surface science and epitaxy

This section describes the basic concepts of surface science in order to understand the mechanisms of epitaxy and the challenges raised by heteroepitaxy. Extensive treatment of surface physics and chemistry goes beyond the scope of this thesis. There are several excellent textbooks covering this broad field, for instance "Surface Science: Foundations of Catalysis and Nanoscience" by Kolasinski ( [15]), or "Introduction to Surface and Thin Film Processes" by Venables ( [21]).

### 2.2.1 Crystals geometry

A crystal is a homogeneous and well-ordered set of atoms, reproducing to infinite the same basic unit cell. Different types of geometry, called the Bravais lattices, exist and define the structure of the material. The materials considered in this project have a face-centered cubic lattice. $Si$ has a diamond cubic structure and $GaAs$ has a Zinc-Blende structure,

both with a two-atoms basis, as displayed on Figure 2.3. Diamond cubic and Zinc-Blende structures are indeed composed of two face centered cubic lattices, shifted by the vector $\begin{pmatrix} a/4 \\ a/4 \\ a/4 \end{pmatrix}$ where $a$ is the height of the unit cell, also called the lattice parameter.

The lattice parameters of the different materials involved in this project are summarized in Table 2.1:

Table 2.1: Lattice constants

| Material | Lattice constant (Å) |
|---|---|
| Aluminum | 4.0495 |
| Silicon | 5.4309 |
| Gallium Arsenide | 5.6533 |

The symmetrical arrangement of a crystalline lattice leads to the formation of planes of atoms. These planes are defined by Miller indices ($hkl$), which are related by the symmetry of the crystal to its lattice parameters (length and angles). More details on the Miller indices are given in the Appendix B. For the face-centered cubic structure the most important planes are shown in Figure 2.4: the (100) and (111) planes define the surface orientations of the substrates used and all three (100), (111) and (110) planes are observed as crystallographic orientations of the grown $Al$ phases. The density of atoms in a given plane depends on the orientation of the plane and the symmetry of the unit cell. As a result, the thickness of a monolayer (ML), defined as the distance between two adjacent planes, also depends on the Miller indices. The distance between two (100) planes is defined as the lattice parameter $a$ of the material. The distance between two (110) planes, however, equals to $\frac{a\sqrt{2}}{2}$ and the distance between two (111) planes equals to $\frac{a\sqrt{3}}{3}$. This has to be taken into account during the *in-situ* observations.

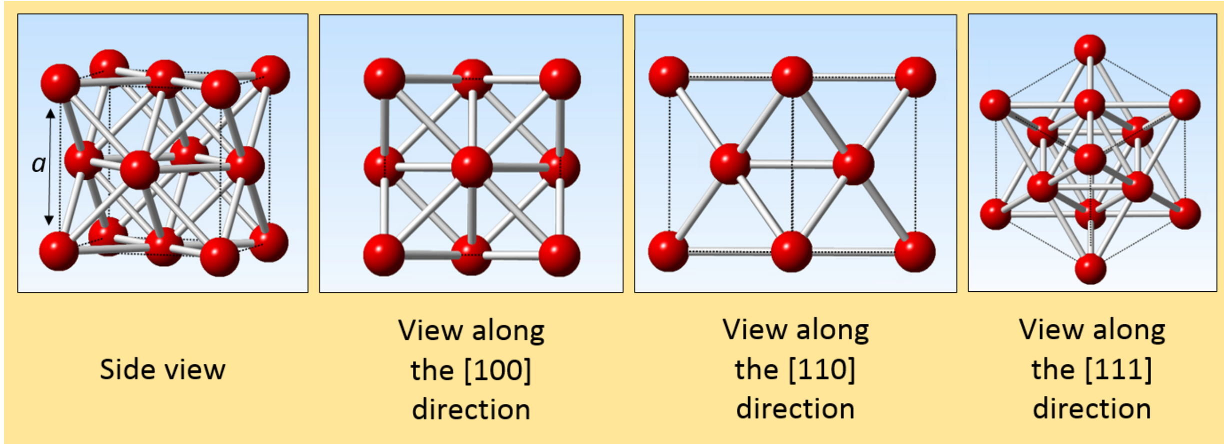


(a)

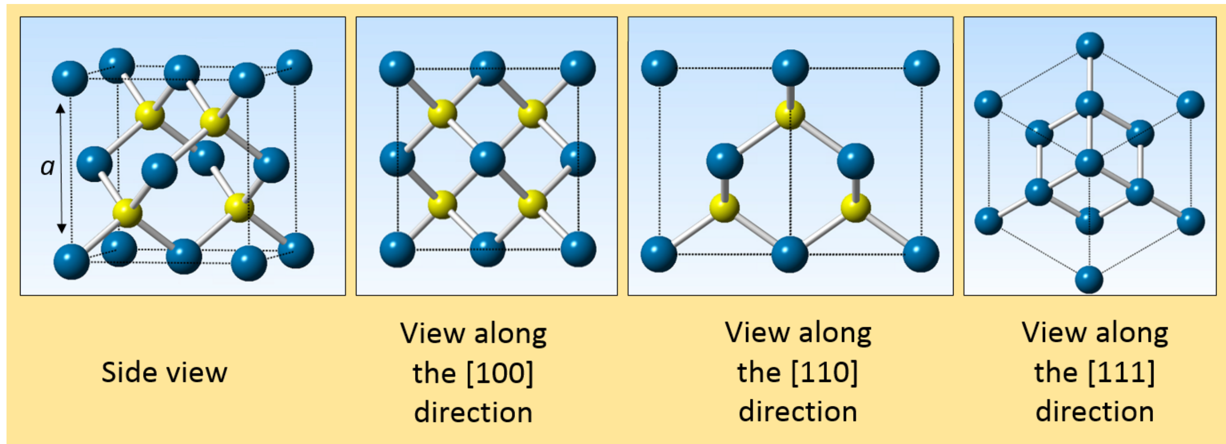


(b)

Figure 2.3: Schema of face-centered cubic (a) and Zinc-Blende (b) structures. The diamond cubic structure is similar to the Zinc-Blende structure but with only one type of atoms, not two different atoms. The distance defined as the lattice parameter is indicated by the letter $a$.

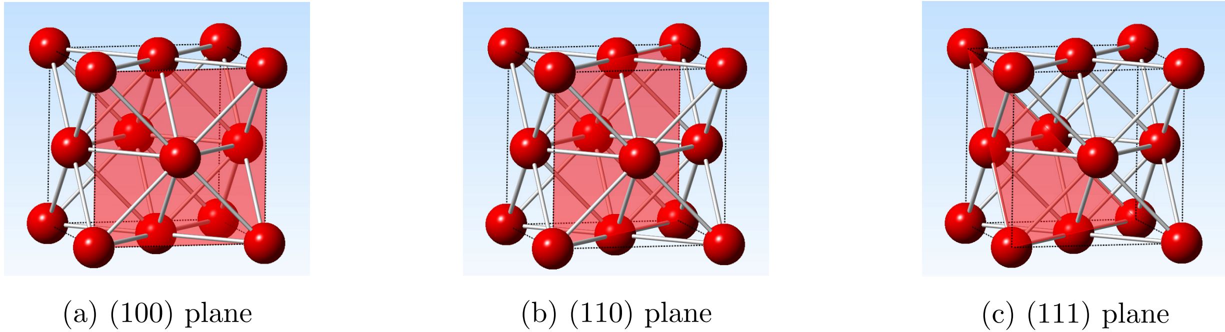

(a) (100) plane (b) (110) plane (c) (111) plane

Figure 2.4: Crystallographic planes of the face centered cubic structure.

### 2.2.2 Surface reconstructions

While bulk structures satisfy all atomic bonding requirements, the formation of a surface leaves the topmost atoms with dangling bonds. In some cases, a modification of the bond length is sufficient to minimize the energy of the surface. However, for most cases, surface atoms need to reorganize the bonding among themselves. This results in a surface arrangement that differs from the crystal bulk structure and is therefore called "reconstruction". This phenomenon happens for most semiconductors. One of the simplest and most studied reconstructions is the $Si(001) - (2 \times 1)$, where the topmost $Si$ atoms group in dimers to leave only one dangling bond by $Si$ atom as shown on Figure 2.5.

The exact atomic configuration of the reconstructed surfaces is a complex problem to solve. Many models exist, determined by simulations and validated by microscopy and diffraction studies. Other reconstructions used in this project are listed in Figure 2.6 and 2.7 below, according to the most accepted models.

$GaAs(001) - (2 \times 4)$ is often referred to as the $As$-stabilized surface while $GaAs(001) - (4 \times 4)$ is an $As$-rich surface, owing to the $As$ coverage in the topmost layers. The $Si(111) - (\text{"}1 \times 1\text{"})$ is an unreconstructed disordered structure, hence the quotation marks. The $Si(111) - (7 \times 7)$, on the other hand, is a remarkable structure which required the combination of multiple instruments (low energy electron diffraction, scanning tunneling microscopy and transmission high energy electron diffraction) to solve [25] [26] and over 25 years of research. The most agreed model, initially proposed by Takayanagi *et al* [25]

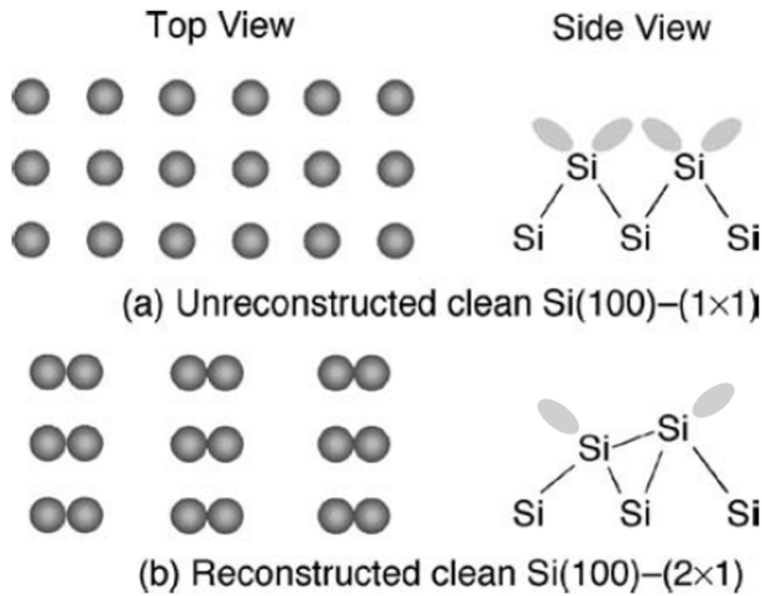


Figure 2.5: $(2 \times 1)$ reconstruction of the $Si(001)$ surface. Adapted from [15].

and finally resolved in real space by Binnig *et al* [26], is called the Dimer Adatom Stacking fault (DAS) model. It contains 12 adatoms[1], 2 triangular sub-units, 9 dimers and a deep corner hole that extends to the fourth and fifth layer of the surface. The structure has also been confirmed by extensive *ab-initio* simulations [27].

[1] Atom that lies on a crystal surface (opposite of a vacancy).

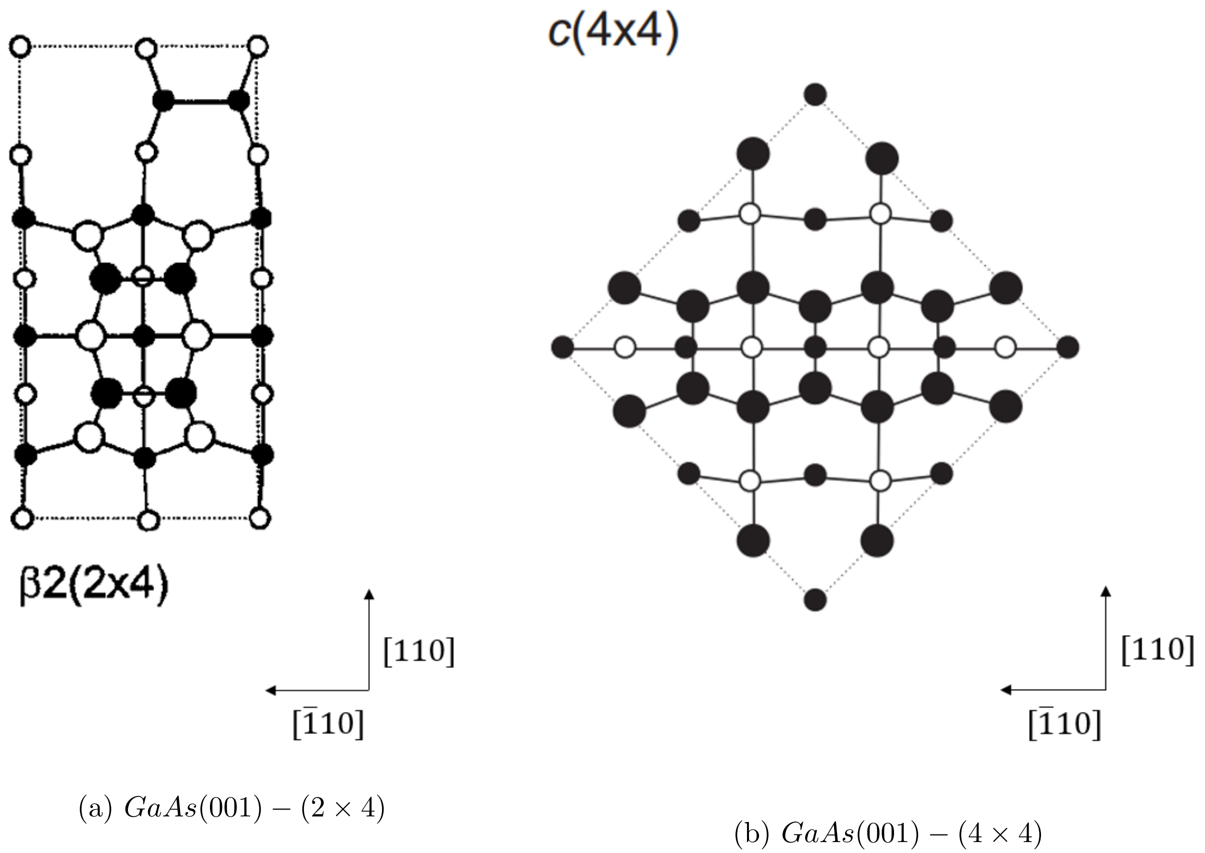


(a) $GaAs(001) - (2 \times 4)$

(b) $GaAs(001) - (4 \times 4)$

Figure 2.6: Top view of the $GaAs(001)$ reconstructed surface configurations prepared for epitaxy. Empty (filled) circles represent $Ga$ ($As$) atoms. Positions in the uppermost two atomic layers are indicated by larger symbols. Adapted from [22].

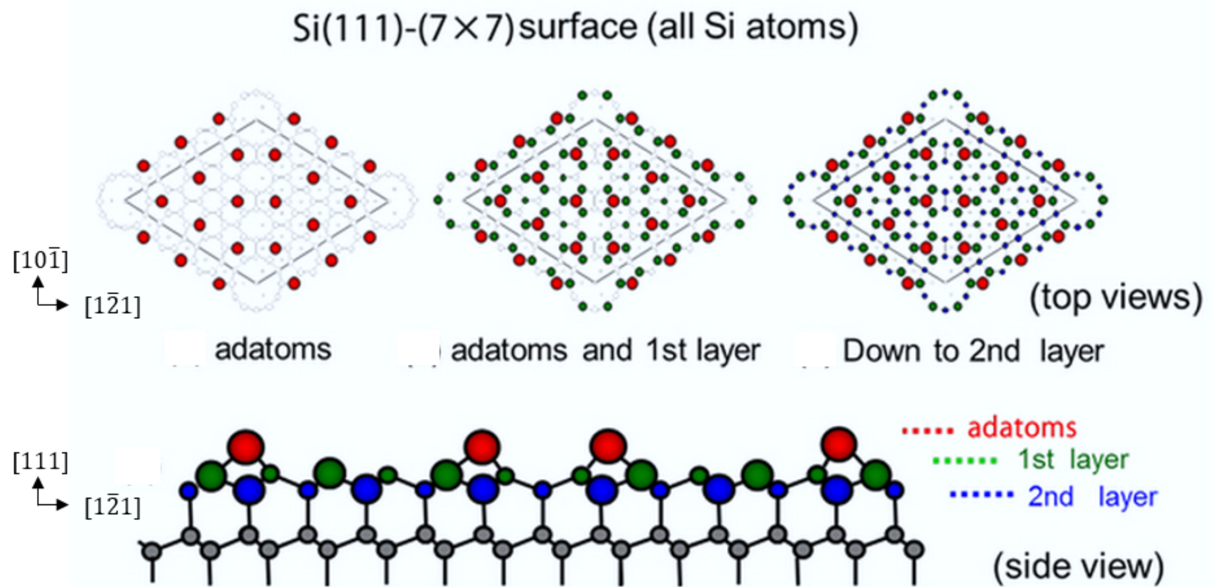


(a) $Si(111) - (7 \times 7)$ adapted from [23].

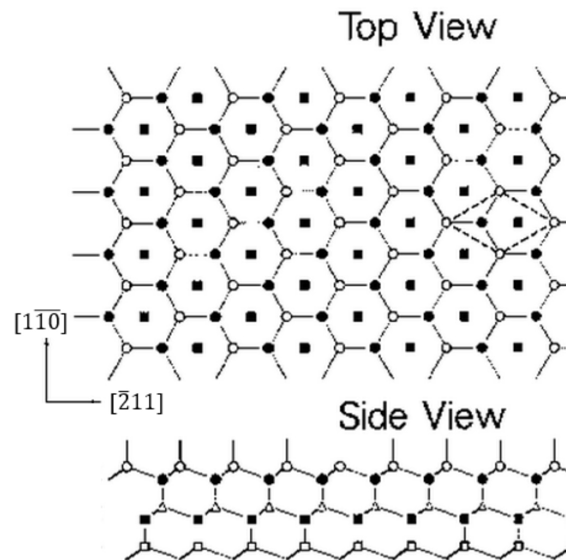


(b) $Si(111) - (\text{“}1 \times 1\text{”})$ adapted from [24].

Figure 2.7: Configurations of the $Si(111)$ reconstructed surfaces prepared for epitaxy.

### 2.2.3 Growth processes

Once vaporized in the growth reactor, the atoms to be deposited are directed at the substrate surface onto which they adsorb and crystallize, forming a film. Four processes are involved at this stage, represented on Figure 2.8.

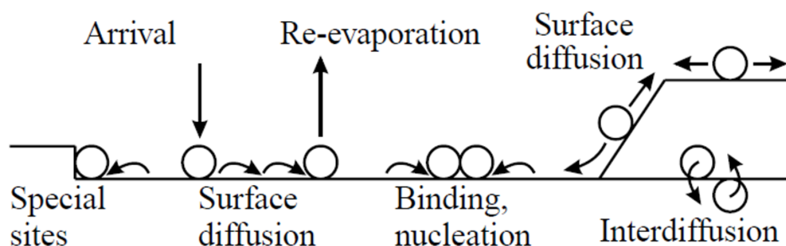


Figure 2.8: Growth processes in epitaxy. Adapted from [21].

First the beam molecule either physisorb or chemisorb on the substrate. This means that the molecule bonds to the surface either by means of Van-der-Waals forces (physisorption) or by electron transfer (chemisorption). Chemisorbed atoms, or chemisorbates, form directional chemical bonds with the substrates. This happens at specific sites such as highest coordination sites[1] in metals, where the energy can be minimized. The grown phase therefore depends strongly on the position of the atoms relative to the substrate. In some cases, chemisorbates can react so strongly with the substrate atoms that it can lead to the formation of new compounds over a few layers at the interface. This happens when the substrate is oxidized for example, when Oxygen atoms can bind to subsurface atoms of the substrate. It could also happen when growing III-type atoms on V-type atoms if a finite III-V phase forms at the interface ($GaAs$ or Aluminum Arsenide ($AlAs$) for example). It involves some diffusion of the substrate atoms into the grown layer (and/or the opposite) and could be enhanced by parameters such as the temperature. Physisorbed atoms, or physisorbates, do not form such directional bonds and attach to the substrate in a more anisotropic way. The interaction with the surface atoms is weaker than for chemisorption

[1] The coordination number of a site can be defined as the number of atoms bonded to the considered site.

and physisorbates may bind to each other more strongly than with the substrate.

Once bonded, the molecule can migrate and dissociate on the surface by diffusion processes. To move between binding sites on the surface, adsorbates have to overcome energy barriers called diffusion barriers. Diffusion is therefore a thermally activated process and can be described by an Arrhenius law

$$D = D_0 \exp \frac{-E_{diff}}{RT} \tag{2.21}$$

where $D$ is the diffusion coefficient, $D_0$ the maximum diffusion coefficient (at infinite temperature) and $E_{diff}$ the activation energy for diffusion. Depending on the growth conditions, diffusion could lead to the formation of flat layers or $3D$ islands of various shapes. In the case of anisotropic diffusion, depending on the surface reconstruction, the grown $3D$ islands do not have a regular but an elongated shape. On the $Si(001) - (2 \times 1)$ for instance, adsorbates move easier along the dimers rows than across them. Diffusion can also be altered by the presence of defects on the surface. On stepped surfaces, diffusion along steps and terraces occur through different mechanisms. Diffusion from one terrace to another, down the step, is governed by higher activation energy since the adsorbates have to move across a region of lower coordination. This energy barrier is known as the Schwoebel barrier. Step up diffusion requires even higher activation energy. Hence, diffusion is favoured along the single terrace. Another diffusion mechanism is the exchange diffusion mechanisms where an adsorbate replaces a surface atom, taking its position in the substrate lattice. This undesirable process is more prevalent for metal-on-metal growth and justifies the decision of not investigating the epitaxy of $Al$ on $Ga$-terminated $GaAs$ substrates.

Finally, adsorbates are eventually incorporated into the crystal lattice or into an existing epilayer. Atoms that do not get incorporated leave the surface by thermal desorption. The growth process kinetics can be appreciated through a set of quantitative parameters such as the arrival rate, the thermal accommodation coefficient and the sticking coefficient of the deposited atoms to the surface.

### 2.2.4 Growth modes

There are three main modes of epitaxial growth possible: in the Frank-Van-der-Merwe the molecules deposit monolayer by monolayer while in the Volmer-Weber growth the crystal grows by forming isolated $3D$ islands that will expand until they connect with other islands. Between these two modes exist the Stranski-Krastanov growth where the reactants first create a few monolayers ("wetting layers") and then islands. The three modes are summarized in Figure 2.9.

In the Frank-Van-der-Merwe mode, adsorbates atoms bind more strongly to the substrate than to each other. They diffuse fast and adsorb on the surface so that they form a complete layer on top of which the incoming atoms will nucleate to form a second complete layer. This process continues until the end of the growth. This growth mode generally minimizes the number of created defects and leads to the highest purity of single-crystalline growth. It is usually observed for close lattice-matching metal-on-metal or semiconductor-on-semiconductor epitaxy. On the contrary, in the Volmer-Weber mode, adsorbates atoms are more strongly attached to each other than to the substrate. Adatoms therefore nucleates in small clusters on the substrate surface. Instead of spreading in a $2D$ plane until forming a complete layer, these clusters grow in $3D$ islands of a condensed phase. Adatoms in this mode usually have a slow diffusion. This mode has been observed principally for the growth of metals on insulators and semiconductors. The Stranski-Krastanov mode, finally, corresponds to the intermediate case where highly strained wetting layers nucleate up to a certain critical thickness, after which the strain has to be relieved by the formation of islands. This growth mode is very common and can result in any perturbation of the monotonic layer-by-layer growth. It also happens in the case of a high lattice mismatch between the grown material and the underlying substrate: the initial grown layers are strained to be in registry with the substrate and, as the thickness increases, the stress increases too. The switch to $3D$ islands growth is then necessary to relax the subsequent layers.

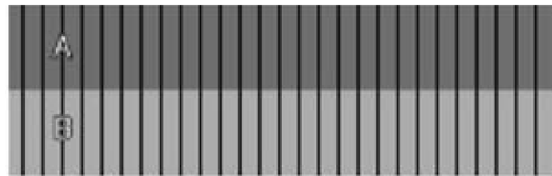


(a) Frank-van der Merwe (FM)

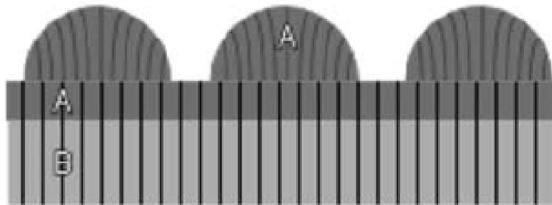


(b) Stranski-Krastanov (SK)

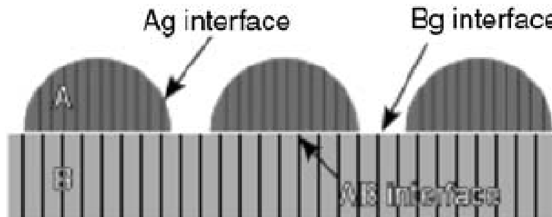


(c) Volmer-Weber (VW)

Figure 2.9: Possible growth modes in the epitaxy of solid overlayer $A$ on solid overlayer $B$ in the presence of gas $g$: (a) layer-by-layer, (b) layer-plus-islands and (c) islands growth. Adapted from [15].

### 2.2.5 Heteroepitaxy

MBE owes part of its success to the capability it offers for growing structures that do not exist in nature and are not easily achievable with other techniques. Such challenge can be presented by heteroepitaxy for instance, which refers to the growth of a sequence of layers of different materials, all in at least partial registry with each other. One obvious difficulty raised by this type of structure is the structural difference of the two materials concerned, possibly leading to bad registry of the overlayer with the substrate. Assuming similar geometries (face-centered cubic for example), a simple assessment of this matching is the direct comparison of the lattice constants. The lattice mismatch parameter is defined in percentage as:

$$\epsilon_0 = \frac{a_{epi} - a_{sub}}{a_{sub}} \times 100 \tag{2.22}$$

where $a_{epi}$ is the lattice constant of the grown material and $a_{sub}$ is the lattice constant of the substrate. The lattice mismatch for $Al$ and $Si$ or $GaAs$ is very high summarized in Table 2.2:

Table 2.2: Lattice mismatch between $Al$ and the substrate and thermal expansion coefficients (at room temperature).

| Substrate material | Lattice mismatch (%) | Thermal expansion coefficient (m/(m·cm)) |
|---|---|---|
| Aluminum | NA | $23.6 \times 10^{-6}$ |
| Silicon | -25.44 | $2.6 \times 10^{-6}$ |
| Gallium Arsenide | -28.37 | $5.7 \times 10^{-6}$ |

In some cases, despite the high misfit, the two structures can find a good arrangement by rotation of the layer lattice with respect to the lattice of the substrate. This is the case for the growth of $Al(100)$ on $GaAs(001)$: the lattice parameters differ by a factor of very nearly $\sqrt{2}$ so a 45° rotation of the $Al(100)$ plane with respect to the $GaAs(001)$ should

accommodate the mismatch (the $Al[100]$ being along the $GaAs[011]$ direction) as shown on Figure 2.10. Another possibility is the arrangement of $X$ atoms from the substrate on $Y$ atoms of the epilayer as described by Zur and McGill in [28]. This could be possible for the growth of $Al(100)$ on $Si(001)$ by stacking 4 $Al$ atoms ($4 \times a_{Al} = 16.1980$Å) on 3 $Si$ atoms ($3 \times a_{Si} = 16.2927$Å). When a good arrangement cannot be achieved while bringing the two surfaces to come into contact, the dangling bonds are highly perturbed and have to relax in some way. If the mismatch is not too high, this can be contained up to a certain so-called critical thickness where the layers are highly strained. Above the critical thickness however, the stress is relaxed through the formation of dislocations and stacking faults so that the crystal could lower its energy (see Figure 2.11).

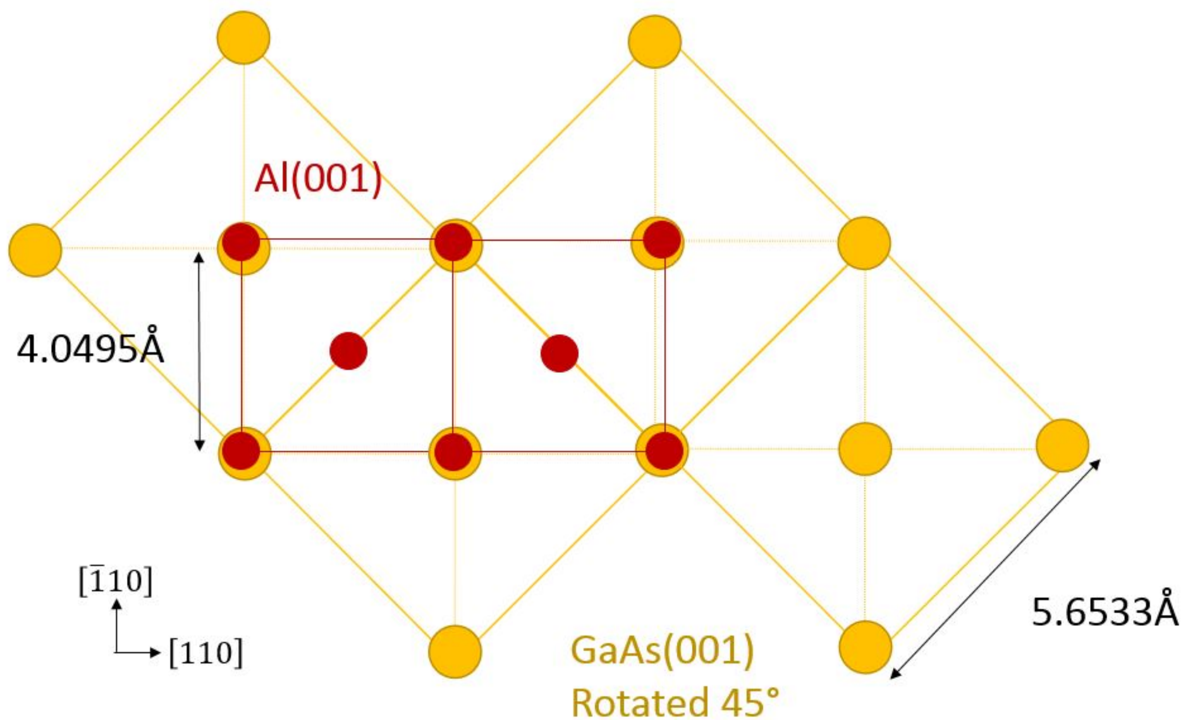


Figure 2.10: Possible matching of $Al(001)$ on $GaAs(001)$. $As$ atoms are in yellow and $Al$ atoms in red.

Interdiffusion is another degradation process which can take place during heteroepi-

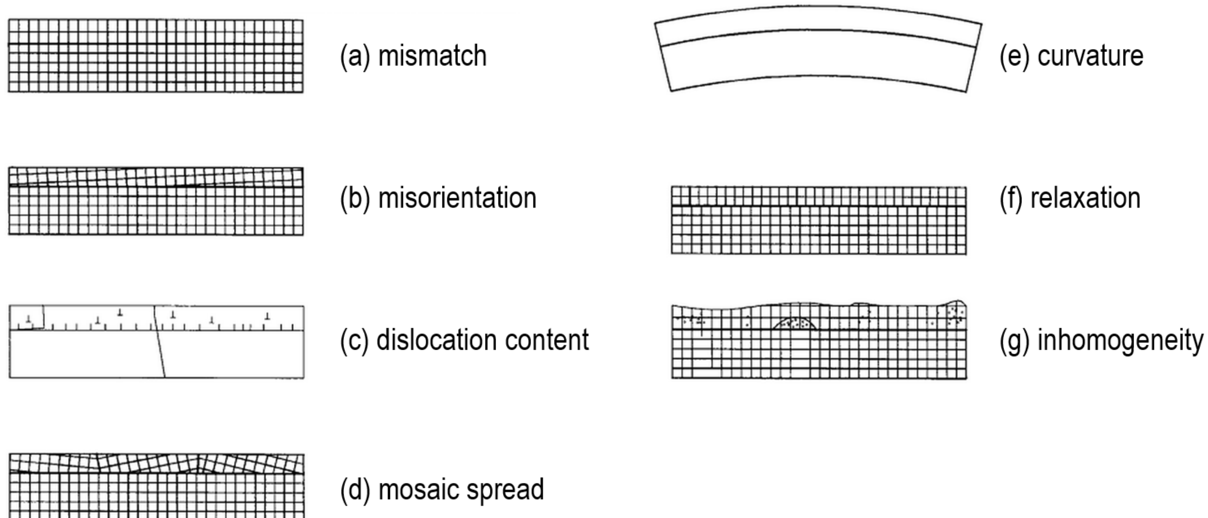


Figure 2.11: Defects created to relieve strained layers in heteroepitaxy. Adapted from [29].

taxy. When depositing a dissimilar material on a substrate, one does not always reach a sharp interface where there is no mixing between the two species. Non-abrupt interfaces where one species diffuse into the other and forms substitutional impurities or interstitial defects can happen under certain growth conditions. Sharp interfaces are desirable in order to minimize the number of defects and unwanted electrical properties that could generate losses in the resonators. Interdiffusion has been observed for $Al$ and $Si$ at $400 - 450°C$, despite the small solubility of $Si$ into $Al$ (0.4% at 400°C) and the non-existing solubility of $Al$ into $Si$ below the eutectic temperature of 577°C [30]. Other parameters must therefore be taken into account. Interdiffusion is encouraged at elevated temperatures [30] which justifies the choice of low temperature growth and no subsequent annealing of the epitaxial layers, even though the literature suggests that annealing could reorient minor phase domains into the dominant phase [31] [32]. It has also been demonstrated that interdiffusion is more likely to happen on disordered starting surfaces [30], such as those obtained after heavy plasma sputtering. These considerations highlight once more the need for clean and properly reconstructed surfaces.

Finally, and even if the heteroepitaxy yielded good registry of the two crystal lattices,

one should anticipate the processing of the wafers posterior to growth. One specific parameter is of paramount importance in this project: the difference in the thermal expansion coefficient of the materials since the resonators will be cooled to $7mK$ for their quality factor measurements. At room temperature, $Al$ has a high thermal expansion coefficient compared to the two substrates: more than 4 times the $GaAs$ coefficient and 9 times the $Si$ coefficient ( 2.2). This could lead to defect formation with the two lattices not compressing at the same rate. The thermal expansion coefficient is also dependent on the temperature and its behavior is shown on Figure 2.12. If all coefficients tend to 0 while approaching the absolute 0 temperature, it can be seen that both semiconductors have a region of negative thermal expansion close to $0K$. This adds further challenge to the cooling procedure.

## 2.3 State of the art techniques

### 2.3.1 Cleaning methods

While $Si$ and $GaAs$ are some of the most widely used substrates in the semiconductor industry, the variety of published works on their pre-growth cleaning reveals the less than perfect efficiency of the proposed methods. To be fair, perfect planar and contaminant-free surfaces are not required in all devices. However, in applications dependent on quantum mechanical effects, the substrate cleaning is of paramount importance to the quality of the final device. Indeed, contaminants can lead to a variety of defects in the material: they can cause stacking faults leading to the formation of dislocations, or block the diffusion of the adatoms on the surface and lead to non-uniform growths (causing dislocations, faceting and all sorts of structural defects). In the case of electrical properties, they can act as donors or acceptors and trap electrons, hindering the expected behavior of the device. The importance of the metal-substrate interface for superconducting resonators has been demonstrated by Wisbey *et al* [5]. This emphasizes the need for pristine starting surfaces. This section focuses on $Si$ cleaning since the deposition system used in this project offers the possibility of growing $GaAs$ buffer layers to bury the native surface and create a clean new one *in-situ*, as will be discussed later. One should note that the contaminants dealt with here are common to any substrate and that many of the quoted techniques can be applied

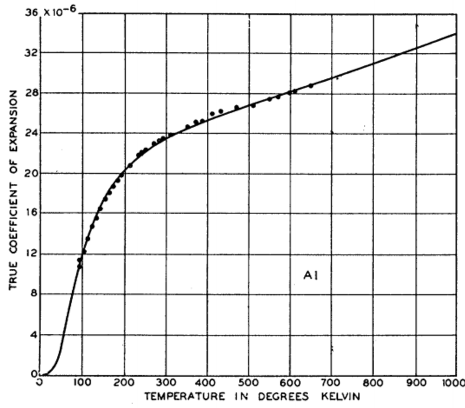


(a) *Al*. Adapted from [33].

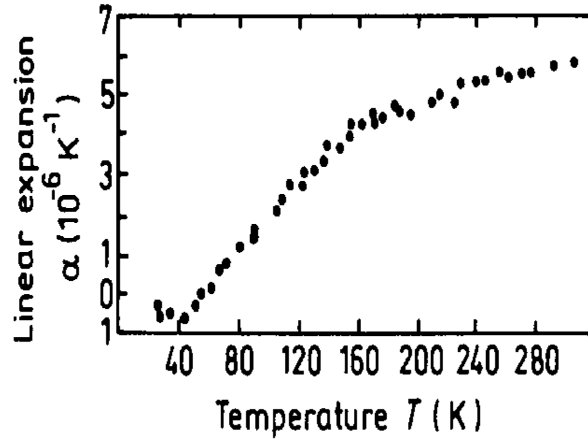


(b) *GaAs*. Adapted from [34].

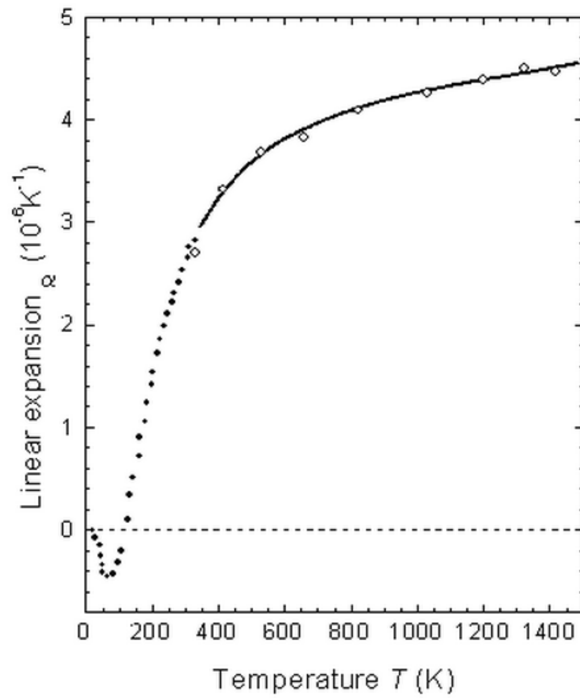


(c) *Si*. Adapted from [35].

Figure 2.12: Linear thermal expansion coefficients of *Al*, *GaAs* and *Si* in $\times 10^{-6}$ $K^{-1}$ versus temperature (K).

to other materials. Finally, choice is made to oppose not wet and dry, neither *ex-situ* and *in-situ* cleaning techniques, as both types complement each other, but rather hydrophilic and hydrophobic treatments. Indeed, they employ different processes and involve different types of contaminants.

Impurities can be present on the substrates in the form of particles, films or adsorbed gases. Nowadays, wafers manufacturing improved significantly and as-delivered epi-ready substrates do not require intense preparation. Material scientists are predominantly concerned with Oxygen ($O$) and Carbon ($C$): oxides are unavoidably created by exposure to air and $C$ likely stems from the use of diamond saws in wafer manufacturing and hydrocarbons floating in the air. Substrates' native oxide can also trap many other impurities and metallic or ionic species are routinely observed in surface analysis. Basic techniques include solvent (methanol or isopropyl alcohol ($IPA$)) or mechanical cleaning by means of brush-scrubbing, fluid jets, or ultrasonic bath. If the former are too light to remove efficiently contaminants, the latter are considered too brutal and often led to wafer damaging or even breaking. Many chemical cleaning processes were developed in the twentieth century but most of them were found to introduce more contaminants than what they were removing. This was true until the introduction in 1970 by Radio Corporation of America of the eponymous cleaning process [36]. The RCA cleaning is comprised of two steps. The first one, named SC-1 consists of dipping the substrate in a solution of deionized (DI) water, ammonium hydroxide ($NH_4OH$) and hydrogen peroxide ($H_2O_2$). It targets organic surface films and some metals such as $Au$, $Ag$, $Cu$, $Ni$, $Cd$, $Zn$, $Co$, $Cr$. It leaves a thin hydrous oxide film on the surface that will be removed subsequently. This oxide, while protecting the substrate from most residues, might trap more metallic impurities. Further decontamination is realized by SC-2, which is a bath of DI water, hydrochloric acid ($HCl$) and $H_2O_2$. SC-2 removes the alkali ions and the rest of the metallic impurities. This process, provided that the wafer is rinsed, dried and manipulated properly (with ultra-clean equipment), leaves a clean oxide layer on the surface that should protect it from re-contamination if loaded into the growth system rapidly. Rinsing should be done with ultra-filtered DI water of resistivity equal or superior to $18M\Omega \cdot cm$. As for drying, evaporation should be avoided in favor of physical removal of solvents such as in spinning or blowing with Nitrogen [37]. To further improve the quality, many scientists

add a preliminary degrease step in an ultrasonic bath of trichloroethylene, acetone and methanol. To ensure the formation of a clean oxide layer and provide deeper cleaning, wet RCA can be supplemented with a dry UV/Ozone cleaning [38]. This technique uses short wavelength UV light to excite and/or dissociate contaminant molecules into ions, free radicals, excited or neutral molecules. Also absorbed by the present di-oxygen ($O_2$), it produces atomic $O$ and ozone ($O_3$) which react with the contaminant molecules to produce volatile compounds such as $CO_2$, $H_2O$ and $N_2$. UV/Ozone alone is not able to remove non-organic contaminants such as dust and thick films, which is why it should be applied only to pre-cleaned surfaces. A few minutes of exposure have proven to be sufficient to produce clean surfaces. Prolonged exposure leads to the formation of an enhanced (thicker and cleaner) protective oxide layer on the surface. An alternative to the RCA process is the Ishizaka-Shiraki method [39] consisting of boiling $HNO_3$ and $NH_4OH : H_2O_2 : H_3O$ baths interspersed with $HF$ (Hydrofluoric acid) dips and a final boiling acid treatment ($HCl : H_2O_2 : H_2O$) to remove ionic and metallic contaminants and form a passivating film.

The aforementioned three techniques lead to hydrophilic surfaces, covered by an oxide possibly containing trapped impurities. Desorbing this oxide in vacuum, along with its contaminants, should therefore provide clean exposed $Si$ surfaces. Lander and Morrison [40] proved that this was possible at temperatures between 800°C and 1000°C. The deoxidation process was studied in detail by Kasper et al [41]. They showed that the first step of the process is the formation of $SiO$ at the interface following reaction as in Equation 2.23

$$SiO_2 + Si \rightarrow SiO \tag{2.23}$$

$SiO$ diffuses to the surface and desorbs. At thin oxide regions or enhanced-diffusion areas, desorption creates holes. The second step of the process is the formation and desorption of $SiO$ at the rim of these holes where no volume diffusion is required. The combined steps lead to the formation of flat depressions, exposing a clean but rough $Si$ surface. A summary of this process is presented in Figure 2.13. The authors showed successful desorption of both $O$ and $C$ between 860°C and 900°C. However they pointed out that residual boron ($B$) did not desorb with the oxide and stuck to the surface. Miki et al [42] showed

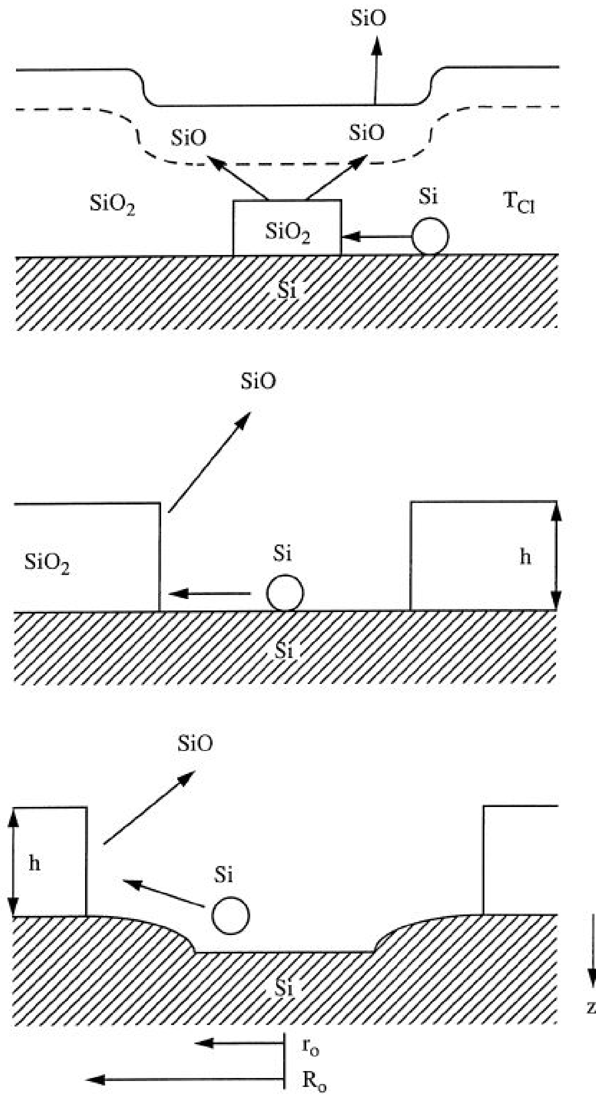


Figure 2.13: Two step model for Silicon oxide desorption. Adapted from [41].

the same year that $B$ contamination was inseparable from the oxide formation and could be worsened by the use of certain materials in the system (Pyrex, Quartz viewports). $B$ contamination does not occur on oxide-free surfaces, likely due to the high affinity of $B$ for $O$. The surface roughness and $B$ presence explains the search for alternative surface cleaning procedure. Another proposed method for oxide desorption is the use of atomic fluxes such as Gallium ($Ga$) [43], Indium ($In$) [44] or $Si$ [45]. The impinging species would react with the oxygen present in the oxide layer to form their own oxide and desorb. It was suggested that potential residual $Ga$ or $In$ particles could further be removed by mere evaporation but it was never proved that all particles can be remove in this way. Droplets formation and particle diffusion into the bulk, although not yet reported, should be considered as a possible consequence of such methods. In the case of $Si$ however, this would not cause any issue. Moreover, by reacting with the external $Si$ instead of the wafer $Si$, the oxide desorption would lead to a smoother surface. This was proven to be possible with very low $Si$ fluxes ($2.5 \times 10^{11}/(\text{cm}^2{\cdot}\text{s})$) by Castagne et al [45].

Hydrophobic surfaces, which are H-terminated, can be formed by dips in hydrofluoric acid ($HF$) or use of $H$-plasma. $HF$ dip is also referred to as oxide stripping as a few minutes suffice to expose the substrate. As $HF$ cannot by itself remove all contaminants, it has to be used on high purity materials or pre-cleaned substrates. It is often used between RCA SC-1 and SC-2. $HF$ leaves a monolayer (or bilayer depending on the wafer orientation) of $H$ on the surface, reducing the sticking coefficient of $O$ and other contaminants to it [46]. However, care should be taken as to the concentration of the $HF$ solution since this technique tends to induce fluorine contamination. It has been shown that $HF$ dip retards the re-oxidation of the surface in ambient air to a rate of 0.17nm/h [47]. Immediate loading to the deposition system should therefore guarantee an oxide-free sample. Another popular technique for $H$-passivation is the exposure of the wafer to an $H$-plasma. This has been extensively studied by Ramm *et al* [48] [49]. Its major advantage is the possibility of being realized in vacuum, avoiding any contact with ambient air (the major source of contamination). $H$-plasma cleaning takes advantages of three phenomena: the physical removal of contaminants by sputtering (transfer of momentum from the impacting molecules to the surface impurities), the chemical reactions between the excited plasma molecules and the film contaminants to form volatile compounds such as $Si-H$ complexes

or hydrocarbons, and finally the heating by impingement enhancing the desorption from the surface. Potential drawbacks of this technique are the incorporation of $H$ (because of the high discharge current and long exposure) as well as possible roughening of the surface by impingement.

The last two techniques described above generate hydrophobic surfaces where a $H$-passivated film remains to be desorbed before growth to expose the bare wafer. Advantageously, this type of film can be desorbed at much lower temperature than oxide films [50]. A few minutes of annealing at 500°C is sufficient, while oxide desorption requires a minimum of 800°C. Other than the convenience aspect and the equipment preservation, keeping the substrate under high temperatures prevents the formation of stable $SiC$ and its diffusion into the bulk [50]. It also avoids other contaminants diffusion as well as the formation of dislocations and stacking faults due to thermal expansion and strain. Finally, above 900°C, direct $Si$ desorption occurs, roughening further the surface [41]. These reasons rule out pre-70s popular thermal flashes where substrates were cleaned by rapid heating up to 1200°C. A comparative atomic force microscopy Atomic Force Microscopy (AFM) study by Sobanska *et al* [51] confirmed that $H$-passivated surfaces annealed at 750°C were smoother than RCA-treated surfaces annealed at 950°C for oxide desorption. The latter displayed islands at its surface, believed to be formed of residual contaminants.

Very recent works propose to combine the strengths of both oxide and $H$-passivation, taking advantages of the self-etching $Si$ oxidation process. Madiomanana *et al* [47] studied cycles of $O_2$ plasma exposure and $HF$ dips. The former removes hydrocarbons and any contaminants trapped in the oxide layer while the latter creates a controlled oxide film on the surface, capturing residual impurities without adding external contaminants. By repeating the process several times, and because $O$ diffuses into $Si$ to create the oxide, the interface moves deeper into the substrate where impurities had not been previously exposed to cleaning. This allows the removal of contaminants that could be buried in the superficial layers of the wafer. The authors showed that 2 cycles were enough to obtain high quality surfaces. The plasma oxidation could be replaced by chemical or thermal oxidation, however plasma seems to have a better efficiency. It was shown that the superficial layer thickness left by $HF$ decreased with an increasing number of cycles, making it easier to desorb once in the growth system. A short annealing at 800°C formed smooth surfaces

with a lower dislocations density. Long anneal times, on the other hand, led to a re-contamination of the surface with contaminants provenient from the hot sources enclosed in the system (cells, viewports, etc).

### 2.3.2 *Al* epitaxy on *GaAs* substrates

The invention of the MBE technique in the late 1960s enabled a dramatic increase in the fabrication quality of electronic components. Preventing atmospheric contamination, hence the introduction of defects, allowing a better control of doping and sub-atomic layer precision in the structures growth, MBE soon became a popular fabrication method, for example, of junction diodes. In this perspective, the MBE growth of *Al* on *GaAs* was investigated in the early seventies in a superposition of metallic and semiconductor layers. [52] From a lattice matching point of view, since the constants differ by a factor of nearly $\sqrt{2}$, it was expected that Al(100) would grow on GaAs(001) with a 45° rotation. However, the authors suggested that the (100) growth mode might not be energetically favored because the face-centered *Al* atom cannot be properly accommodated. For temperatures ranging from 50°C to 500°C, *Al*(110) proved to be the dominant growth orientation. Reflection High Energy Electron Diffraction (RHEED) observations showed that the (110) phase took over the initially concurrent (100) phase after a growth of approximately 25Å. However, the final texture of the material was not quantified and, while the authors speculated that the 1000Åthick film was likely smoother than the starting clean *GaAs* surface, no detailed morphology study was ever reported. For elevated temperatures (400°C), this was confirmed by Landgren *et al* in 1982 [53]. However, a more recent work contradicted this result reporting a (100) dominant phase or (100) + (110) mixed phase structures [31]. Epitaxy closer to room temperature (15 to 50°C) was also investigated extensively [53] [54] [55] [56] and led to a mixture of (100) + (110) phases with possibly very strong texture. The case of the (100) dominant growth mode was studied in details by Missous *et al* [56]: using an initially low growth rate to study nucleation, they showed that *Al* nuclei with a (100) and two non-equivalent (110) orientations appeared and persisted up to about 400Å, after which the *Al*(100) took over. The final (100) single crystalline phase was rotated 45° off the *GaAs* lattice and was in close registry with it. Although the final RHEED pattern

exhibited sharp streaks in the $(1\bar{1}0)$ and $(110)$ azimuths without extra diffraction spots, Transmission Electron Microscopy (TEM) analysis revealed that about 10% of the sample had a (110) orientation. Annealing of the wafer after the growth has been shown to lead to the reorientation of the non-dominant phase into the dominant phase [31]. This process, however, induced inter-diffusion and formation of $AlAs$ at the $Al/GaAs$ interface. In all cases, it seems that room and higher temperature lead to the nucleation of different orientations whose coexistence at the interface could create defects and boundaries, undesired for the resonators.

While most of the aforementioned reports refer to an initial complex RHEED pattern resulting from multiple growth orientations, only few [57] [53] [58] explicitly mention an initial dendritic growth mode, expected for the growth of a metal on a semiconductor with significant lattice mismatch. Massies *et al* [57] attribute the multiple epitaxial orientations obtained to a Volmer-Weber growth mode. However, ten years later, the nucleation phase was studied in more details by Donner *et al* [59] at room temperature and revealed that the growth mode was actually Stranski-Krastanov with the formation of a wetting layer on which $3D$ islands subsequently formed (Figure 2.14). Below 0.2ML the RHEED pattern displayed streaks with the bulk $GaAs$ spacing in the [110] direction but conserved the same pattern in the orthogonal $[\bar{1}10]$ direction. After 0.25ML, the pattern changed to a $(4 \times 1)$ reconstruction which persisted until 0.75ML. Afterward, islands nucleation was observed. The authors also estimated the change in the interplanar spacing in both directions (calculated from RHEED data). In the [110] direction, the initial spacing remained unchanged at 4Åup to 6ML (representing the nucleation of $Al(100)$), after which extra-diffraction spots appeared corresponding to a lattice spacing of 2.86Å(representing the concurrent nucleation of $Al(110)$). In the $[\bar{1}10]$ direction there was an immediate increase in the streaks separation corresponding to a change in the lattice spacing from 4Åto 2.86Åwith the deposition of only 0.30ML. These very different results were attributed to directionally dependent adatom-substrate interactions in the [110] direction and strong adatom-adatom interactions in the $[\bar{1}10]$ direction. This was supplemented by the fact that the Auger Electron Spectroscopy (AES) analysis showed $AlAs$-like covalently bonds up to a thickness of 6Å.

Low temperature epitaxy proved to be more successful in the obtainment of single

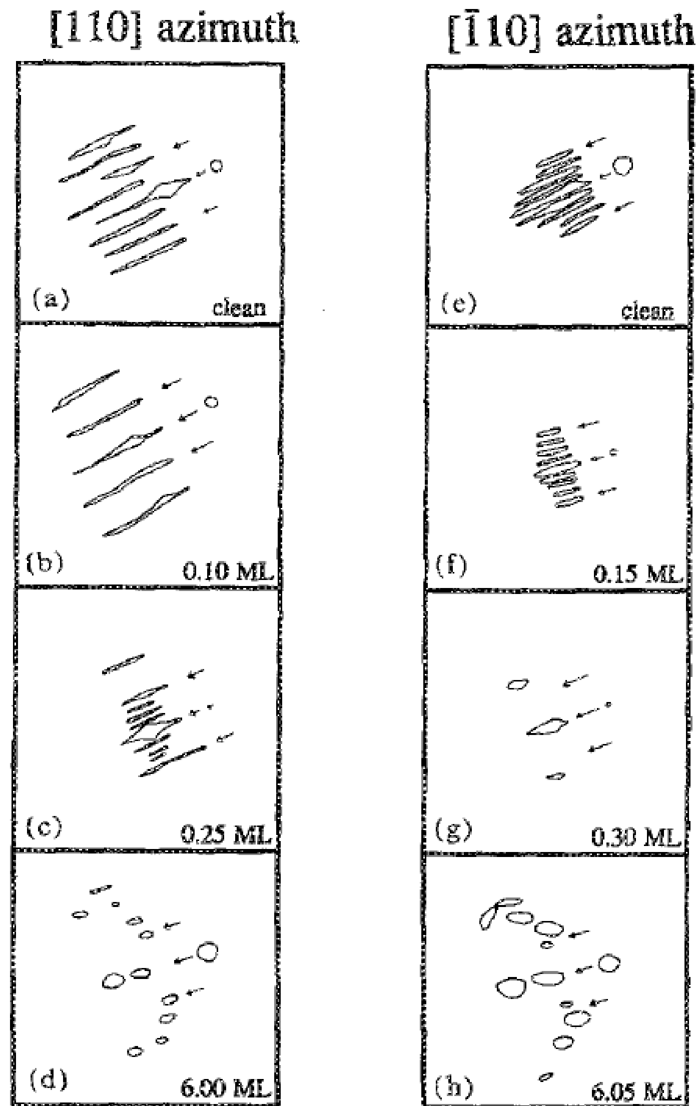


Figure 2.14: Schematic representation of the RHEED patterns observed in the growth of $Al$ on $GaAs(001) - (2 \times 4)$ in the [110] and [$\bar{1}$10] directions at different coverages. Adapted from [59].

crystalline phases. Prinz *et al* [60] had indeed suggested in 1982 that lowering further the growth temperature could hinder the surface mobility of $Al$ and lead to a more uniform coverage by preventing the formation of clusters. Technological progress allowed such low temperature growths to be realized as in the work of Oh *et al* [61] and more recently Shi-Wei *et al* [62]. Both reported successful growths of single crystals at 0°C and highlighted the result dependence on the starting reconstructed surface, namely, a $Ga$-rich surface led to a (110) phase, while an $As$-rich led to a (111) or (100) phase. The grown phases were identified with X-Ray Diffraction (XRD) and compared to conventionally evaporated $Al$ films, the latter showing extra diffraction peaks (indicative of a polycrystalline material). An AFM study estimated the roughness of the (111) sample to 0.4nm, proving its remarkable smoothness.

The last growth parameter investigated was the type of dangling bonds offered by the topmost layer. Landgren, Ludeke and Serrano [53] suggested that strong tetrahedral $Al - As$ bond on an $As$-stable surface would lead to $Al(110)$ formation while weaker metallic $Al - Ga$ bonds would favor $Al(100)$ formation. For the latter, Ludeke, Chang and Esaki [52] have proposed a model which explains that the surface asymmetry due to the reconstruction, combined with the strongly directional tetrahedral bonding of the $As$-stabilized $GaAs$ structures, favor the growth of tetrahedral $AlAs$ (at the interface layer) hence the nucleation of an $Al(110)$ phase since subsequent atoms would nucleate at the face-centered position (lowest energy sites). The dependence of the growth orientation upon the surface reconstruction has been observed experimentally and reported in the literature with results not always consistent with the aforementioned theories. Mixed phases of $Al(100) + Al(110)$ with different degrees of texture have been obtained on the three $As$-rich $(4 \times 4)$, $As$-stable $(2 \times 4)$ and $Ga$-rich $(4 \times 6)$ orientations. Missous *et al* [63] attempted to summarize and classify the different reported outputs but no general pattern could be brought out of the too diverse pool of results. The authors noted that slight changes to the vacuum and temperature conditions could lead to drastically different grown orientations with the same starting reconstruction. Growth on vicinal surfaces was also investigated. In 1981, Petroff *et al* [64] suggested that the presence of steps on the surface would favor the growth of the $Al(110)$ orientation with a better additional matching along the step edge, therefore reducing the amount of $Al(100)$ domains. Such growth was

attempted very recently by Lovygin *et al* [65] on a 3°-misoriented $GaAs(001)$ substrate. A detailed TEM study revealed that the type and orientation of the grains of the layer grown on the vicinal surface was identical to the case of a layer grown on a singular surface. Another observation, although not quantified but worth mentioning, is that the interface underneath the $Al(100)$ grains appeared to be smoother and with less defects than the interface underneath the $Al(110)$ grains.

From this brief review of past work, it is clear that the growth orientation of the $Al$ layers is critically dependent on the growth conditions, even though the exact details of this dependence are still controversial. Low temperature growth seems to be vital for the formation of single crystalline materials. In addition, the extreme sensitivity of the grown orientation to the procedure emphasizes the need for strictly controllable and reproducible parameters (initial substrate reconstruction, temperature, background pressure). It should be mentioned that the cited works monitored cautiously the $As$ background pressure posterior to the buffer layers growth to this end. However, very little or no efforts were made to properly measure and/or control the growth temperature.

### 2.3.3 $Al$ epitaxy on $Si$ substrates

The case for $Si$ as a substrate for epitaxial growth of $Al$ layers is much simpler than the $GaAs$ counterpart and a consensus was reached rapidly on the growth process. Early studies of $Al$ overgrowth on $Si$ reported polycrystalline structures formed by isolated islands coalescing after the deposition 40nm of $Al$ [66]. The first MBE studies of epitaxial growth of $Al$ on $Si(111)$ only took place in 1986 when Legoues *et al* [32] obtained single crystal $Al(111)$ after annealing at 400°C the samples deposited at room temperature. Indeed, while they observed a strongly textured $Al$ material after deposition, the concurrent $Al(100)$ phase disappeared after annealing. The authors noted a structural arrangement matching 4 $Al$ atoms ($\sim 16.1980$Å) to 3 $Si$ atoms ($\sim 16.2927$Å) at the interface, optimizing the energy by the creation of misfit dislocations. This accommodation of $n$ overlayer atoms to $m$ substrate atoms had been predicted a few years before by Zur and McGill [28]. On $Si(001)$wafers however, no epitaxial growth was observed even though the same lattice arrangement could in theory have been possible. Epitaxial growth by Ionized Cluster Beam

(ICB) at room temperature have also been demonstrated by Yamada *et al* [67]. With results consistent with Legoues [32], Yamada detailed further the growth processes. On $Si(111)$ samples, the $Al$ started forming islands from the first stage displaying a spotty RHEED pattern indicative of the presence of several orientations on the surface. After $10nm$, one orientation took over and dominated until the end of the growth. On $Si(001)$, $Al(110)$ bicrystals nucleated and persisted until the end of the growth. These bicrystals were also reported by Hasan *et al* [68] in 1990. An in-depth AES study led the authors to suggest a Stranski-Krastanov growth mode: it seems that the $Al$ had a layer-by-layer growth mode up to 4ML, after which it grew in flat islands because the pseudomorphic[1] $Al$ wetting layers were too distorted to keep a $2D$ growth mode. Ensuing these works, the room temperature growth of $Al(111)$ on $Si(111)$, followed by a 400-450°C annealing became a popular option to obtain single crystalline layers. However two studies showed the limits of such a process. The first one, by Brillson *et al* [30], investigated the interdiffusion of $Al$ and $Si$. While in theory the solubility of $Si$ into $Al$ is limited, recrystallization of $Al$-doped $Si$ at the interface has been observed. Brillson showed that the post-growth annealing of the wafers led to an interface 10 times less abrupt and that the cleanliness of the starting surface was a crucial parameter since intentionally disordered surfaces led to more interdiffusion. This was later confirmed by Fortuin *et al* [69], who showed that annealing increased the $Si$ incorporation into $Al$ from 0.03% to 0.17% in single-crystalline layers and to 0.47% in polycrystalline layers. The second study by Doerner *et al* [70] showed that annealing also induced strain (higher if the film was thin). This can be explained by the difference in thermal expansion coefficients between $Al$ and $Si$. The high temperature growth investigation was subsequently abandoned since it had only led to polycrystalline materials with high strain induced dislocations upon cooling to room temperature.

The research around $Al$ on $Si$ was refocused on $Si(111)$ substrates and low temperature MBE growth which led to successful single crystalline epitaxy as reported by Miura [71], Fortuin [69] and Liu [72]. Miura [71] explored the growth of $Al$ on different reconstructions of the $Si(111)$ surface, namely $(7 \times 7)$ and $(“1 \times 1”)$. Perfect epitaxy was found to happen at 50°C on the $7 \times 7$ reconstruction only, which could be explained by the covalent bonding sites the superstructure offers to $Al$ adatoms. The need for extremely smooth starting

[1] Describes a layer which is strained to match the substrate it is deposited on.

surfaces was also highlighted by the observation that single crystals did not grow on a rough, even though clean, $(7 \times 7)$ surface. The reason for this stems from the privileged nucleation of $Al(100)$ at the step edges while $Al(111)$ growth preferably occurs on terraces, due to lattice matching. This result was confirmed and elaborated on by Fortuin [69] in 1996. Finally, a very low temperature growth ($-128°$C) was realized by Liu et al [72] in 2004 and led to the discovery of a new growth mode. The authors noted the nucleation of a disordered wetting layer followed by the formation of small flat islands. The formation of such islands was attributed to the hindered thermal energy (low temperature kinetics), preventing the $Al$ atoms from overcoming the Schwoebel barrier, and thus subsequent $3D$ growth should have been expected. However, at a critical thickness of 4ML, sharp RHEED streaks appeared revealing a layer-by-layer growth and an already relaxed $Al$ lattice. A well-defined stepped surface was observed by Scanning Tunneling Microscopy (STM) at 8ML coverage with a root mean square RMS roughness of 0.05nm. These results agree with a model suggested a few years earlier by Zhang [73] called the electronic growth mode. No changes to the crystal structure were observed when warmed up to room temperature.

The dependence of the grown orientation on the presence of surface steps has also been established. It was first suggested by Legoues *et al* [32] that because of the $4Al : 3Si$ arrangement of the atoms at the interface, the presence of a step which height could not fulfill this exact arrangement would result in different stacking sequences on each side of the step. This phenomenon was later observed by Sosnowski *et al* [74]. Surprisingly, instead of the expected polycrystalline material, it led to the growth of single crystalline $Al(100)$ layers at room temperature on a $Si(111)$ substrate with a cut-off angle of $3.5°$, while non-misoriented $Si(111)$ wafers led to $Al(111)$ layers. The reason was found to be the different accommodation possibilities of the vertical mismatch by a low tilt of the crystallites (described in details in [74]) and therefore dependent on the step height. The authors also highlighted the importance of using regularly distributed steps. Indeed, growth on a similar cut-off wafer prepared with less-uniformly distributed steps led to a higher content of $Al(111)$, even after annealing.

This review provides us with solid research directions as to obtaining single crystalline atomically smooth $Al$ layers on $Si$: epi-ready $Si(111)$ wafers and low temperature growth should be favored. The use of vicinal surfaces is not recommended unless the uniform

distribution of the steps on the surface can be controlled with precision.

# Chapter 3

# Equipment and techniques

## 3.1 Molecular Beam Epitaxy

In this section, basic information about MBE principles will be provided. It includes the description of the Ultra-High Vacuum (UHV) environment, of the system itself and of the sources used. Many books exist in literature that will satisfy the reader's curiosity for further detail on technical information [75] [76] [77] [78].

### 3.1.1 The need for Ultra-High Vacuum (UHV)

The majority of deposition techniques for thin films require an environment classified as high vacuum (HV) and covering pressures from $10^{-3}$Torr to $10^{-9}$Torr[1]. MBE is an even more demanding technique:typically, the so-called base pressure in the growth reactor (i.e. pressure prior to starting the deposition process) is in the $10^{-10}$ to $10^{-11}$Torr range. The reason for this extremely low pressure lies in the very high quality standards of MBE grown films. Some believe that the $10^{-9}$Torr limit is set by a mean free path[2] that needs to be larger than the distance between the sources of the atomic beams and the substrate. This

[1]Unit of measurement for pressure commonly used in UHV systems. 1Torr= $1.333 \times 10^2$Pa

[2]Distance traveled by a moving particle without undergoing a collision with another particle.

is a necessary condition but not sufficient. Indeed in most of the existing systems this distance is less than 20cm and such a mean free path is achievable for pressures lower than $10^{-3}$Torr, which would require HV and not necessarily UHV. In fact, the key reason for a UHV MBE environment concerns the contamination by background molecules. To ensure high purity of the film, the time to deposit 1ML of contaminants should be at least $10^5$ times smaller than the time required to deposit 1ML of materials on the substrate:

$$t_{monolayer}(beam) < \frac{t_{monolayer}(contaminants)}{10^5} \quad (3.1)$$

The duration of the deposition of 1ML can be related to the partial pressure through the definition of the flux (number of molecules impinging a surface per unit area and time) and this formula:

$$w_i = p_i \sqrt{\frac{N_A}{2\pi k_B M_i T}} \quad (3.2)$$

where $w_i$ is the flux of the species $i$, $p_i$ is the partial pressure of the species $i$, $M_i$ is the molar mass of the species $i$, $T$ is the temperature and $N_A$ and $k_B$ are the Avogadro and Boltzmann constants, respectively. Using typical growth rates for MBE $GaAs$, this leads to a maximum pressure of the residual gases in the vacuum reactor of about $10^{-11}$Torr. This can be achieved only through deploying highly efficient UHV pumps (cryo-pumps, ion pumps, and/or UHV turbo pumps), using liquid nitrogen ($LN_2$) cryo-shrouds in the reactor, upholding extreme cleanness of the growth environment through very stringent operating procedures and using ultra-pure elements for the molecular beam sources. Moreover, after every opening of the growth reactor to atmosphere, the system should be baked (several days to several weeks) to outgass from the inner surfaces the moisture and other volatile contaminates which may have entered the reactor.

### 3.1.2 Description of the GEN10 system

The MBE reactor used in this project, the GEN10 system from Veeco, is composed of four modules. Each module is equipped with its own pumping system and is separated from the others by UHV gate valves. The four modules, presented on Figure 3.1, are:

1. Load-lock (LL)
2. Cluster Tool (CT)
3. Preparation Module (PM)
4. Growth Module (GM)

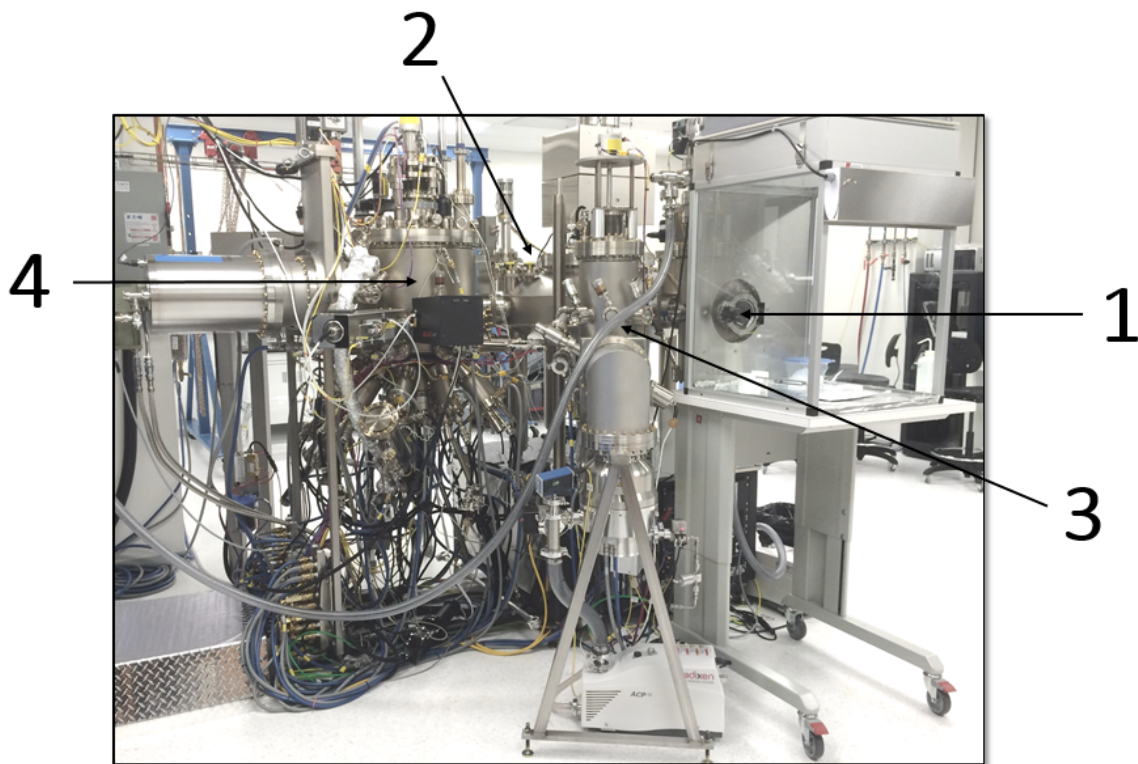


Figure 3.1: Veeco GEN10 MBE system of the University of Waterloo MBE Laboratory. Zone 1 is the LL, zone 2 the CT, zone 3 the PM and zone 4 the GM.

The LL is the module where wafers are loaded into. Afterwards, the moisture can be pumped out in the process of heating the interior of the module to 200°C. After the the pressure reaches the low $10^{-8}$Torr level, the wafers are transferred to the CT, using the robot which is housed in there. The pressure in the CT is kept in the $10^{-11}$Torr range.

CT has a total of 16 wafer storage positions. Depending on the process, the substrates can be transferred to the PM where they can be outgassed to much higher temperature (up to 800°C) with or without additional radio-frequency plasma cleaning using $Ar$ or $H$ atoms. From PM or directly from CT the wafers are finally transferred to the GM where the deposition of desired epitaxial structures takes place.

### Details of the growth module

The essential elements of the growth module consist of a substrate manipulator and source cells, as shown in Figure 3.2. Prior to loading the wafer for deposition process, the substrate heater and the source cells to be used are heated above the growth temperature to degas any possibly remaining contaminant adsorbed on their surface. At the end of this period (generally two hours), the substrate manipulator is cooled down and the temperatures of the effusion cells is lowered to the value used during the deposition. Molecular fluxes are checked before loading the substrate into the GM and cells temperatures are corrected if needed to achieve desired growth rates. The molecular flux from a cell is directly controlled by the cell temperature. The calibration of the flux versus the cell temperature is an ongoing process: for a given cell temperature the flux depends on the amount of material in the cell. Once these settings have been made, the substrate is put in the manipulator in the center of the GM. The substrate holder is typically radiatively heated and rotated during the deposition in order to achieve a good uniformity of the film thickness and composition across the entire wafer. The substrate temperature is one of the key parameters for the growth. The growth then proceeds by opening and closing the shutters associated to the cells containing the material to be deposited, depending on the desired composition. Some cells are also equipped with regulating valves, further controlling the molecular flux. The arrangement of the cells around the system and the angular direction of their beam are designed to yield flux uniformity on rotating substrates better than 1.5% over 3" wafer [79]. The entire process, including the operation of the cell shutters, is controlled by a dedicated computer, permitting switching of the molecular fluxes ON and OFF with an actuation time better than 100ms. The growth area is surrounded by cryopanels which are typically cooled down by circulating liquid nitrogen (77K). This low temperature turns the cryopanel walls into traps for contaminants, further improving the vacuum quality.

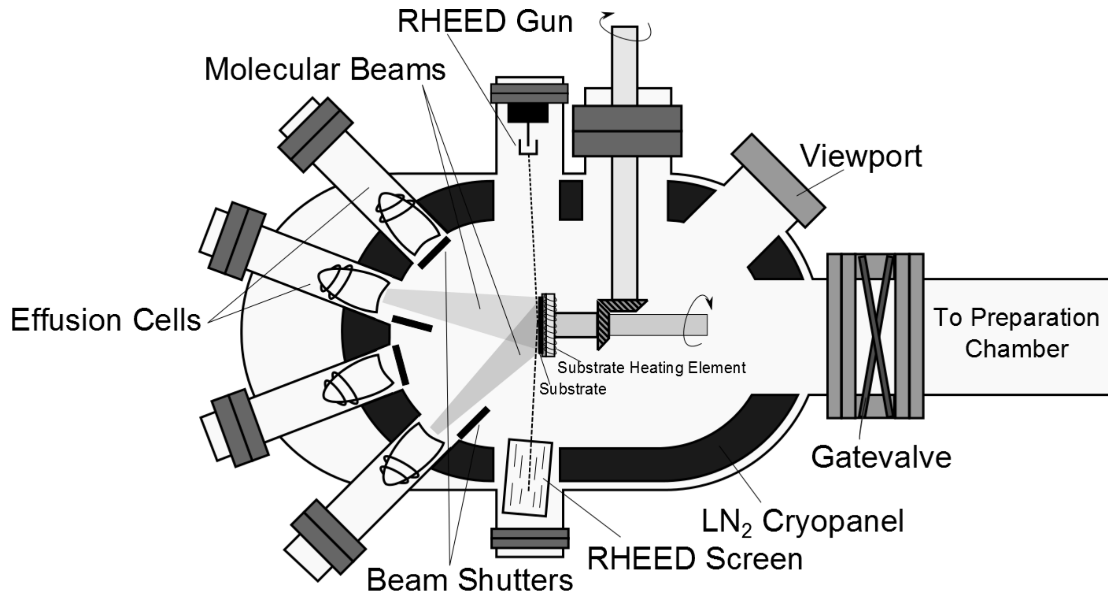


Figure 3.2: Schema of the growth module of a MBE system. Source: [80].

### Sources

The principal sources used in MBE are thermal effusion cells, directly mounted in the growth chamber in dedicated ports. Each cell is heated to a temperature needed to achieve desired evaporation rate of the element it contains. Group V elements evaporate as molecules rather than atoms, and depending on the process may benefit from cracking larger molecules into smaller. This is achieved with cells equipped with cracking zone. In the case of $As$, the $As_4$ molecules are typically cracked into two $As_2$ molecules. Indeed it has been shown, for example, that the use of $As_4$ over $As_2$ benefits optical properties of $GaAs/AlGaAs$ (Aluminum Gallium Arsenide) quantum wells. For this project dimeric Arsenic $As_2$ was used by passing $As_4$ molecules through the cracking zone kept at 900°C.

The $Al$ cell used for deposition in this project is is a dual-filament cell, which top filament was disabled to keep the cell tip cooler. This aims at preventing the $Al$ from flowing out of the crucible. $Al$ is contained in a 60cm$^3$ pyrolitic boron nitride ($PBN$) conical crucibles. Special precautions needs to be taken to avoid so-called flux transients which are due to temperature gradient changes in the cell upon opening of the shutter.

Indeed, the opening causes a change in the top melt surface environment that sees the cold walls from this point forward. Moreover, the shutter reflects heat back into the cell and its removal suppresses this source of heat. The thermocouple is in contact with the bottom of the crucible. Receiving no immediate feedback on the changes at the top melt surface upon shutter opening or closing, the loop control system with feedback from the thermocouple is not able to compensate the temperature change of the melt surface. The aforementioned effects can take a few minutes to stabilize the temperature of the melt surface. The beam flux immediately after shutter opening is therefore higher than the equilibrium value to which it settles on after longer period of time, sometimes by as much as 50% depending on the construction of the cell, shutter and material being evaporated [81]. In the reported experiments, to compensate the flux transient, the cell temperature set point was increased in our experiments by 0.5°C upon opening of the shutter and lowered back to its original value upon closing of the shutter. This simple procedure modified the flux transients and resulted in about 2% dip only in the flux value over about 2 min after shutter opening, and subsequent recovery to its initial value over the next 2min.

## 3.2 Characterization techniques

### 3.2.1 *In-situ* metrology

One of the main strengths of MBE is the possibility to mount several metrology tools on the system. These tools can provide information in real-time during the growth process. Not only is it useful to understand growth dynamics but it is also a way to control the fabrication of the nanostructures. Indeed, by monitoring the surface reconstruction and morphology, one is able to optimize growth conditions in order to obtain the best quality film. Different facilities have different set of characterization tools according to their needs. Here are reviewed only those used in this project.

**Reflection High Energy Electron Diffraction (RHEED)**

RHEED allows to monitor the growth process with accuracy: it can provide information on the growth rate, surface reconstruction as well surface roughness. RHEED uses an electron gun to send high-energy electrons at a grazing incidence to the substrate. For the system used in this project, the electron acceleration voltage can be set in the range $0.5 - 15$kV, its intensity $0.01 - 100\mu$A, allowing a focus spot on the substrate smaller than $100\mu$m. In the experiments described here, the voltage was maintained at 10kV and the intensity at $0.2\mu$A. Thanks to their quantum nature and wave character, the electrons are diffracted off the surface atoms and form characteristic diffraction patterns on the phosphorescent screen on the other side of the chamber. For rough surfaces, thanks to the very small angle of incidence (from about $0.5°$ to $5°$), the electrons penetrate volumetric surface features which produce diffraction typical of TEM, i.e. individual diffraction spots characteristic of the $3D$ crystalline structure of the layer (as seen in the top panel of Figure 3.3).

In the case of smooth crystalline surfaces, the surface reconstruction can be inferred from the analysis of the diffraction patterns. The spacing between the streaks on the fluorescent screen is inversely proportional to the size of the unit cell of the reconstructed surface in the direction perpendicular to the beam incidence direction (see Appendix C). Hence, for a known surface configuration ($GaAs(001) - (2 \times 4)$ for example), the proportionality constant can be computed without knowing exact distance from the sample to the RHEED screen, or RHEED gun acceleration voltage, and subsequently used to calculate the associated atomic planes spacing from the measured distance between the streaks on the screen for other materials, such as Aluminum.

Furthermore, it has been discovered by J.J. Harris [82] that the intensity of individual spots forms damped oscillations resulting from periodic smoothing and roughening of the surface as individual atomic layers are being deposited. These oscillations give direct measure of the growth rate since their period corresponds to the growth of 1ML (Figure 3.4). The exact characteristics of these oscillations are still a hot debate but RHEED studies in MBE have underpinned much of a progress in surface science over the past four decades. RHEED oscillations are often used to calibrate the growth rates. In close feedback they can be used to control the layer thickness to a fraction of atomic layer.

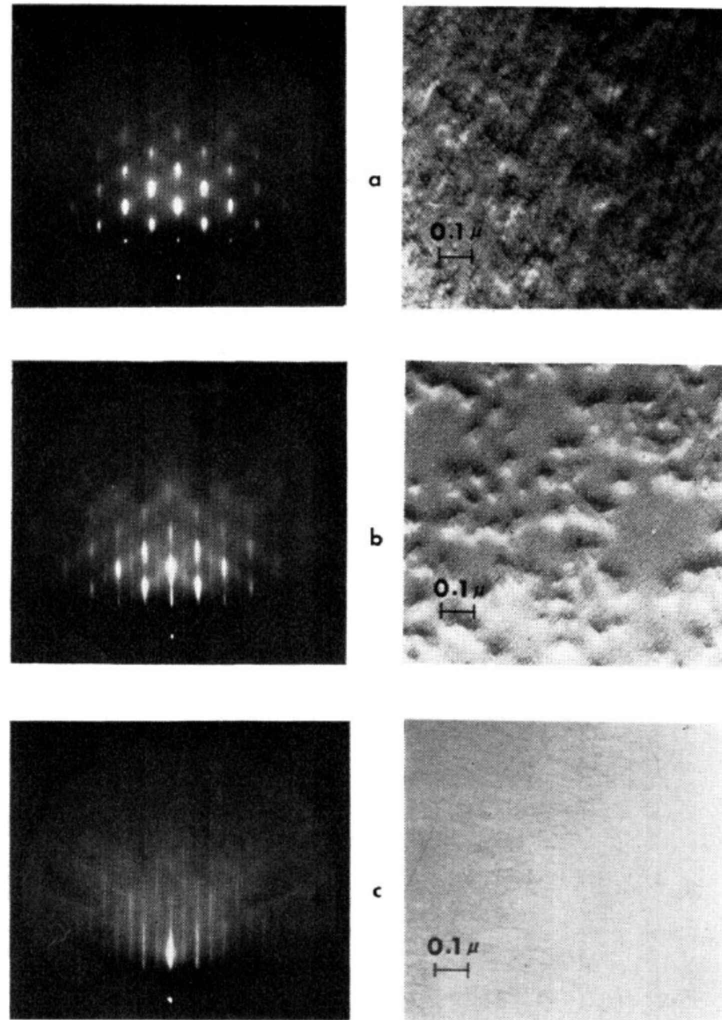


Figure 3.3: Correlation between the RHEED pattern and the surface morphology as studied by Cho *et al* in [11]. RHEED patterns and the corresponding micrographs of Pt-C replica of the same surface. (a) $Br_2$-methanol polish-etched $GaAs(001)$ substrate heated in vacuum to 885K for 5min. (b) Deposition of an average thickness of 150Åof $GaAs$. (c) Deposition of 1$\mu$m of $GaAs$.

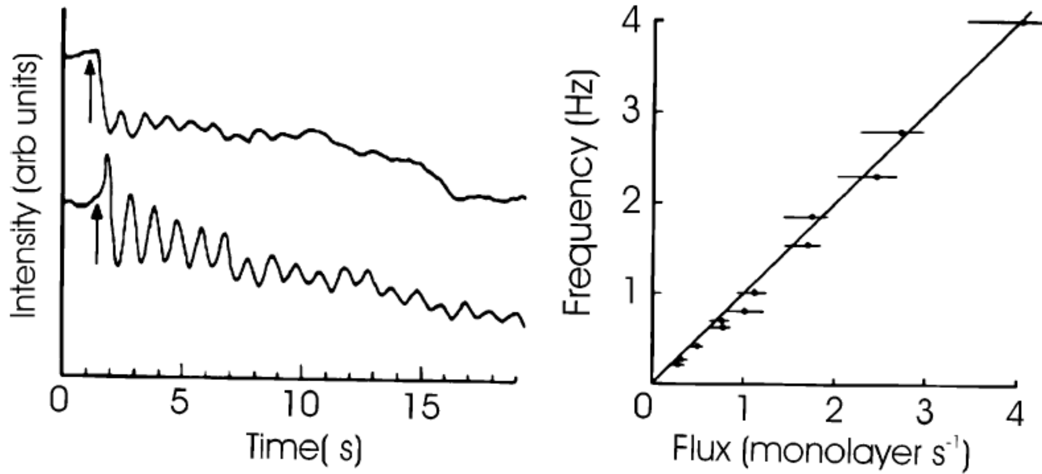


Figure 3.4: RHEED intensity oscillations observed on $Sn$-doped $GaAs$, demonstrating that the oscillation frequency is directly related to the growth rate. Source: [82].

### Band-Edge Thermometry (BET)

All MBE systems are equipped with thermocouples to track the temperature of the wafers. However, the thermocouples in the manipulators are not in contact with the substrate and can show a temperature up to 150°C higher than the actual wafer temperature. This temperature difference depends on the substrate, on the temperature range and ramp rate so the wafer temperature cannot be calibrated against the manipulator temperature uniquely with the thermocouple. Band-Edge Thermometry (BET) also known as Absorption Band-Edge Spectroscopy (ABES), provides much more reliable measurement by taking advantage of the electronic properties of semiconductors. Indeed, the semiconductor bandgap, and therefore its fundamental absorption edge, is temperature dependent hence measuring its position determines the substrate's temperature. A set-up relying on the double-pass of the light through the substrate is displayed in Figure 3.5. Light from a halogen lamp is scattered back towards the spectrometer's input from the rough back surface of the substrate.

The dependence of the bandgap energy ($E_g$) on the temperature ($T$) is described by

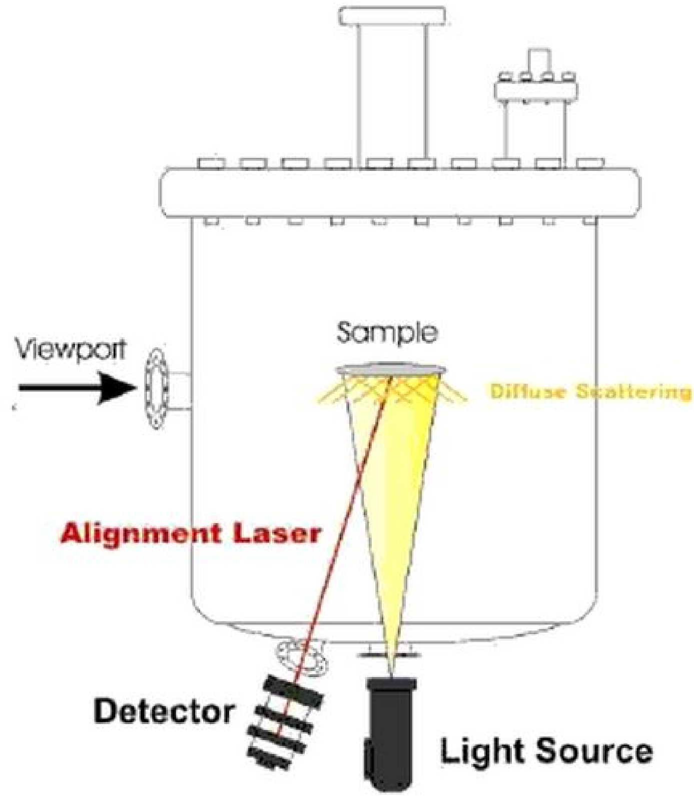


Figure 3.5: Schematics of BandiT BET k-Space Associates Inc.) mounting on Veeco GEN200 MBE

Varshni empirical expression:

$$E_g(T) = E_g(0) - \alpha \times \frac{T^2}{T+\beta} \tag{3.3}$$

where $\alpha$ and $\beta$ are numerical coefficients. Such way of substrate measurement, unlike for instance pyrometry, does not rely on the black body emission of light from a hot substrate and can be used for non-contact temperature measurements well below 0°C. For the experiments discussed in this thesis a commercial system from k-Space Associates Inc, BandiT was used to monitor substrate temperature below 100°C. As was highlighted previously, the substrate temperature is of paramount importance for the epitaxy of *Al*

which is a highly reactive and diffusive material. The exact knowledge of this temperature is crucial to the reproducibility of the growth process. Lack of proper instrumentation to measure the lower ranges of substrate temperatures in MBE can explain the inconsistency of results one can encounter in the literature as to the orientation of the grown $Al$ epitaxial layer orientations, while accurate temperature monitoring with BET instrument in the experiments reported here gave consistently reproducible results.

#### Residual Gas Analyzer (RGA)

The Residual Gas Analyzer (RGA) used in this project is a quadrupole mass spectrometer. RGA are used to monitor the quality of the vacuum in the growth chamber and quantify each gas species contribution to the background pressure. The instrument is mounted directly on the vacuum chamber, allowing the molecules inside the system to move close to the filament wire and the anode wire cage. The residual gas is then ionized when it collides with the thermoelectrons discharged from the filament. The created ions are accelerated through the ion source and reach the mass spectrometer where the ions are separated by mass by the four poles to which direct and alternating current voltages are applied, based on the mass-to-charge dependency of the ion trajectories on the electrical field. Used in the GEN10 MBE system, Stanford Research Inc. RGA can trace residual gases down to $10^{-14}$Torr. RGA are indispensable in ensuring vacuum tightness of UHV systems. For this purpose, Helium ($He$) gas is sprayed on the external surfaces of the system and flanges, while the RGA is sensing the presence of $He$ atoms in the system. RGA can also be used to study surface chemistry by monitoring the species reflected or desorbed from the growing epitaxial layers.

### 3.2.2 *Ex-situ* metrology

In addition to the techniques available *in-situ*, the samples were further characterized with *ex-situ* equipment. High Resolution X-Ray Diffraction (HRXRD) gave insight into the structural properties of the materials and an AFM was used to probe the surface and observe its morphology at nano-scale. Differential Interference Contrast (DIC) (or

Nomarski) microscopy, was also used to assess epitaxial layer morphology over larger areas.

### High Resolution X-Ray Diffraction (HRXRD)

XRD is the technique of choice to study the structural properties of crystals. It has been broadly described in the literature and many excellent books could provide the interested reader with more details [83] [84]. An XRD system is comprised of an X-ray source, a beam conditioner to control the beam wavelength and divergence, a goniometer to manipulate the sample, a detector to measure the intensity of the scattered X-ray beam and a collimator to limit the divergence of the measured beam. When impinging the sample's surface, the incident rays are diffracted by the different crystal planes (rows of atoms), as represented in Figure 3.6. The scattered rays can interfere with each other. The condition for constructive interferences for a beam scattered by parallel lattice planes is known as Bragg's law and can be written as:

$$2d \sin\theta = n\lambda \tag{3.4}$$

with $n$ an integer, $d$ the interplanar spacing between adjacent parallel planes, $\theta$ the incidence angle on the substrate and $\lambda$ the ray wavelength. This means that the optical path difference between the rays must be a multiple (integer) of the wavelength. Thus, the diffraction pattern of a single crystal should display a line at the so-called Bragg reflection angles, satisfying Equation 3.4. In particular for planes in cubic crystals, Bragg's law can be written as:

$$2a \sin\theta = \lambda\sqrt{h^2 + k^2 + l^2} \tag{3.5}$$

where $a$ is the lattice parameter and $h$, $k$ and $l$ are the Miller indices of the considered set of planes, as defined in Appendix B.

Fulfilling Bragg's law ensures that the point representing the considered planes in reciprocal space lie on the surface of the Ewald's sphere, as described in Appendix C. A rotation of the crystal induces the rotation of the reciprocal space and causes different planes to lie on the sphere as shown on Figure 3.7.

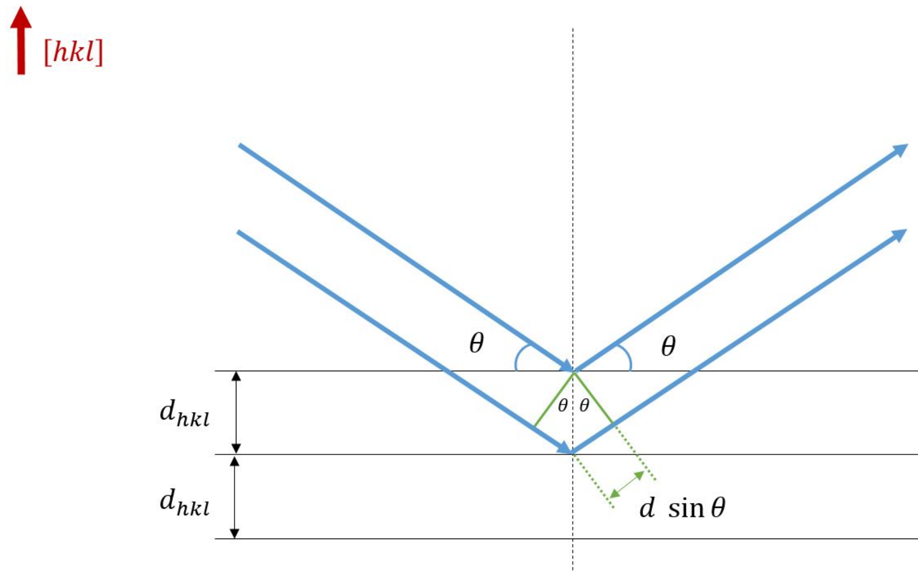


Figure 3.6: Interaction between rays diffracted on parallel planes of a crystal showing the optical path difference.

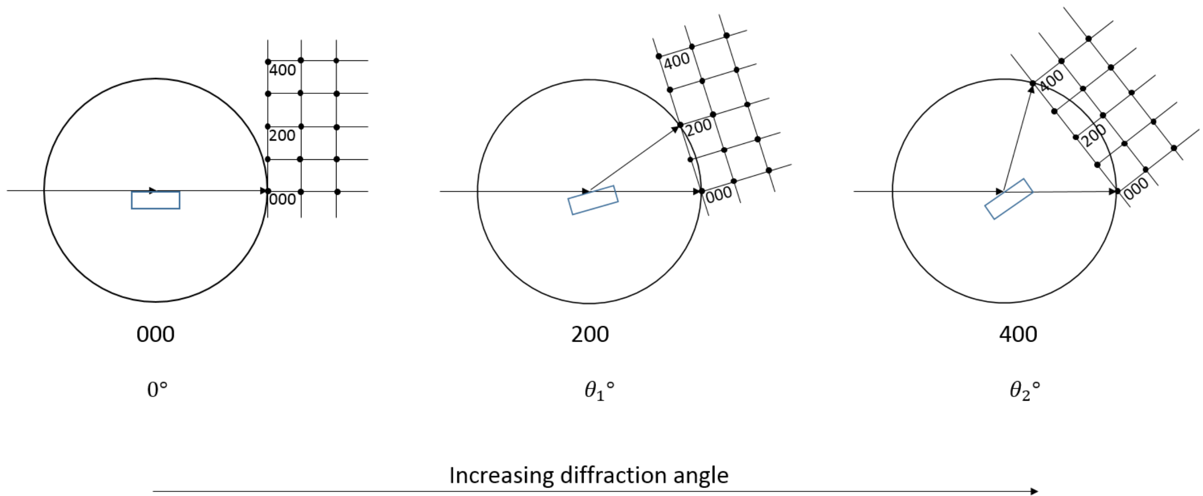


Figure 3.7: Representation of the diffraction of a crystal and the Ewald sphere in different rotations.

Figure 3.8 presents the rotation axis of a typical XRD system. In particular, the incident angle $\omega$ is defined between the X-ray source and the sample surface. The angle $2\theta$ is the angle between the incident beam and the detector axis. $\phi$ is the rotation angle around the substrate's normal. Different scan modes are possible. The ones used in this project are:

- Coupled scan: plot of scattered beam intensity versus $2\theta$ while varying $\omega$ so that $\omega = \frac{2\theta}{2}$ at anytime.
- Rocking curve: plot of scattered intensity versus $\omega$, keeping $2\theta$ constant.
- $\phi$ scan: plot of scattered intensity versus $\phi$

A coupled scan shows intensity peaks whenever $\omega$ fulfills Bragg's law. Each peak can be ascribed to a specific phase by computing the interplanar spacing from the peak position using Bragg's law. The potential shift of a peak from its expected position reflects the layers' strain or tilt with respect to the substrate surface. So-called symmetric scans only reveal planes parallel to the substrate surface. Asymmetric scans, where the sample is tilted compared to the substrate's normal ($\omega = \theta + \chi$), can be used to measure different crystallographic directions.

In a rocking curve, the detector is parked at a determined Bragg angle and the sample is tilted so as to vary $\omega$. If the material is a perfect single crystal (perfect parallelism of the planes), only one set of parallel planes will generate a Bragg reflection and a very sharp peak will be observed. However, if the substrate is made of multiple crystallites slightly tilted with respect to each other, a broader peak will be observed. Such disruptions in the perfect parallelism of the atomic planes can result from dislocations, mosaicity and curvature (previously illustrated on Figure 2.11).

A $\phi$ scan performs a 360° in-plane rotation around the center of the sample. It can be used to confirm crystalline symmetry when locking the 2Theta to the layer Bragg angle with asymmetric scans. Indeed, Bragg reflections from planes that are not parallel to the surface can only be observed at particular azimuths.

Jordan Valley Semiconductors Ltd QC3 and Bruker Corporation D8 ADVANCE systems were used to assess the samples in the following.

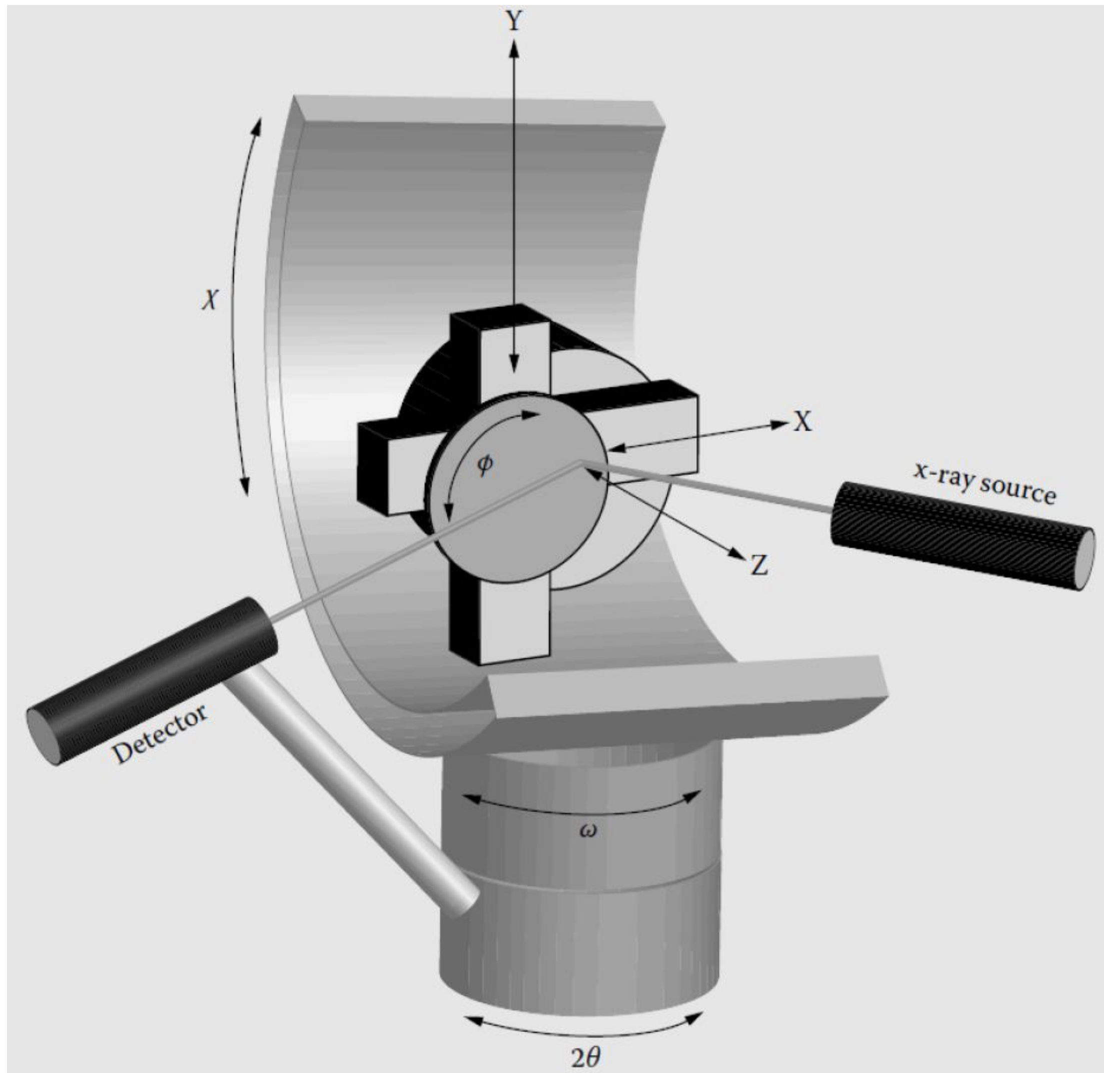


Figure 3.8: XRD apparatus showing the different scan (rotation) axis. Adapted from [83].

**Differential Interference Contrast (DIC) microscopy**

A DIC microscope or, as it will be referred to in the remainder of this thesis, Nomarski microscope, is an optical microscope producing images with a distinctive shadow-cast appearance (as if illuminated with an oblique light). Thanks to the Nomarski prism, made of birefringent material, the illuminating light is split into two beams of orthogonal polariza-

tions. These beams leave the prism displaced laterally by a fraction of the wavelength of the light. The passage of light through the optically dense sample shortens the wavelength hence changes the phase of the light wave. After interacting with the specimen, the beams are recombined and made to interfere with each other. The optical path difference leads to constructive and destructive interference, which is responsible for the observed contrast, revealing the shapes of the observed objects. For reflected Nomarski microscopy, the relief revealed in the image does correspond to the actual topography of the surface features of the investigated sample. The very high sensitivity to the vertical surface displacements (of an order of 1nm) is what makes Nomarski microscopes indispensable tools for epitaxial wafers inspection. The lateral resolution of these microscopes is diffraction limited to about 200nm. The microscope used in this project is a Nikon Corporation Optiphot 66 equipped with a SPOT digital camera (SPOT Imaging Solutions, Diagnostic Instruments, Inc).

**Atomic Force Microscopy (AFM)**

AFM is a powerful tool to probe a sample surface. With a vertical resolution down to a tenth of nanometer and a lateral resolution down to about 30nm, it gives extremely accurate measurements of a wafer morphology. Equipped with a cantilever, the system uses a sharp tip to scan the wafer surface ($x, y$ directions) as shown on Figure 3.9. As the tip approaches the surface, it experiences an attraction force and the cantilever deflects towards the surface. In an even closer range, such that the tip is brought in contact with the surface, an increasingly repulsive force takes over and deflects the cantilever away from the surface. The cantilever deflection is assessed by use of a laser beam directed at the flat top of the tip. Any deflection towards or away from the surface changes the reflected beam direction, which is captured by a position-sensitive photodiode. Changes in the surface topography will induce changes in the tip-surface distance and hence on the cantilever deflection. By using a feedback loop, the system measures the signal variations required to maintain a constant height of the tip above the surface (i.e. to keep the reflected beam at the same position). The processed data results in an image of the surface mainly corresponding to the surface topography but also potentially impacted by the atoms bonding. The system used in this project is di-Innova (Veeco Instruments Inc.). Analysis

softwares, such as Nanoscope Analysis (Bruker Instruments) used in the following, are able to give an estimate of the surface average roughness and line sections of the morphology. While these data must be interpreted with care, they can reveal interesting patterns not visible with conventional microscopes.

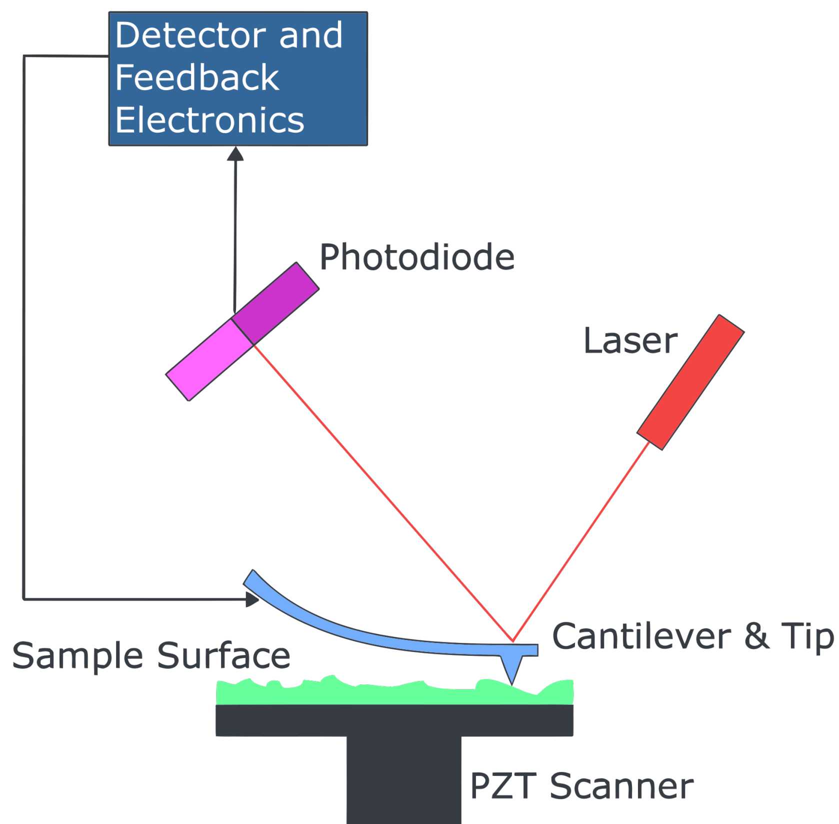


Figure 3.9: Schematics of AFM Source: [85].

## 3.3 Experimental procedure

### 3.3.1 Preparation of the substrates

The wafers used in this project were epi-ready[1]. As such, no additional *ex-situ* cleaning was employed prior to loading into the system (shown on Figure 3.10). All tools to manipulate the wafer, however, were cleaned with $IPA$. Upon opening of the wafer's container, the 3" substrates were picked up with a vacuum wand[2] (WaferPik ®Wand, TDI Inc.) and placed onto Molybdenum UNI-Blocks substrate holders (Veeco Instruments Inc.). Some growths were made on quarters rather than on full wafers. In this case, the wafer was cleaved using a diamond scribe: a small mark was made with the diamond scribe at the location where the wafer had to be cleaved, the extremity of a tantalum wire was inserted under the wafer and slight pressure was applied on each side of the mark with clean tweezers. The cleaving generated some dust, subsequently blown with dry Nitrogen. The quarters were then placed onto the substrate holders using a spring and retainer plates set designed to accommodate quarters of 3" wafers. Each wafer holder was used for a specific type of substrate only ($Si$ or $GaAs$) to minimize cross-contamination. The cleaving and assembly of wafers onto the Molybdenum holders took place in a portable laminar flow hood (Vertical Clean Ceil Workstation, Microzone Corporation) juxtaposed to the LL door. The wafer-holder assembly was then put into the system LL, whose door was only open for a few seconds at a time. The LL was immediately pumped down and outgassed to 200°C for 2h, at the end of which period the pressure reached $\approx 1.8 \times 10^{-8}$Torr. After this step, the wafers were subjected to the following procedures (or combination of them) depending on the studied growth conditions.

### 3.3.2 Thermal cleaning

The wafers were annealed in the GM to desorb the native oxide. The $GaAs$ wafers were annealed to 630°C for 5 minutes under $As$ flux to prevent surface decomposition. After this

[1] Can be used without further treatment.

[2] Tool for manipulating a wafer with the use of a suction pump.

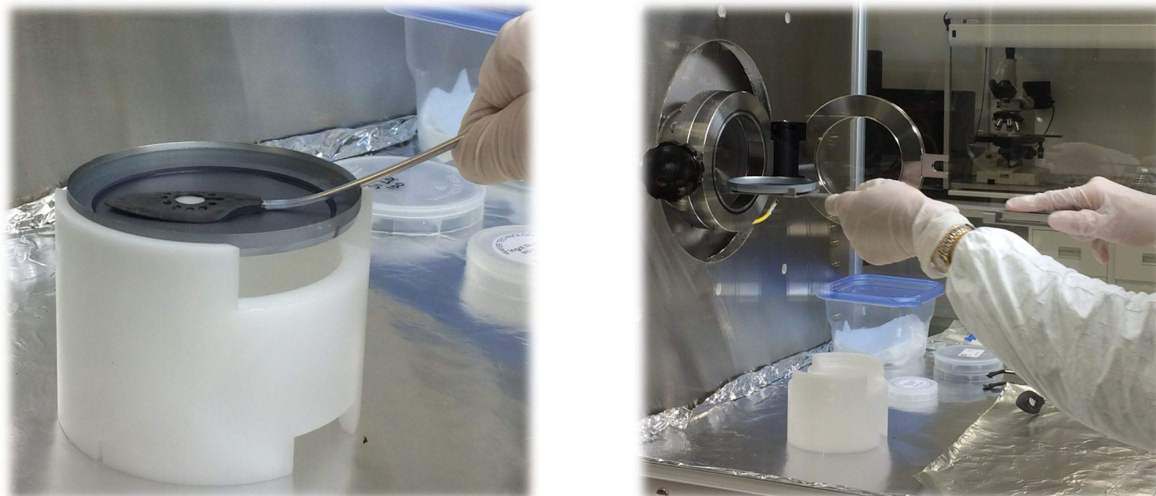

Figure 3.10: Loading of the substrates as described above: (left) the epi-ready wafer is placed with the vacuum wand onto a Molybdenum holder; (right) the wafer-holder assembly is loaded into the LL.

time, it was verified with the RHEED that desorption of the oxide had indeed been achieved (RHEED displaying a streaky pattern). The $Si$ substrates required higher temperature which could not be monitored accurately with the tools available in the system. Instead, the improvement in the sharpness of the RHEED pattern and the increase in the residual gas partial pressure of $C$ on the RGA served as indicators of the oxide desorption. $Si$ substrates were heated according to the following protocol:

1. Heat to 800°C at 60°C/min and wait for the thermocouple reading to stabilize (2min)
2. Heat to 900°C at 20°C/min and wait for the thermocouple reading to stabilize (2min)
3. Heat to 950°C at 10°C/min and wait for the thermocouple reading to stabilize (2min)
4. Heat to 960°C at 10°C/min and wait for the pressure levels to decrease on the RGA (5min)

5. Heat to 1010°C at 10°C/min and be prepared to pause if the RHEED pattern or RGA levels change significantly

The RGA level of $SiO$ (44amu, not distinguishable here from the level of $CO_2$) did not show any significant change over the whole process. On the other hand, both the $CO$ and $C$ (in the cracking pattern of $CO$) profile increased significantly at 960°C and dropped after a few minutes 3.11). As was discussed previously, it has been observed that $C$ desorbs with the oxide [41]. The RHEED pattern at this temperature displayed sharp streaks in contrast with the dim and blurry initial pattern. While the RHEED lines gained further sharpness during the heating to 1010°C, trials to heat it beyond did not improve them further. On the other hand, the Nitrogen partial pressure started increasing slightly from 990°C, which could stem from decomposition of the $PBN$ plate in which the substrate heater wire is placed or from some release of Nitrogen from the $LN_2$ shroud elements facing the wafer. Heating was therefore not pursued beyond 1010°C.

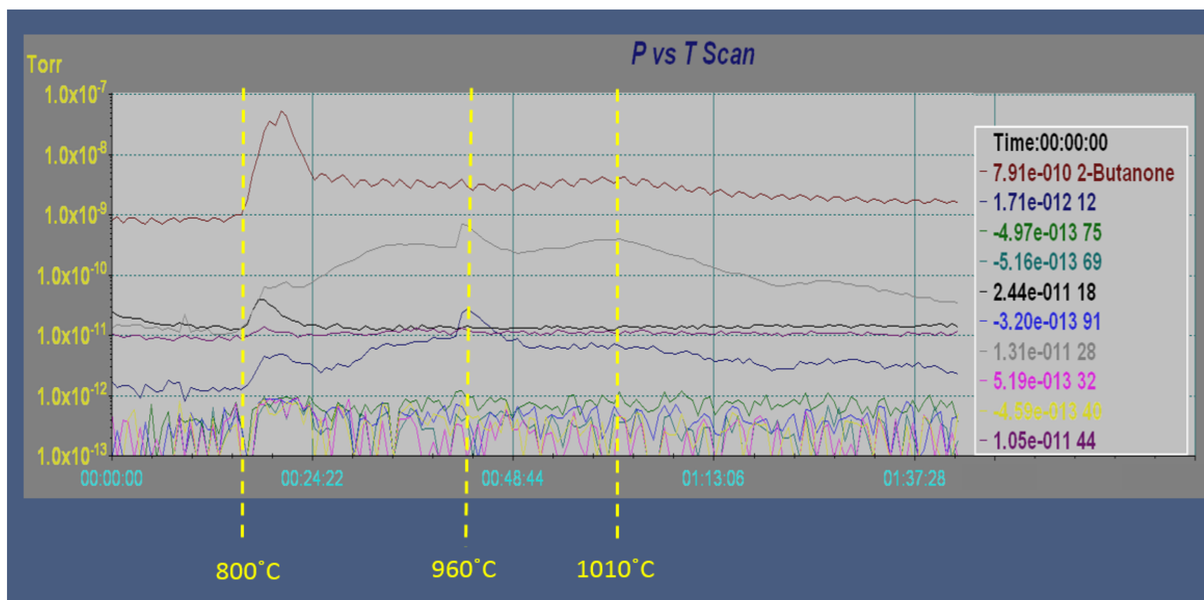


Figure 3.11: Oxide desorption from a $Si$ substrate monitored on the RGA. The indicated temperatures are the thermocouple readings, not the substrate real temperature. The different colors correspond to different atomic masses specified on the legend on the right.

### 3.3.3 Buffer layer deposition (case of the $GaAs$ wafers)

After the oxide desorption from $GaAs$ substrates, a 2000Å$GaAs$ buffer layer was grown at 580°C, followed by a short period $AlAs/GaAs$ superlattice (20 repeats of 20Å/20Å) and a 200Å$GaAs$ capping layer. Since most of the residual substrate contamination stays at the interface with the epitaxial layer, the surface prepared in such a way was practically contamination-free and atomically smooth, providing superior substrate for $Al$ epitaxy. A 2000Åbuffer was grown while ramping the substrate temperature from 580°C to 620°C and reducing the $As$ flux. Growth rates of 2Å/s and 1Å/s were used for $GaAs$ and $AlAs$ respectively. Some wafers were prepared with a simpler structure with no superlattice (only 2000Åof $GaAs$ grown at 2Å/s). A final 200Å$GaAs$ cap was deposited (at 2Å/s) on top of the structure.

### 3.3.4 Cooling down

The cooling conditions of the substrate after its preparation determined the surface reconstruction. In the case of $GaAs$, by quickly lowering the $As$ flux [1] while reducing the temperature to about 350°C immediately after the buffer deposition, an As-stabilized $(2 \times 4)$ reconstruction was preserved (Figure 3.12a). On the contrary, when a large $As$ overpressure was maintained during a few minutes after the buffer deposition [2] while the substrate temperature was lowered to about 350°C, an $As$-rich $(4 \times 4)$ reconstruction was yielded (Figure 3.12b). In the case of $Si(111)$, the "$(1 \times 1)$" unreconstructed surface is the dominant phase at elevated temperature (above 900°C). The switch to the $(7 \times 7)$ phase occurs at 837°C according to [21], provided that the substrate is cooled slowly enough. The cooling rate used through this switch was of 5°C/min and led to the formation of the $(7 \times 7)$ phase as seen on Figure 3.13b. The RHEED images were obtained on rotating substrates by triggering the RHEED camera at preset azimuths. Since the exposure time was of an order of 100ms, and the wafer rotation rate was 1 revolution every 3 seconds, the arcs of spots typically seen for the $(7 \times 7)$ reconstruction show here as arcs of short dashes. After

[1] reducing the valve opening to a third of its precedent value with a speed of 60mils/s

[2] lowering the valve opening to 0 with a speed of 0.1mils/s

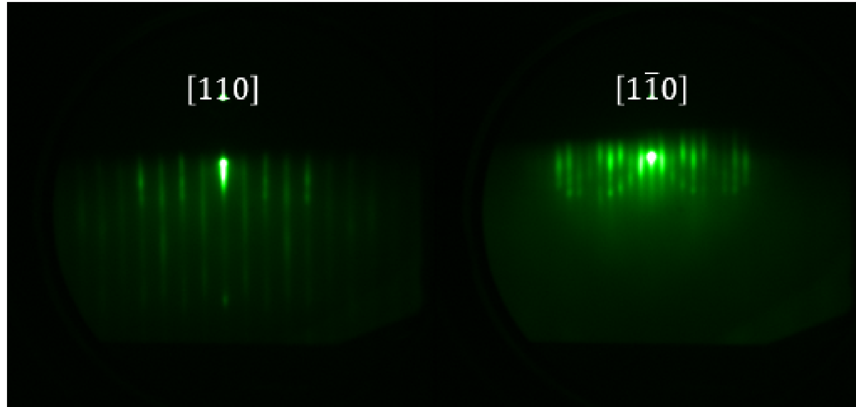


(a) GaAs $(2 \times 4)$ surface reconstruction

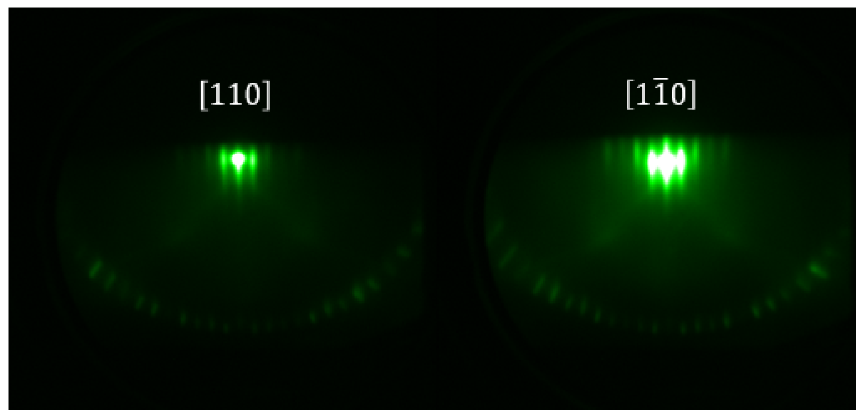


(b) $GaAs(001) - (4 \times 4)$ reconstruction

Figure 3.12: $GaAs(001)$ surface reconstructions used in this project observed with RHEED.

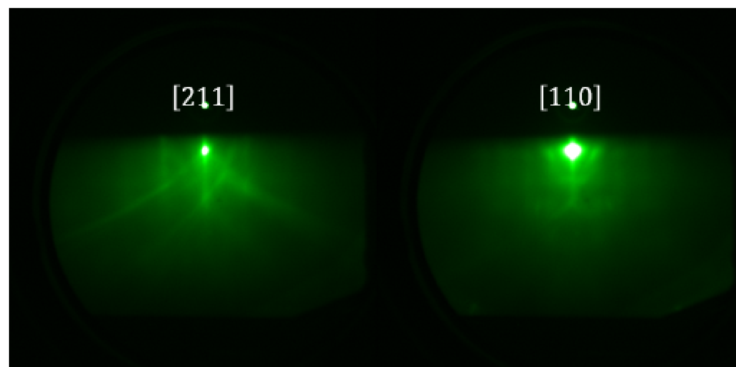


(a) $Si(111) - $ "$(1 \times 1)$"

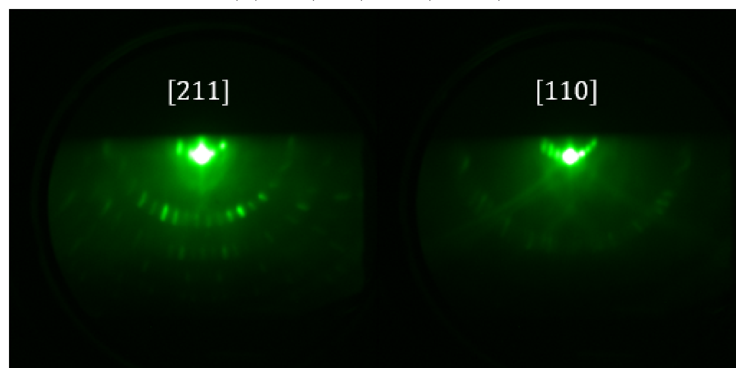


(b) $Si(111) - (7 \times 7)$

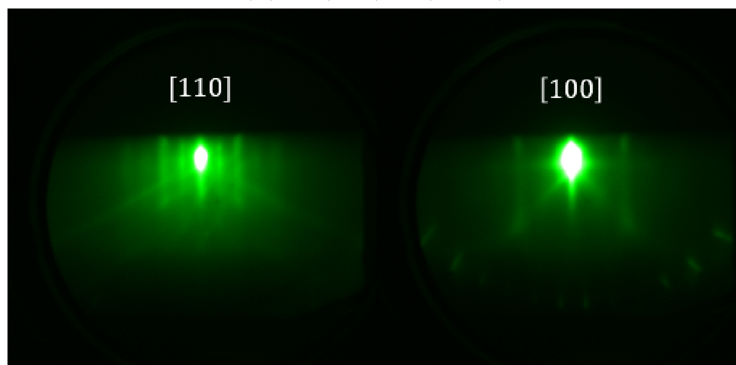


(c) $Si(001) - (2 \times 1)$

Figure 3.13: $Si(001)$ and $Si(111)$ surface reconstructions used in this project observed with RHEED

the switch, the cooling rate could be increased to 30°C/min. When the cooling rate was not slowed down for the reconstruction switch and maintained at 30°C/min, the "$(1 \times 1)$" was conserved down to low temperatures (Figure 3.13a). For $Si(001)$, the reconstructed phase stayed $(2 \times 1)$ over cooling as shown on Figure 3.13c. After obtaining the desired reconstructed surface, the substrate temperature was lowered to 300°C and maintained there until the background pressure of the module dropped below $1.2 \times 10^{-10}$Torr. This was done to avoid condensation on the surface of $As$ molecules which background level elevates as a result of heating some of the $As$ coated surfaces during the high-temperature treatment of the substrates. The wafers were then let to cool during 16 hours with no power applied to the heater. To avoid all sources of contamination during this phase, the main shutter and all the heated viewports were closed, the latter being also powered off. The beam flux monitoring ion gauge and RGA were also powered off for this stage. RHEED patterns were checked before and at the end of the cooling period to make sure that the surface remained clean and smooth over this period. RHEED patterns remained unchanged for all wafers during this process. Substrate temperature, as measured with BandiT BET system, prior to commencing Al deposition was −7°C, while the manipulator thermocouple showed temperature of 5°C.

### 3.3.5 *Al* epitaxy

The *Al* source used in this project has a purity of 99.99995%. *Al* was evaporated from a Dual filament SUMO cell (Veeco Instruments Inc). A 1100Å-thick *Al* layer deposited at a rate of 0.5Å/s. Opening of the *Al* cell shutter exposed the wafer to a source of radiative heat (the cell temperature was about 1110°C), which resulted in a gradual increase in the substrate temperature during the *Al* layer deposition. According to BandiT, the substrate temperature increased by less than 12°C during the deposition. This is in good agreement with the increase of substrate temperature due to radiation from evaporation source estimated by Hasan *et al* [68], considering that their effusion cell temperature is below the range used in the experiments reported here (960°C). As mentioned earlier, the triggering unit (kSA RMAT, k-Space Associates Inc.) allowed observing RHEED patterns sequentially at four azimuths while growing on the rotating wafer. After deposition of

the $Al$ layer, the wafer was taken out of the system for structural and morphological characterization.

# Chapter 4

# Results

## 4.1 Preliminary observations

This section compiles preliminary observations about the substrate preparation and the growth environment.

### 4.1.1 Study of the wet cleaning techniques

The effect of some wet cleaning techniques was investigated by the Digital Quantum Matter Laboratory from the Institute of Quantum Computing (University of Waterloo). AES, X-Ray Photoelectron Spectroscopy (XPS) and Secondary Ion Mass Spectrometry (SIMS) were used to assess the types and level of contaminants on clean and as supplied $Si$ wafers. As a preliminary test, an as-supplied sample and a fully cleaned sample (namely by degreasing, RCA, and $HF$ dip) were directly compared to evaluate the overall efficiency of the cleaning. $C$ and $O$ levels were found to be below the detection limit of AES and XPS for both samples. This shows the high quality of the epi-ready wafers as delivered by the manufacturers. Other contaminants, such as Iron and Copper, were found on all surfaces. These contaminants likely originate from the Nitrogen line (made of Copper) used to purge the transport chamber of the wafers. SIMS analysis confirmed that the oxide layer was

thinner in the case of cleaned samples and that it was the main source of $C$ contamination. These results indicated that further investigation of all the wet cleaning steps was unnecessary. The epi-ready wafers seem to have a very high-quality and could be loaded directly into the deposition system for *in-situ* cleaning and oxide desorption. Moreover, this study highlighted that a wet cleaning procedure should be realized in the MBE lab in order to load the wafer immediately after preparation, so as to avoid the transport step which incorporated more contaminants on the substrate.

### 4.1.2 Effect of the *in-situ* contaminants

The possible sources of *in-situ* contamination are reviewed here and justify the precautions taken in the experiments.

#### Effect of the pumping system

While UHV is maintained in the growth system, some parts of the equipment could still contribute to *in-situ* contamination. One of the primary sources of *in-situ* contamination is the presence of pumps such as rotary vane pump using hydro-carbon-based oil. Although such pumps are not used in the Veeco GEN10 system, it seems important to mention their possible impact on the devices quality. Caroll *et al* [46] studied the impact of a prolonged stay of the wafer in different parts of a UHV-Chemical Vapor Deposition system. They pointed out that the use of the rotary vane led to barely detectable $C$ and $CO$ levels (even after 6 cycles), far less important than for a wafer exposed to the fume hood for $10min$. It should be mentioned that a $5min$ stay in the LL with the door slightly open only added a small increase of $C$ and $CO$ contamination. Finally, no contaminants could be detected on the SIMS analysis after a $15min$ stay in the growth chamber, indicating that the reactor itself does not add to the contamination.

#### Effect of the ion gauge

The growth system appears therefore to be a minor source of contamination. However, it has been proven by Missous *et al* [63] that the presence of an ion gauge in the growth

system has an impact on the growth output in the case of $Al/GaAs$. Indeed, while they consistently observed only the (100) orientation of $Al$ on $GaAs(001) - (4 \times 4)$ ($As$-rich) when they switched off the ion gauge over cooling down of the substrate before epitaxy, a mixture of $Al(100)$ and $Al(110)$was obtained if such precaution was not taken. The ion gauge presence did not impact growth results for the case of $GaAs(001) - (2 \times 4)$ ($As$-stable) nor $GaAs(001) - (4 \times 6)$ ($Ga$-rich). One could imagine that the heated filament of the gauge might desorb gases and add contaminants to the layer, therefore changing its structure and morphology and leading to the growth of different orientations. The authors also suggested that the gauge could ionize or excite some molecules present in the reactor, causing damage to the surface (by collision or chemical reaction). Previous work by Pianetta *et al* [86] also demonstrated that the ion gauge enhanced the oxidation (adsorption of oxygen) on $GaAs(110)$ surfaces by orders of magnitude. A similar observation was made on $Si(111)$ substrates [87]. Missous *et al* [63] tried to monitor the background pressure composition on switching on and off of the gauge but could not notice any change.

#### Effect of the cryopanels

The contribution of the cryopanels was also studied by Missous *et al* [63]. It was shown that the use of cryopanels changed significantly the growth output, yielding (100) phase "only" (with (110) amounting to less than 10% of the total area) for all three reconstructions. Having eliminated the fluctuating (100) + (110) mixed phase, the authors concluded that the use of the cryopanels led to more consistency in the results. Furthermore, the RHEED streaks appeared to be sharper than previously, likely indicating a smoother surface when the cryopanels were used.

#### Consequences for this project

In view of the aforementioned considerations, we decided to shut down the beam flux monitoring instrument's ion gauge during the substrate cooling down and epitaxial growth steps. Additionally, we cooled down and closed the heated viewports to avoid any desorption from them and suppress a potential source of radiative heating of our substrate (which aimed at

the lowest temperature possible). Finally, the main shutter was set in front of the substrate during the whole cooling procedure as an extra-precaution for preventing contaminants to reach the surface. These measures aimed at minimizing the level of contaminants at the starting surface. They were also crucial to the reproducibility of the growth results, as literature has demonstrated. The effect of these precautions was visible on the RHEED pattern: upon cooling with the ion gauge on, with heated viewports and no main shutter protection, the RHEED pattern of the surface got dimmer and blurrier over time whereas this did not happen when taking all the necessary precautions (see Figure 4.1).

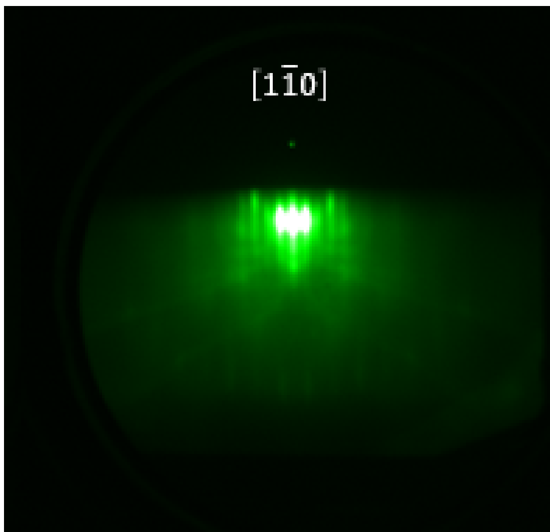


(a) Surface cooled down with the ion gauge off, the heated viewports powered off and closed and the main substrate placed in front of the substrate.

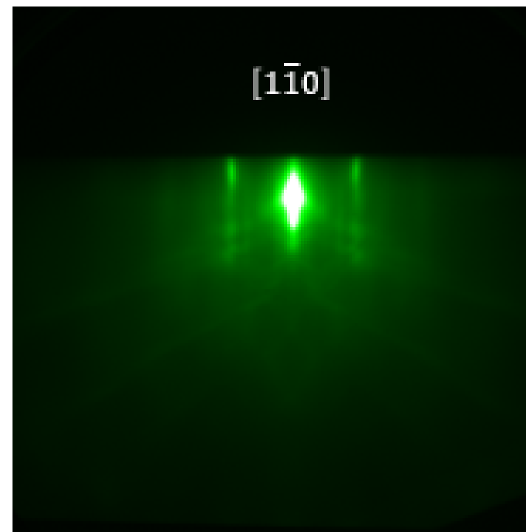


(b) Surface cooled down without preventing *in-situ* contamination (ion gauge on, heated viewports on and open and main shutter not placed)

Figure 4.1: Comparison between the RHEED patterns of a $GaAs(001) - (2 \times 4)$ surface cooled down without preventing *in-situ* contamination and a $GaAs(001) - (2 \times 4)$ surface cooled down without these precautions.

## 4.2 $Al$ epitaxy on $GaAs$

Here are presented the results of the epitaxy of $Al$ on $GaAs$. Two surface reconstructions were investigated: the $As$-stabilized $GaAs(001)-(2\times 4)$ and the $As$-rich $GaAs(001)-(4\times 4)$. The $Ga$-rich and stabilized reconstructions, such as $GaAs(001)-(4\times 6)$, were not investigated because being judged too unsafe for the purpose of resonators applications. Indeed, if not handled properly, $Ga$ droplets could form during the reconstruction preparation and cause electrical defects in the device. Additionally, these surfaces are more sensitive to interdiffusion phenomena.

### 4.2.1 $Al$ epitaxy on $GaAs(001)-(2\times 4)$

#### RHEED observations

The growth was realized by steps of 0.5ML at a time, allowing a minute between each step for the surface to evolve. The evolution of the diffraction pattern suggests a Stranski-Krastanov growth mode as shown on Figure 4.2 and 4.3. In all of the following sections, the error in calculated sizes of the reconstruction pattern which results from the accuracy of measurement of the distance between RHEED streaks was ±0.3Å. This does not allow to discriminate between strained and relaxed layers, nor between $GaAs$ and $AlAs$ lattice parameters but, for most cases, was accurate enough for positive *in-situ* identification of the crystallographic orientation of the $Al$ layer with respect to the substrate. These estimates are refined with the subsequent XRD analyses.

Changes in the RHEED pattern of the $GaAs(001)-(2\times 4)$ surface reconstruction indicative of the formation of a wetting layer were observed immediately after opening the $Al$ shutter. Namely, after deposition of 1ML of $Al$, the pattern transformed from the $(2\times 4)$ reconstruction to a $(1\times 4)$ reconstruction which persisted until the end of the third monolayer deposition. In the [110] RHEED direction, the interplanar spacing calculated after deposition of 1ML and 2ML of $Al$ was indeed 5.6Åwhich corresponds to the bulk $GaAs(001)$ (Table 4.1). This indicates that the $Al$ nucleation broke the dimeric bonds of the top $As$ atoms along the $[1\bar{1}0]$ direction $(2\times 4)$ reconstruction (along the rows), likely by

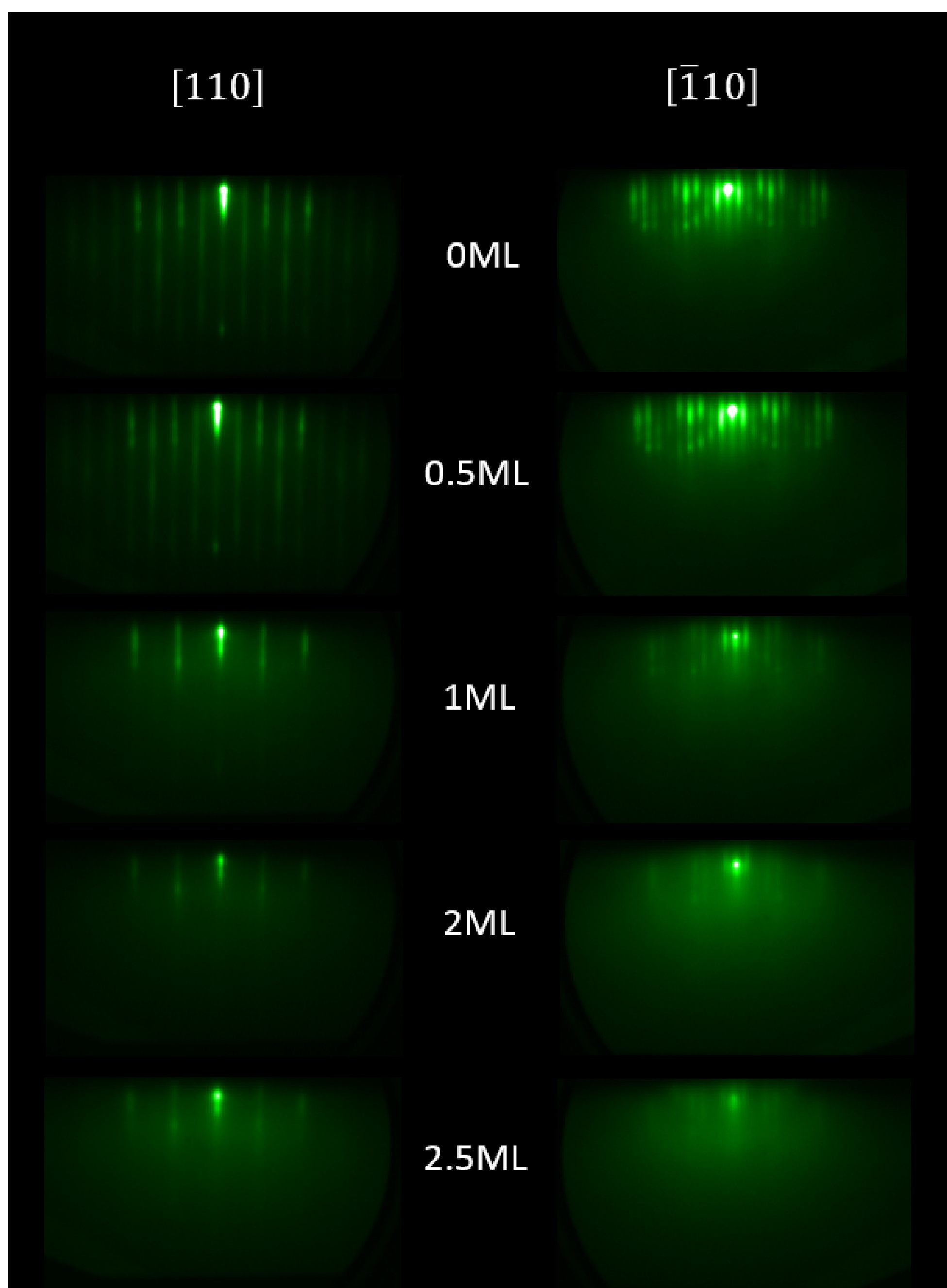


Figure 4.2: RHEED observations in the [110] $GaAs$ direction (left) and in the [$\bar{1}$10] $GaAs$ direction (right) of the $Al$ nucleation on $GaAs(001) - (2 \times 4)$.

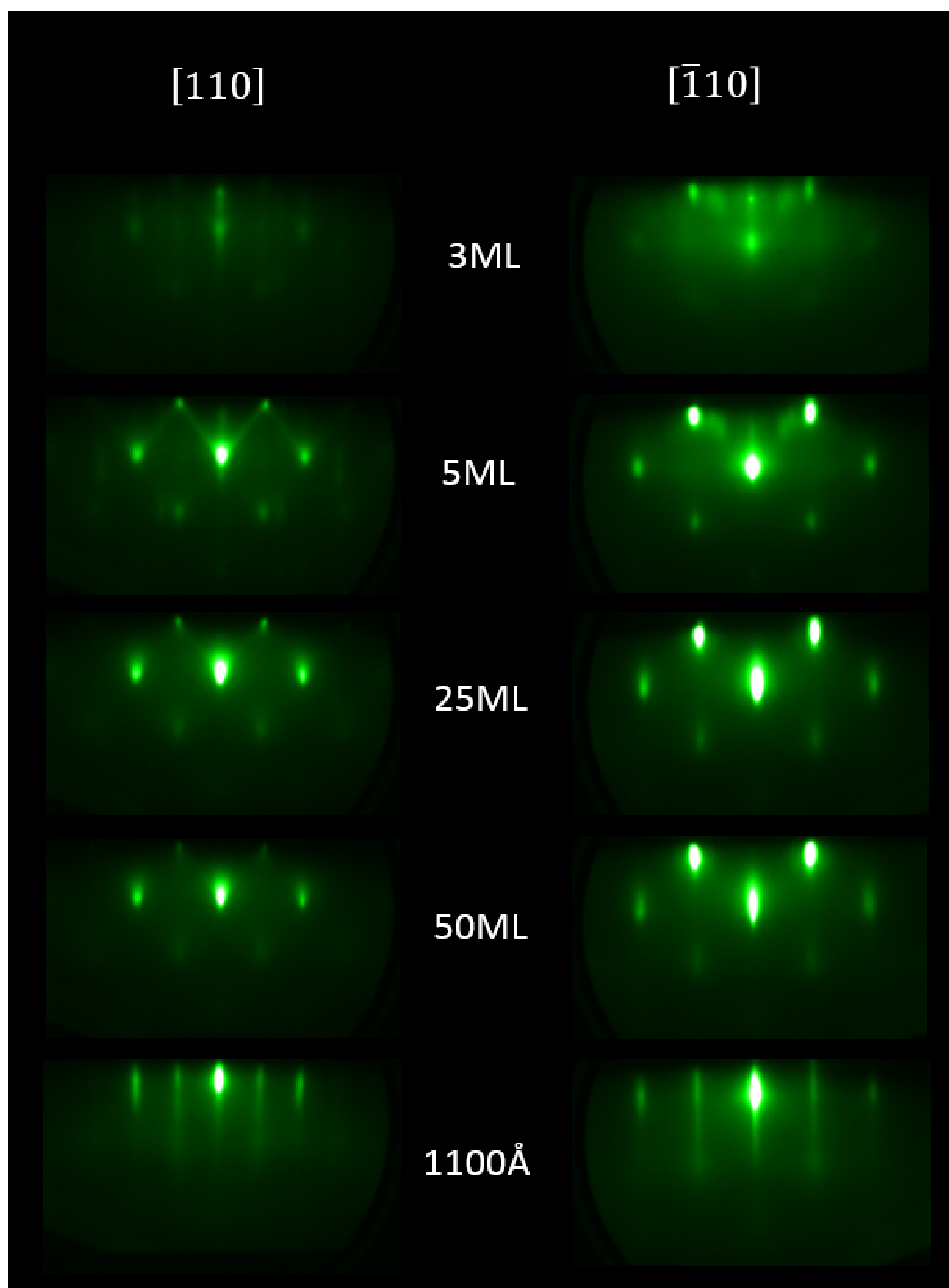


Figure 4.3: RHEED observations in the [110] $GaAs$ direction (left) and in the [1$\bar{1}$0] $GaAs$ direction (right) of the $Al$ islands coalescence on $GaAs(001)-(2 \times 4)$.

Table 4.1: Lattice parameters computed from RHEED observations. The 0° azimuth corresponds to the RHEED [110] direction.

| Thickness | Azimuth (°) | Reciprocal spacing (pixels) | Computed real spacing (Å) | Computed lattice parameter (Å) | Expected lattice parameter (Å) |
|---|---|---|---|---|---|
| 0ML | 0 | 48.8 | 8.0 | 5.7 | 5.7 ($GaAs$(001)) |
| | 90 | 23.6 | 16.6 | 5.8 | 5.7 ($GaAs$(001)) |
| 1ML | 0 | 99.3 | 3.9 | 5.6 | 5.7 ($GaAs$(001)) |
| | 90 | 23.6 | 16.5 | 5.8 | 5.7 ($GaAs$(001)) |
| 1100Å | 0 | 98.0 | 4.0 | 4.0 | 4.1 ($Al$(110) along the [001] direction) |
| | 90 | 137.3 | 2.8 | 2.8 | 2.9 ($Al$(110) along the [$\bar{1}$10] direction) |

forming $AlAs$ (see Figure 4.4). In the orthogonal [$\bar{1}$10] RHEED direction, the $\times 4$ pattern was preserved but got dimmer with increasing $Al$ coverage. This could be interpreted as the $Al$ atoms filling the trenches between the rows of dimers and hence adding disorder to the structure in the [110] direction. This suggests the formation of a partially ordered wetting layer and is consistent with the observations of Donner *et al* [59].

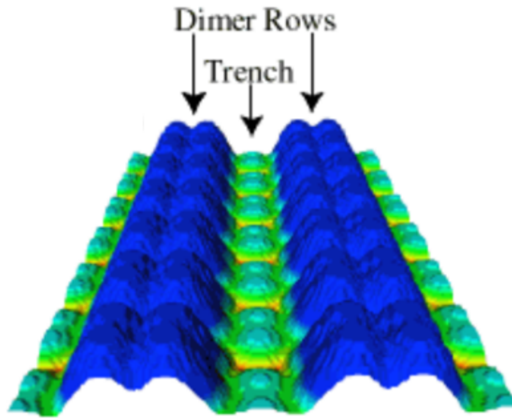


Figure 4.4: $3D$ representation of the $GaAs(001) - (2 \times 4)$ reconstruction. Adapted from [88]

The fact that the pattern in the $[\bar{1}10]$ direction weakened while the pattern in the [110] direction displayed sharp streaks could be interpreted as the growing $Al$ being in good registry with the underlying $GaAs$ substrate in only the $[\bar{1}10]$ direction, while facing a substantial misalignment in the [110] direction. This is understandable judging by how the tetragonal $Al(110)$ structure would match the rotated cubic $GaAs$ structure (Figure 4.5). The mismatch could easily be accommodated and would only amount to 1.30% in the $[\bar{1}10]$ direction. However, in the [110] direction, only the stacking of 8 $Al$ atoms to 6 $As$ atoms would be able to accommodate the mismatch to a satisfying level (0.28%). Such a complex arrangement could generate dislocations and stress. This hypothesis is confirmed by the interplanar spacing computed from the final RHEED streaks presented in Table 4.1.

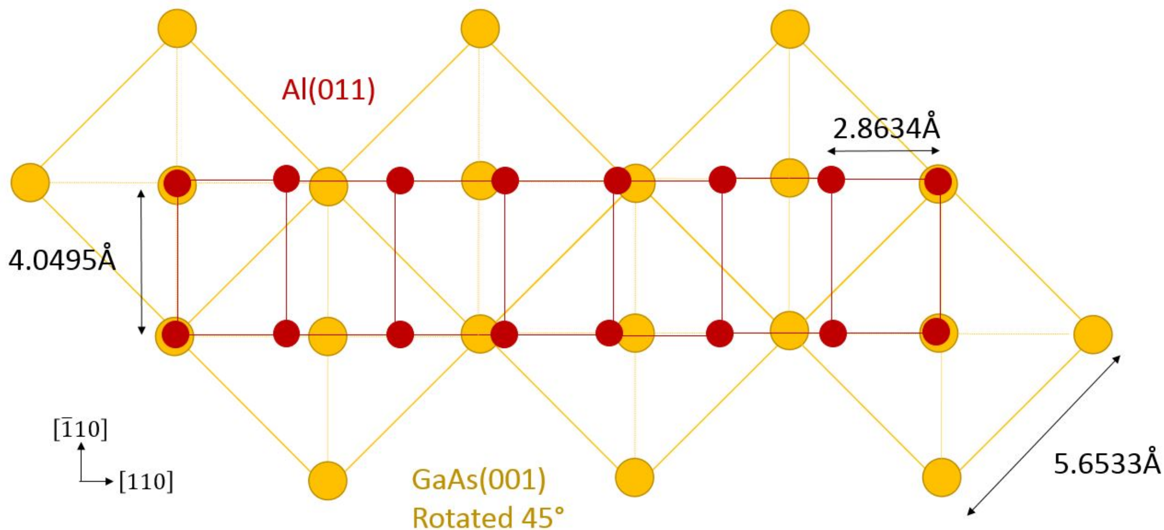


Figure 4.5: $Al(011)$ matching to $GaAs(001)$ surface. $Al$ atoms are in red and $As$ atoms in yellow.

After deposition of the first three monolayers, features indicative of $3D$ islands formation started to appear, as can be seen on Figure 4.3. Interestingly, these islands seemed to coalesce at different rates in the two directions. Indeed the spotty pattern persisted up to 25ML in the $[\bar{1}10]$ direction and up to 50ML in the [110] direction, after which the pattern smoothed gradually. This reveals that the $Al$ mobility was higher in the $[1\bar{1}0]$ direction, along what were initially the trenches. The islands were therefore elongated

in this direction and coalesced faster than in the orthogonal [110] direction. The surface kept smoothing until the end of the growth, the RHEED streaks gaining sharpness with increasing thickness.

After 1100Å, the RHEED pattern showed sharp lines in the $GaAs$ directions and also 35° and 55° off these azimuths. This implies firstly that the growth was epitaxial and reached an atomically smooth surface, and secondly that the surface orientation is not a cubic (100) but a rectangular (110) plane (Figure 4.6) where the diagonal planes are 35° and 55° off (not 45° off) the $GaAs$ $[1\bar{1}0]$ and [110] directions. From the spacing between the streaks, the distances between the planes were computed (Table 4.1). It was deduced from the patterns that the surface had a $(1 \times 1)$ reconstruction.

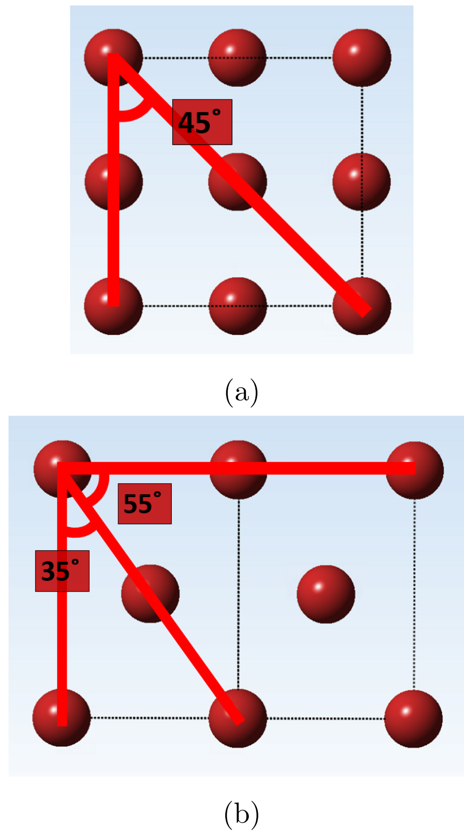


(a)

(b)

Figure 4.6: Top-view of the $Al(100)$ and $Al(110)$ phases showing the angles between different planes.

**HRXRD structural analysis**

The structural properties of the grown materials were further studied with an HRXRD system (Bruker D8 ADVANCE). First, a coupled $2\theta$-$\omega$ scan was performed, which is presented on Figure 4.7a. Strong signal counts from the buffer structure were registered, but the peak at $2\theta = 64.992°$ could clearly be identified as the $Al(220)$ phase. Increased noise was also observed at the $Al(220)$ and $Al(111)$ positions but in amounts too weak to be identified as peaks. The sample was then tilted by 45° ($\Psi$ axis) and rotated by 88° ($\Phi$ axis) to observe the $Al(200)$ peak at $2\theta = 44.719°$, confirming the phase orientation (Figure 4.7b). The calculated lattice constant of the $Al$ film was 4.0498Åfrom the (200) peak and 4.0554Åfrom the (220) peak which are both close to the bulk value of 4.0495Å. The $Al$ film was therefore fully relaxed. It should be mentioned that the $Al(220)$ peak was twice as sharp as the $Al(200)$ peak with a Full Width at Half Maximum of $FWHM(220) = 0.214°$ while $FWHM(200) = 0.425°$, with a substrate $FWHM$ below 0.1°. This could be due to relaxation of strain leading to tilt of the crystallites or low angle grain boundaries, both resulting from the Stranski-Krastanov growth mode (during the $3D$ islands coalescence). Finally, a $\Phi$ scan, with $2\theta$ set towards $Al(200)$ diffraction and the wafer tilted to $\Psi = 45°$, was performed to validate the epitaxial character of the grown layers (Figure 4.8). The number of peaks and the angular spacing between them support our hypothesis: only two diffraction peaks were observed for the $Al(200)$ with a full 360°$\Phi$ rotation, confirming the rectangular projection of $Al(220)$ onto the substrate. Moreover, these peaks were oriented 45° off the $GaAs(200)$ peaks which proves that the observed epitaxial relationship is $Al[110]/GaAs[100]$ with $Al[100]//GaAs[110]$.

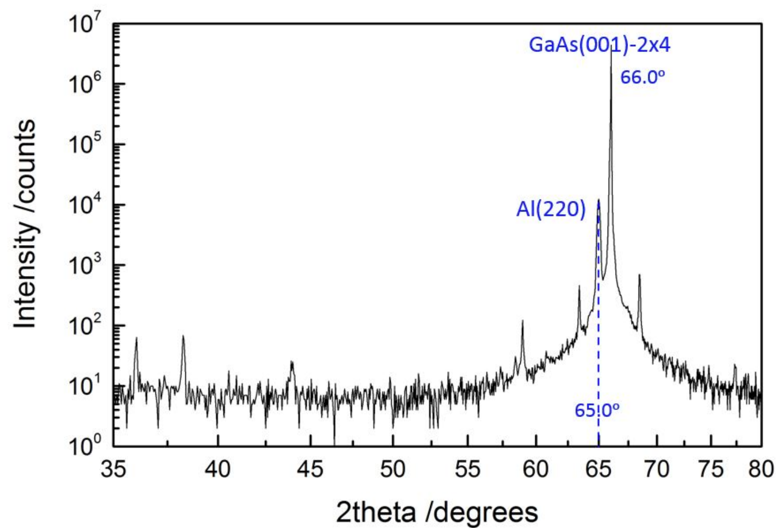


(a) Coupled scan at $\Psi = 0°$

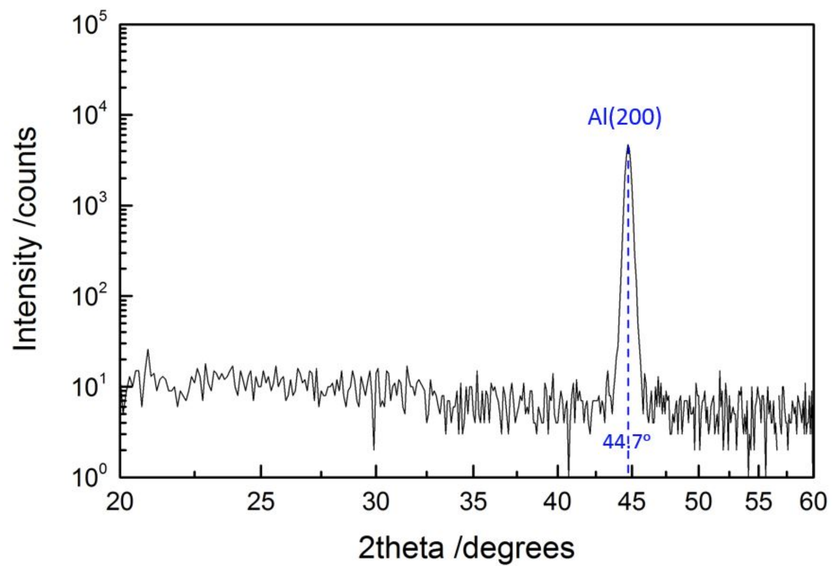


(b) Coupled scan at $\Psi = 88°$

Figure 4.7: Measured High Resolution XRD results for $Al/GaAs(001) - 2 \times 4$ epitaxy.

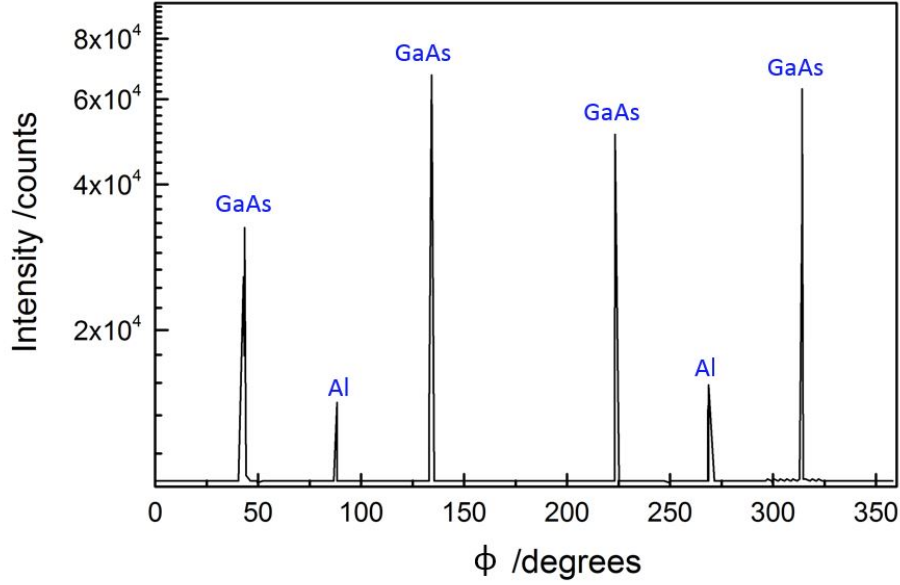


Figure 4.8: Φ scan

#### Morphological study

While the RHEED streaky pattern is already a good indicator of a smooth surface, we decided to investigate further its topology. The morphology study involved immediate visual observation of the wafers upon exiting the system, DIC microscopy and AFM. The surface appeared completely featureless under the microscope, with very few defects, as shown on Figure 4.9.

A $1 \times 1\mu$m AFM scan and a line section (Bruker NanoScope Analysis) are presented in Figure 4.10. The estimated RMS roughness over a $5\mu\text{m}^2$ area was 0.552nm which is roughly equivalent to $\sim$ 2ML confirming the atomic smoothness. This roughness is equivalent to the one of the best samples described in the literature [4] in the patterning of superconducting resonators on Sapphire (0.4nm). A $3D$ reconstruction of the surface was generated with the Nanoscope Analysis software as displayed on Figure 4.11. It can be seen on this figure than the surface topography features are elongated in the $[1\bar{1}0]$ direction, which is consistent with the previous finding of enhanced mobility in this direction compared to the orthogonal

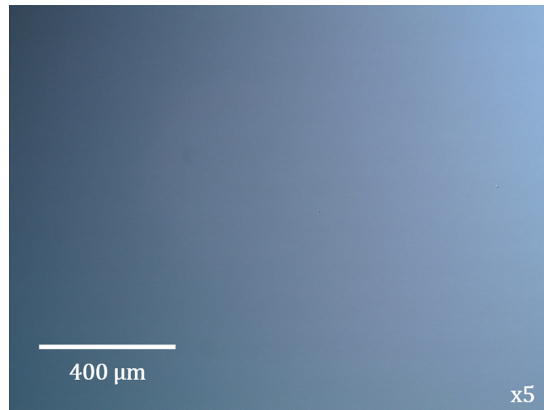


(a) ×5 magnification

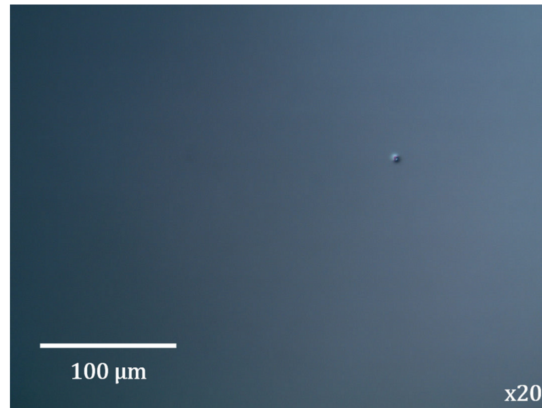


(b) ×20 magnification

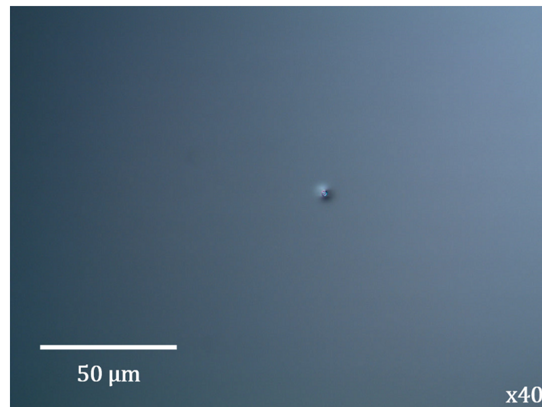


(c) ×40 magnification

Figure 4.9: Nomarski observations for Al/GaAs-(2 × 4).

direction.

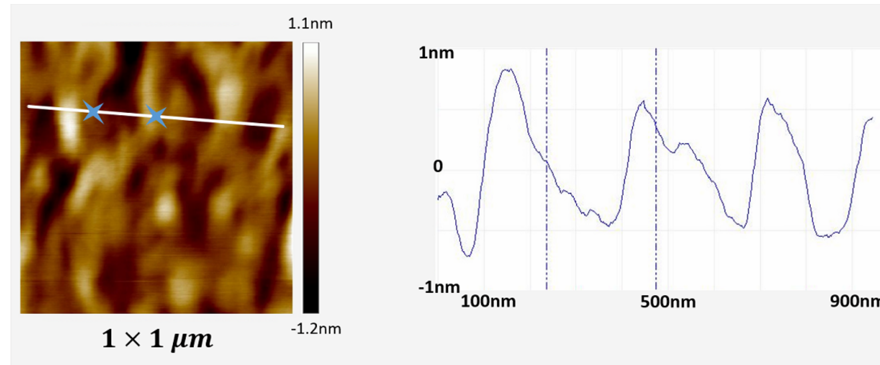


Figure 4.10: $1 \times 1 \mu m$ AFM scan of an $Al/GaAs(001) - (2 \times 4)$ sample and the associated line section. The depth profile on the right corresponds to the white line on the left scan and markers on this line are represented by dotted lines on the depth profile.

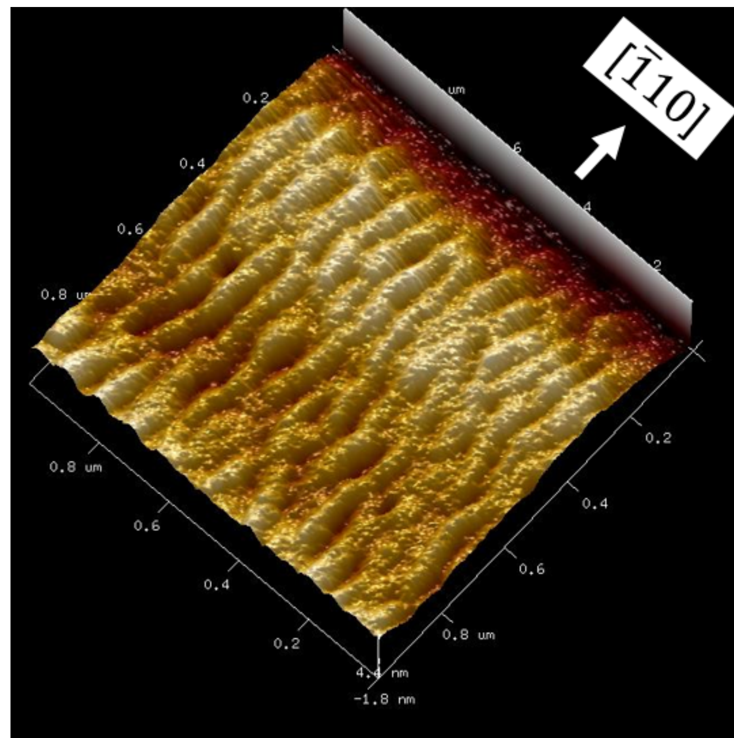


Figure 4.11: $3D$ reconstruction of the $Al/GaAs(001) - (2 \times 4)$ surface (Nanoscope Analysis).

### 4.2.2 $Al$ epitaxy on $GaAs(001) - (4 \times 4)$

As a comparison with the $GaAs - (2 \times 4)$, we investigated the $Al$ epitaxy on an $As$-rich $(4 \times 4)$ surface. While the $(2 \times 4)$ reconstruction has a full monolayer of $As$ on top of the surface, the $(4 \times 4)$ reconstruction is believed to correspond to a 1.75ML $As$ coverage [22]. As is explained below, this resulted in different crystallographic orientation of of the $Al$ layer.

#### RHEED observations

From 0 to 0.5ML coverage, the RHEED pattern transformed briefly to lines whose spacing corresponds to the bulk $GaAs(001)-(1\times1)$ (computed interplanar spacing 5.6Åas shown on Table 4.2). This indicates the formation of a wetting layer in registry with the substrate in both directions. The difference between this layer and the one obtained previously could stem from the different step configuration (between the dimer rows on the $(2 \times 4)$ reconstruction for example) for the involved reconstruction. However, simulations would be required to validate this hypothesis. Once again, the wetting layer is likely formed of $AlAs$, the $As$ being abundant at the interface. The streaky pattern then fainted gradually until completely disappearing after 2ML as shown on Figure 4.12. This is likely due to a disordered $Al$ phase nucleating on top of the wetting layer. Features indicative of $3D$ islands formation appeared with the deposition of the third monolayer in both directions. However, they only persisted in the $[\bar{1}10]$ direction, where they eventually gave way to smoothed streaks. Similar lines appeared at the azimuths 60°, 120°, 180°, 240° and 300° away from the $[\bar{1}10]$ direction which suggest a hexagonal surface, such as $Al(111)$. Unfortunately, their evolution during the growth could not be observed with the RHEED, the triggered azimuths being set beforehand to 45° spacing between observed azimuths. The final RHEED pattern consisted of sharp streaks positioned 60° apart from each other, consistent with an $Al(111)$ phase. At the end of the growth these streaks could be investigated with the RHEED on the static wafer. The computed surface unit cell dimensions, shown in Table 4.2, correspond indeed to the $Al(111)$ orientation. The presence of the $Al(111)$ phase was further confirmed with an XRD study.

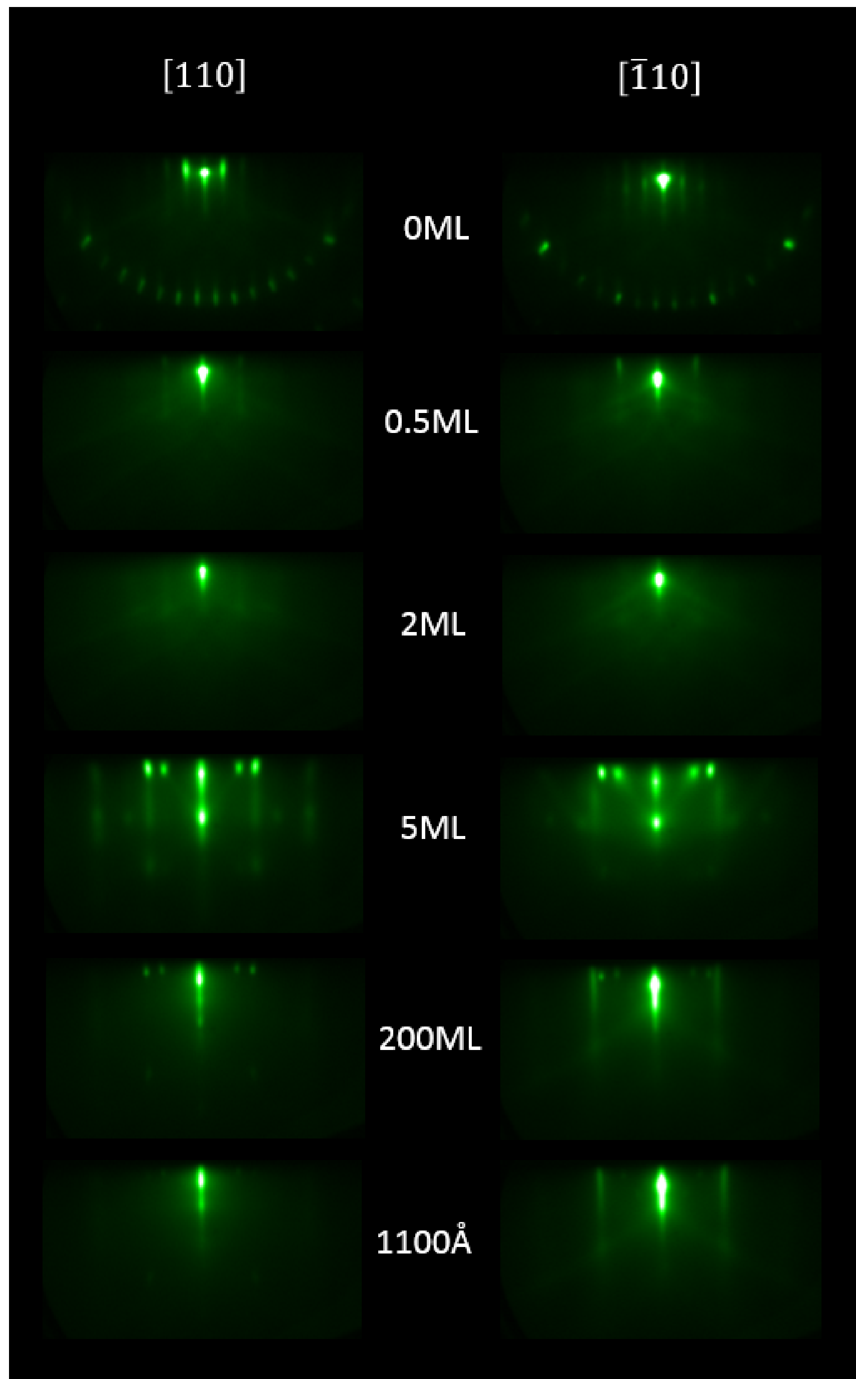


Figure 4.12: RHEED observations in the [110] $GaAs$ direction (left) and in the [1$\bar{1}$0] $GaAs$ direction (right) of the $Al$ epitaxy on $GaAs(001) - (4 \times 4)$.

Table 4.2: Lattice parameters computed from RHEED observations. The 0° azimuth corresponds to the RHEED [110] direction.

| Thickness | Azimuth (°) | Reciprocal spacing (pixels) | Computed real spacing (Å) | Computed lattice parameter (Å) | Expected lattice parameter (Å) |
|---|---|---|---|---|---|
| 0ML | 0 | 49.0 | 7.9 | 5.6 | 5.7 ($GaAs(001)$) |
| | 90 | 48.6 | 8.0 | 5.6 | 5.7 ($GaAs(001)$) |
| 1ML | 0 | 97.6 | 4.0 | 5.6 | 5.7 ($GaAs(001)$) |
| | 90 | 96.5 | 4.0 | 5.7 | 5.7 ($GaAs(001)$) |
| 1100Å | 0 | 160.6 | 2.4 | 2.4 | 2.3 ($Al(111)$) |
| | 60 | 159.1 | 2.4 | 2.4 | 2.3 ($Al(111)$) |

#### HRXRD structural analysis

Although the RHEED only showed streaks at the hexagonal azimuths, the detailed XRD observation (Bruker D8 ADVANCE) revealed the existence of residual (200) and (220) phases (Figure 4.13). The relative intensity of the peaks was not consistent across the samples, not allowing to study the composition of the grown phase, even though the $Al(220)$ peak appeared to be consistently weaker than the two other peaks. Since the samples were polycrystalline, they were not investigated further with a $\phi$ scan to determine the orientation of the epilayers in relation with the substrate. Polycrystalline materials are expected to host more TLS than single crystalline materials, leading to a hindered performance of the resonators.

#### Morphological study

Because the grown material was polycrystalline, hence expected to be rougher, only one sample was studied with AFM to have an idea of the roughness magnitude, but its variation across multiple samples was not investigated. The RMS roughness measured on one representative sample was 1.2nm, which is twice the roughness of the $(2 \times 4)$ samples. A $1 \times 1\mu$m AFM scan and its line section are displayed in Figure 4.14. However, all samples displayed featureless surfaces in both visual and DIC inspection as shown on Figure 4.15. The level of point defects observed with Nomarski was similar to the $(2 \times 4)$ samples.

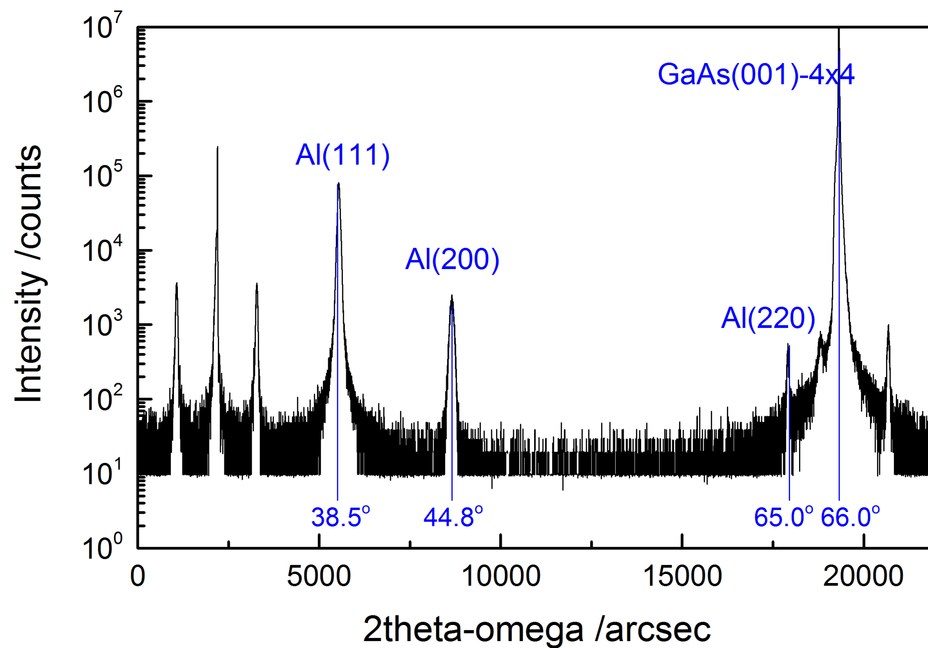


Figure 4.13: Coupled scan of the $Al/GaAs(001) - (4 \times 4)$sample. Unlabeled peaks correspond to the $GaAs$ substrate and the $AlAs/GaAs$ superlattice.

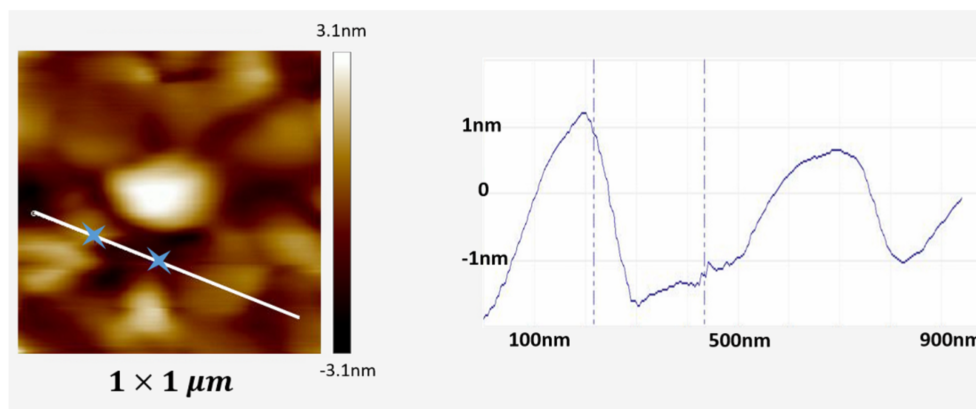


Figure 4.14: $1 \times 1 \mu m$ AFM scan of an $Al/GaAs(001) - (4 \times 4)$ sample and the associated line section. The depth profile on the right corresponds to the white line on the left scan and markers on this line are represented by dotted lines on the depth profile.

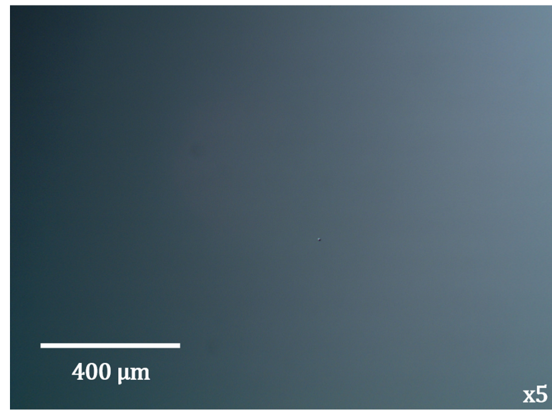


(a) ×5 magnification

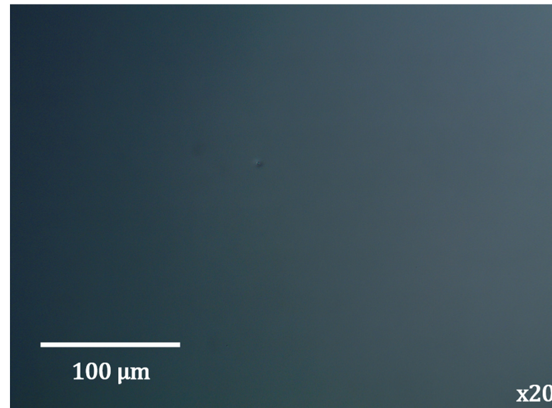


(b) ×20 magnification

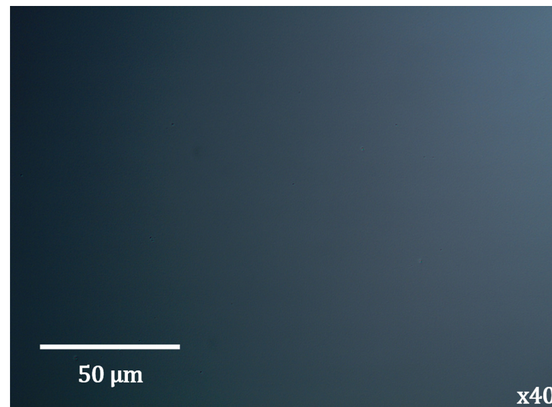


(c) ×40 magnification

Figure 4.15: Nomarski observations for $Al/GaAs-(4\times 4)$.

### 4.2.3 Other parameters

**Effect of the buffer structure**

The purpose of the superlattice is to trap segregating impurities at the heterogeneous interfaces. *Al* layers were also grown on plain 2000Å-thick *GaAs* buffers to investigate the actual impact of the superlattice. The obtained phase when nucleated on a $(2 \times 4)$ reconstruction was again (110), as proved by the XRD study. Other than an overall reduced noise level, the diffraction pattern displayed absolutely no increase in intensity at the expected positions of the (200) and (111) peaks as shown on Figure 4.16. The morphology analysis, however, showed that even though the surface appeared to be as smooth as the samples grown on the superlattice buffer, a slightly higher amount of defects was observed (Figure 4.17). Overall, these samples did not present significant differences with the samples grown with the superlattice, as expected.

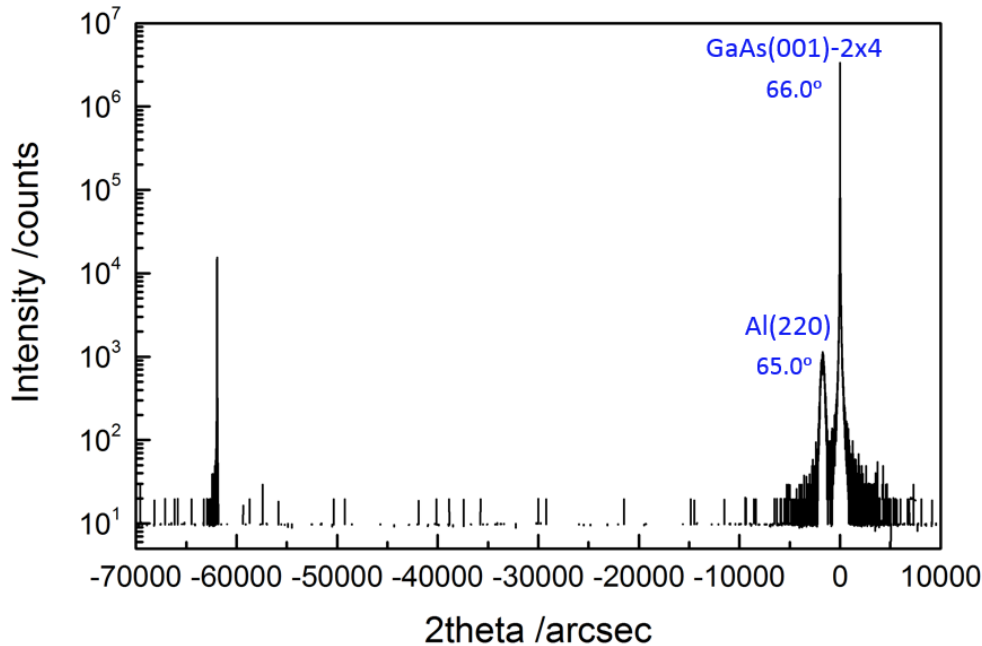


Figure 4.16: Coupled scan of the *Al* epitaxy on a simple buffer structure on a *GaAs* substrate.

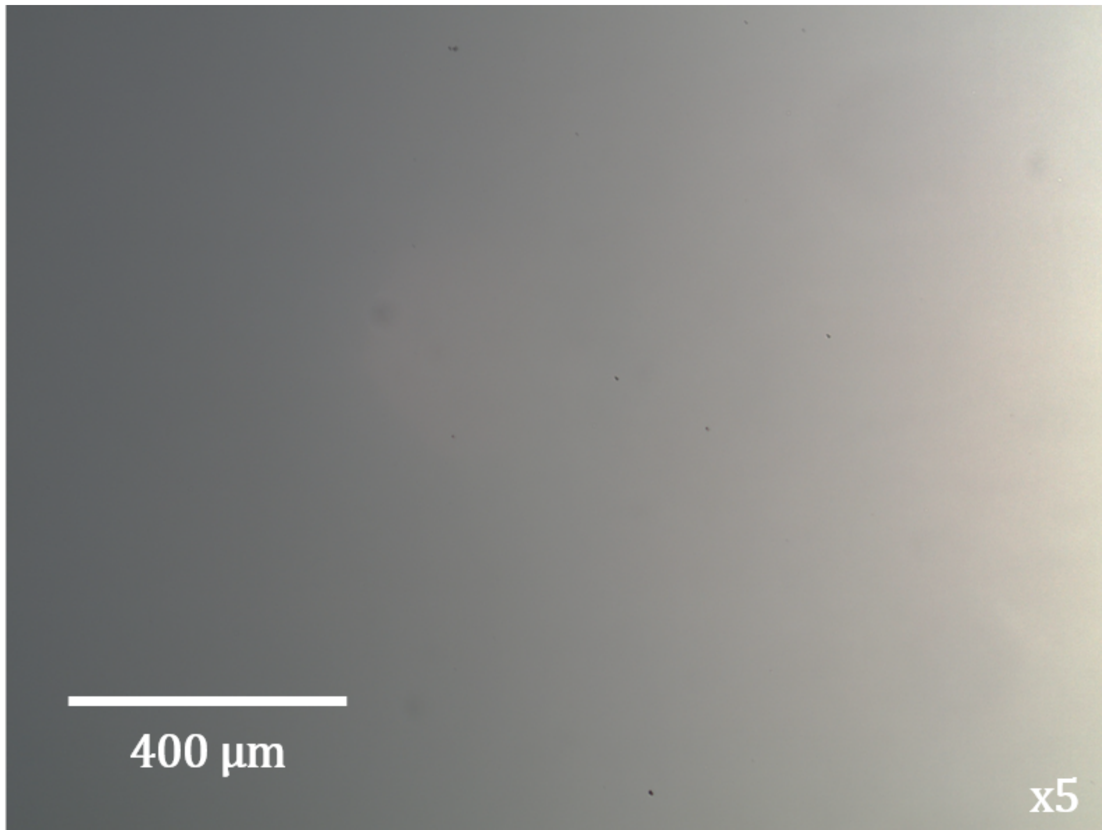


Figure 4.17: $\times 5$ microscope observation of an $Al/Si$ sample grown on a simple buffer structure.

**Effect of the temperature**

A growth on a $GaAs(001)-(2\times4)$ substrate was realized also at higher temperature (50°C) to investigate the importance of the low temperature epitaxy. It was attempted to fit the RHEED intensity profiles to the Arrhenius law but the time scale was too large to provide any accurate result. The difficult estimation of the changes in the surface temperature due to the opening and closing of the cell shutter also complicated the task. Nevertheless, the RHEED observations revealed that $3D$ islands started nucleating one monolayer earlier at 50°C than in the low temperature case as shown on Figures 4.18, 4.19 and 4.20, showing different scanning regions of the image. Final RHEED patterns were similar to the ones obtained for low temperature growth but with dimmer intensity.

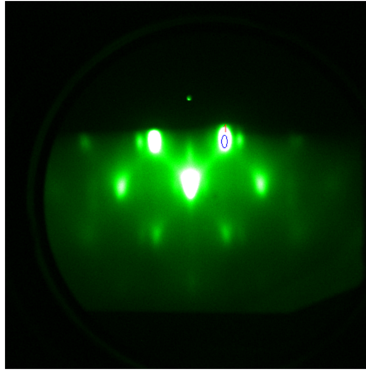

(a) Scanning region

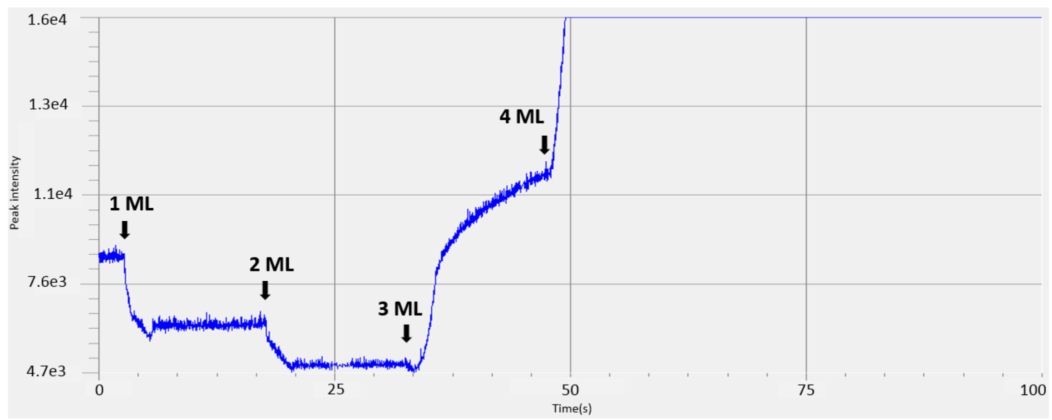


(b) $-7°C$

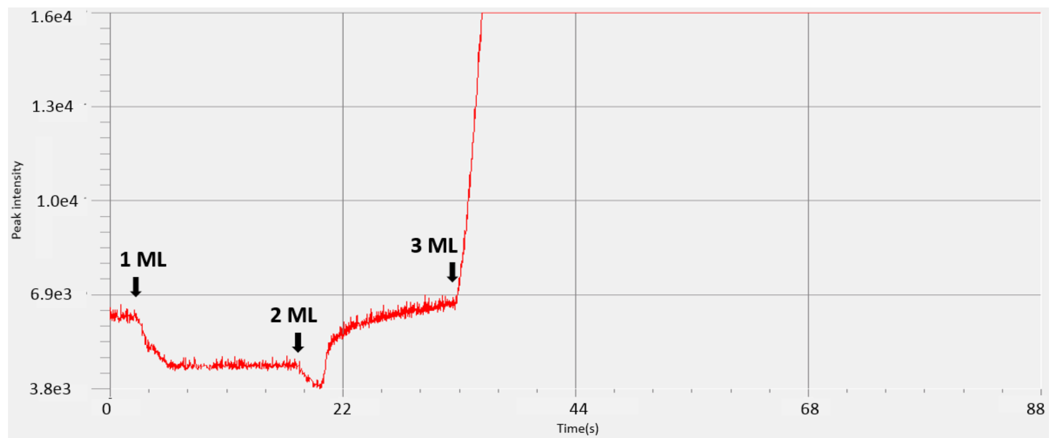


(c) $50°C$

Figure 4.18: RHEED intensity profile of the considered scanning region.

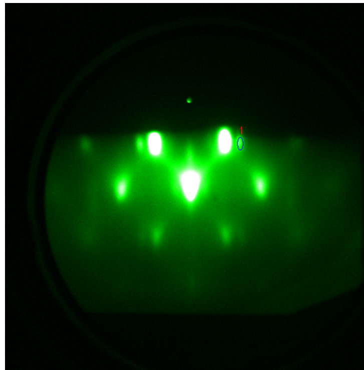

(a) Scanning region

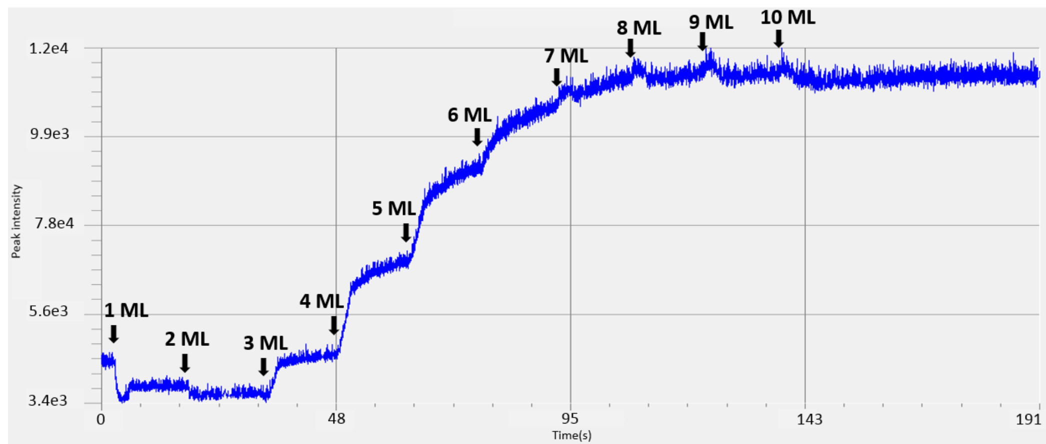


(b) −7°C

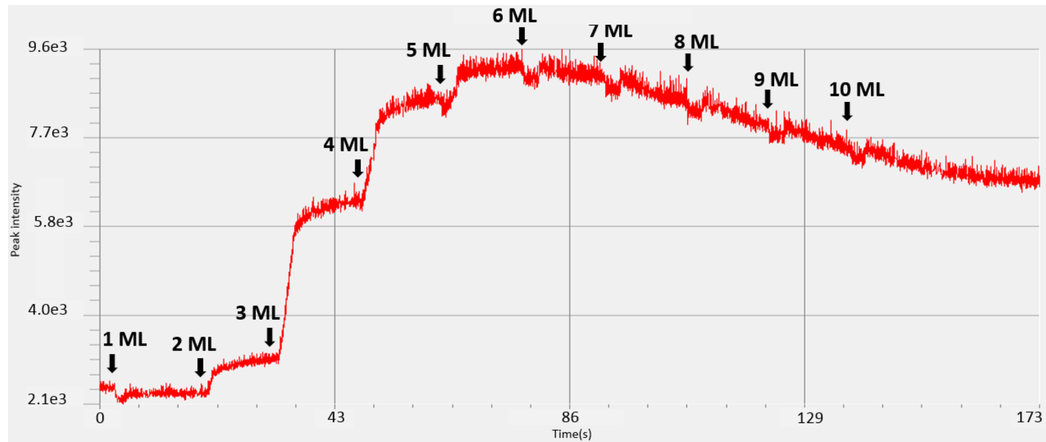


(c) 50°C

Figure 4.19: RHEED intensity profile of the considered scanning region.

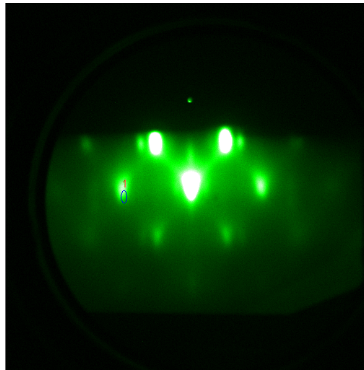

(a) Scanning region

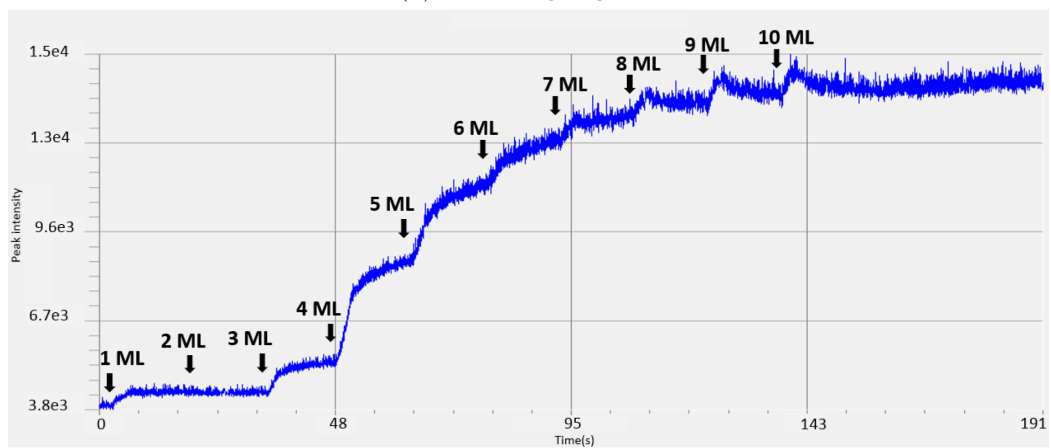


(b) −7°C

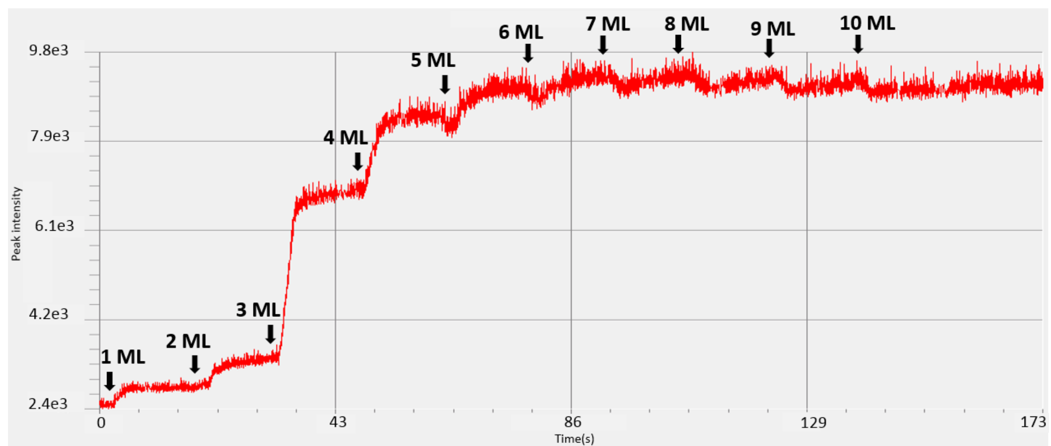


(c) 50°C

Figure 4.20: RHEED intensity profile of the considered scanning region.

The XRD analysis revealed that the grown material was a single crystal with scan results identical to the samples grown at low temperature. The surface did not appear particularly rougher from visual and Nomarski inspection, however it displayed a slightly higher level of defects (see Figure 4.21). Due to limited access to the instrument, no AFM investigation was realized, however it would be interesting to see how the roughness varied on a smaller scale in comparison with the low temperature growths. This is valuable information from the MBE point of view since the use of a higher growth temperature would be more convenient for the grower. Notwithstanding, although the *Al* epilayers grown at this higher temperature proved to be single crystalline, a study of this samples by TEM would be necessary to characterize the interface sharpness and rule out interdiffusion effects upon growth. Formation of fuzzy, poorly defined interfaces between semiconductor and metal could hinder the resonators performance by creating TLS.

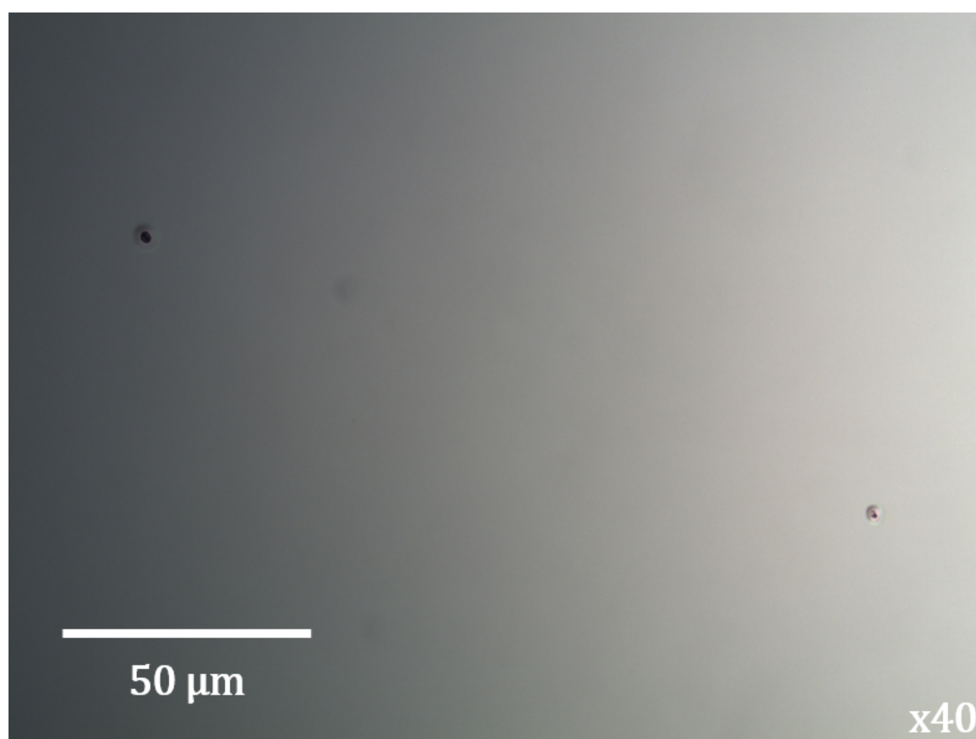


Figure 4.21: ×40 microscope observation of an $Al/GaAs$ sample grown at 50°C

## 4.3 $Al$ epitaxy on $Si$

Here are presented the results of the epitaxy of $Al$ on $Si$. Two different substrates were studied: $Si(111)$ and $Si(001)$. For $Si(111)$, both ("$1 \times 1$") and ($7 \times 7$) reconstructions were investigated. For $Si(001)$ only the most used $2 \times 1$ reconstruction was prepared.

### 4.3.1 $Al$ epitaxy on $Si(111) - (\text{“}1 \times 1\text{”})$

#### RHEED observations

Unlike for $Al$ epitaxy on $GaAs$, no transition from $2D$ to $3D$ was observed in the case of $Si(111)$ and the streaky pattern persisted throughout the growth (Figure 4.22), suggesting a layer-by-layer Frank-Van der Merwe growth mode. Upon opening of the $Al$ shutter, the RHEED lines corresponding to the $Si$ surface remained visible during the nucleation phase. After the first monolayer deposition, another set of lines appeared and remained with unchanged spacing until the end of the growth. With the deposition of the second monolayer, the lines attributed to the underlying $Si$ started to faint until disappearing entirely. The RHEED streaks were observed 60° apart from each other, consistent with the formation of an $Al(111)$ phase. The fact that their spacing remained unchanged throughout the growth suggests that the $Al$ layers were relaxed from the very beginning. The RHEED images displayed on Figure 4.22 correspond to snapshots of the not triggered rotating wafer RHEED observations extracted from a movie taken at 30 frames per second. As such, because the frames were not taken at exact azimuths, they were not used to compute the interplanar distances from the RHEED streaks spacing.

#### XRD structural analysis

The sample was studied with the Bruker D8 ADVANCE systems. High resolution XRD analysis was not used since a preliminary test determined that the reflected intensity was too small, likely due to the roughness of the unreconstructed $Si(111) - (\text{“}1 \times 1\text{”})$ surface. First, a coupled $2\theta$-$\omega$ scan was performed, which is presented on Figure 4.23a. The peak

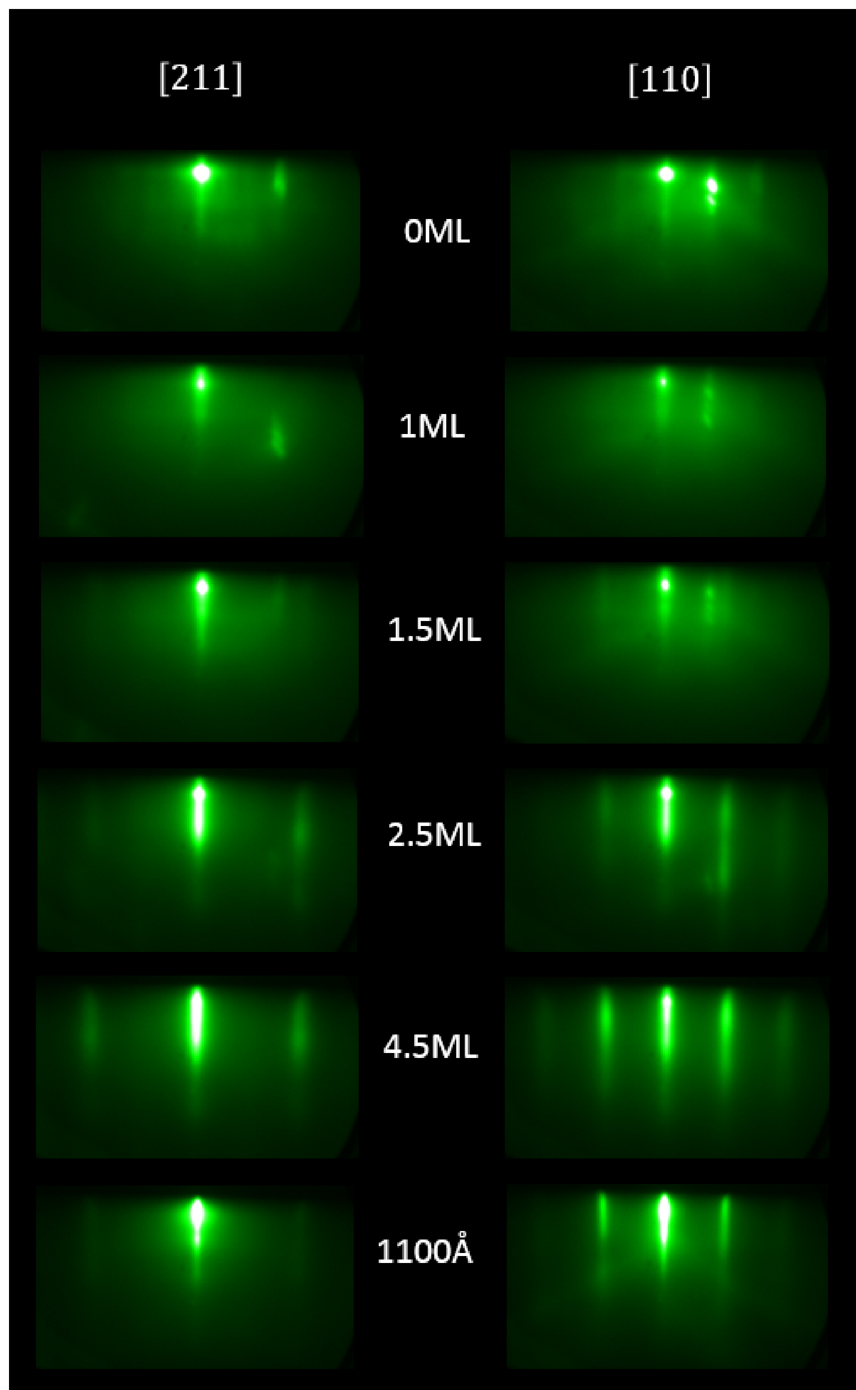


Figure 4.22: RHEED observations of the $Al$ epitaxy on a $Si(111)-(``1\times1")$ substrate in the $[211]Si$ direction (left) and in the $[110]Si$ direction (right).

at $2\theta = 38.429°$ was ascribed to $Al(111)$. No other peak was observed, except the $Si(111)$ substrate peak at $2\theta = 28.44°$ and its satellite peaks (too narrow to come from the grown phase and appearing on other XRD scans with different materials grown on $Si$ substrates). No increased signal was observed at the expected $Al(220)$ and $Al(220)$ positions. The calculated lattice constant of the $Al$ film was 4.0540Åfrom the $Al(111)$ peak, while the bulk value is 4.0495Å. The layers are therefore fully relaxed.

The sample was then tilted by 54.73° ($\Psi$ axis) to perform a $\Phi$ scan. While the coupled scan only displayed one peak for $Al(111)$, the phase could have crystallized in two equivalent orientations and lead to the formation of bicrystals. The $\Phi$ scan is presented on Figure 4.23b. Only 3 peaks, 120° from each other, were observed. This validates the single crystalline nature of the grown layers.

Rocking curves (see Figure 4.24) were also obtained for $Al(111)$ (at $\psi = 0$ and $2\theta = 38.42$) and $Al(200)$ (at $\psi = 54.74$ and $2\theta = 44.74$). The $Al(111)$ peak appeared almost 10 times as sharp as the $Al(200)$ peak with $FWHM(111) = 0.15°$ while $FWHM(200) = 1.15°$, with a substrate $FWHM$ of 0.03°. This might indicate a slight tilt of the (200) planes inducing stress and dislocations. The lattice parameter computed from the angular peak position of the $Al(200)$ peak ($2\theta = 44.738°$) amounts to 4.0481Åcompared to the bulk value of 4.0495Å. Once again, the layers are therefore fully relaxed.

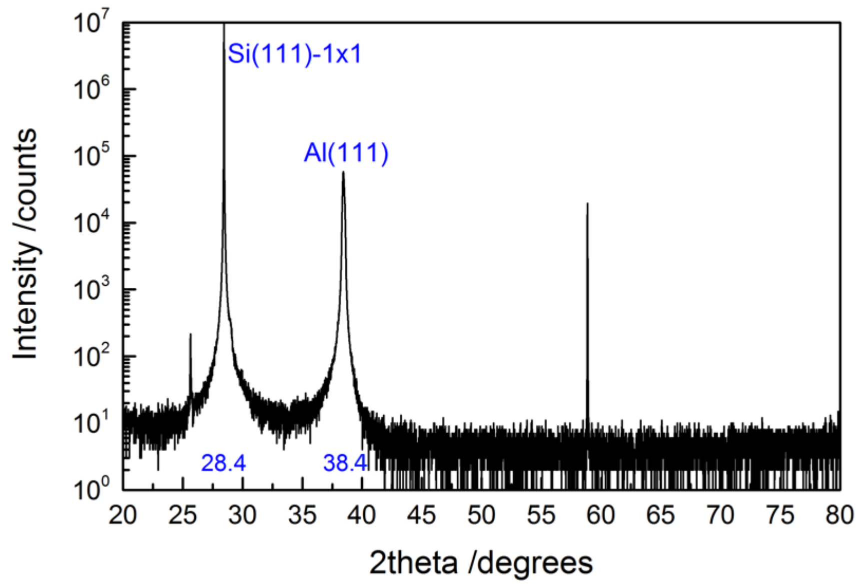


(a) Coupled scan at $\Psi = 0°$

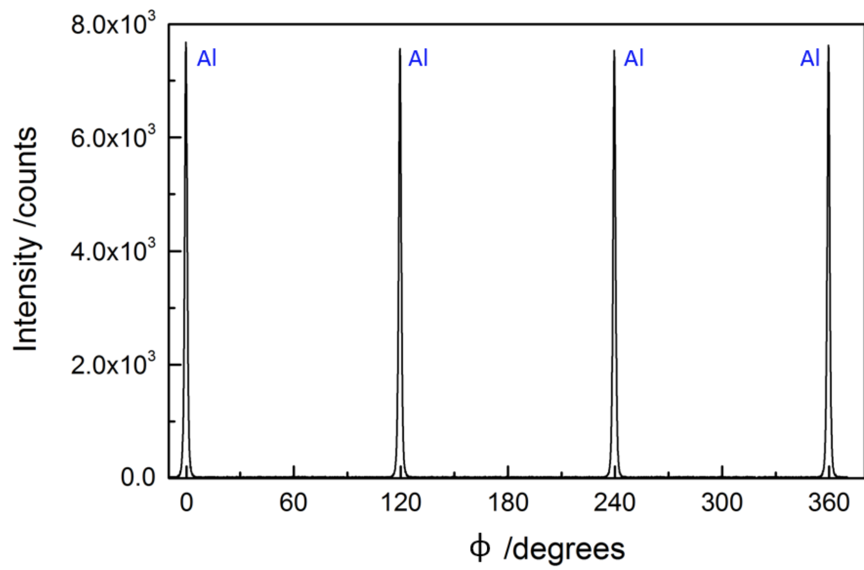


(b) $\Phi$ scan at $\Psi = 54.73°$

Figure 4.23: Measured XRD results for $Al/Si(111) - (\text{“}1 \times 1\text{”})$ epitaxy.

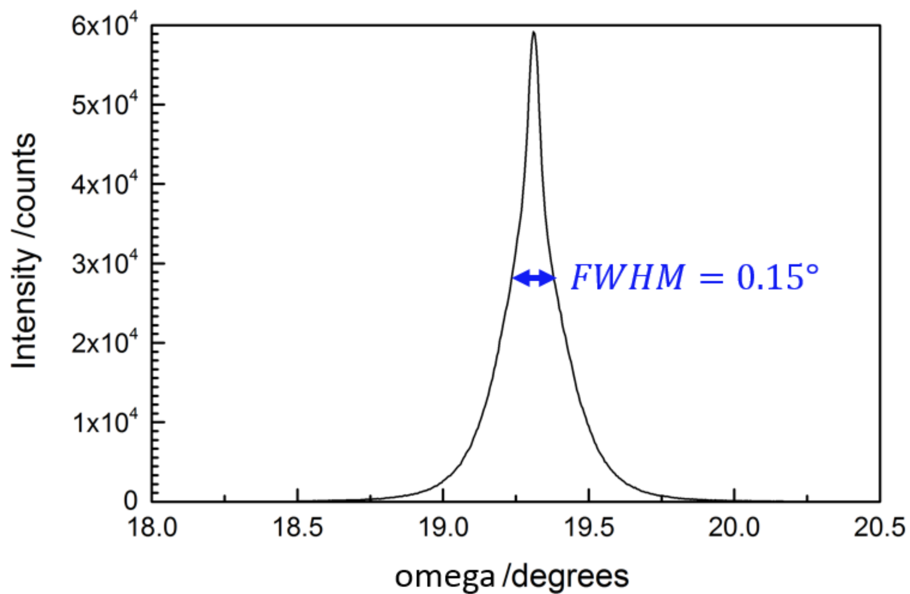


(a) Rocking curve of $Al(111)$

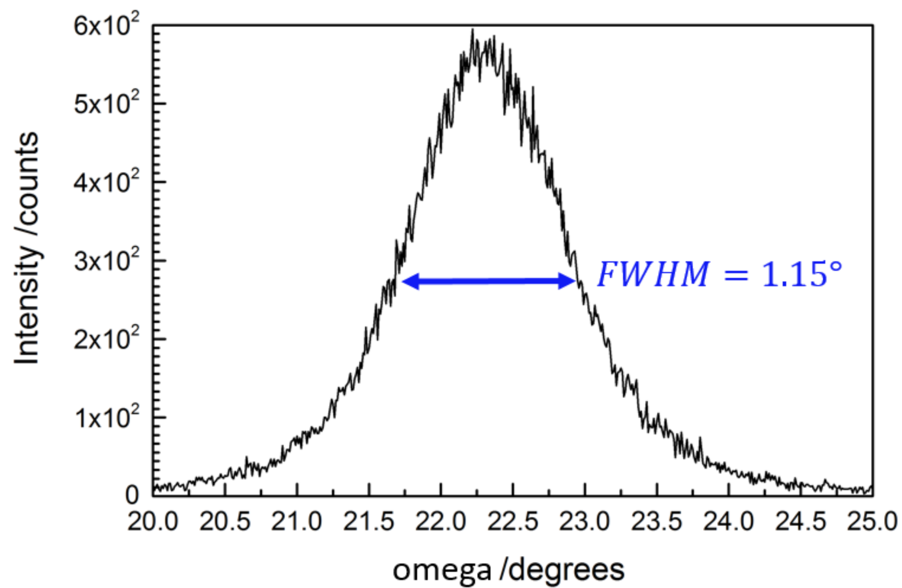


(b) Rocking curve of $Al(200)$

Figure 4.24: Measured rocking curves for $Al/Si(111) - (\text{“}1 \times 1\text{”})$ epitaxy.

### Morphological study

The observed surface with the Nomarski microscope was smooth and featureless with very low point defect density, remarkably similar to the $Al$ layers grown on $GaAs$ substrates.

A $1 \times 1\mu$m AFM scan and a line section are presented in Figure 4.25. The estimated RMS roughness over a $1\mu\text{m}^2$ area was 0.487nm which is very similar to what was found for epitaxy on $GaAs$. This roughness is once again equivalent to the one of the best samples obtained by Megrant *et al* [4] in the patterning of superconducting resonators on Sapphire (0.4nm).

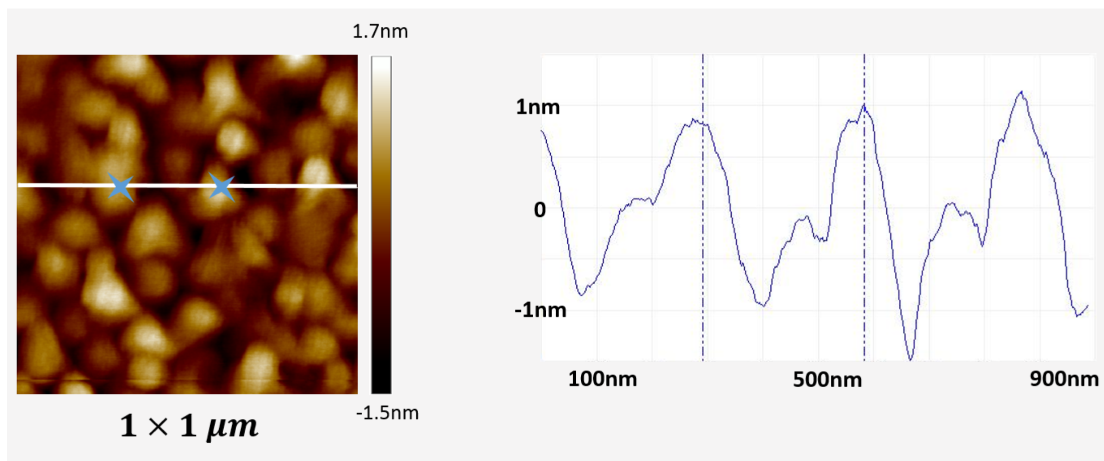


Figure 4.25: $1 \times 1\mu m$ AFM scan of an $Al/Si(111) - (\text{“}1 \times 1\text{”})$ sample and the associated line section. The depth profile on the right corresponds to the white line on the left scan and markers on this line are represented by dotted lines on the depth profile.

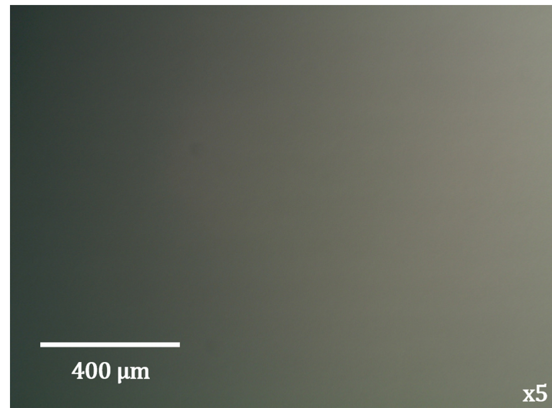


(a) $\times 5$ magnification

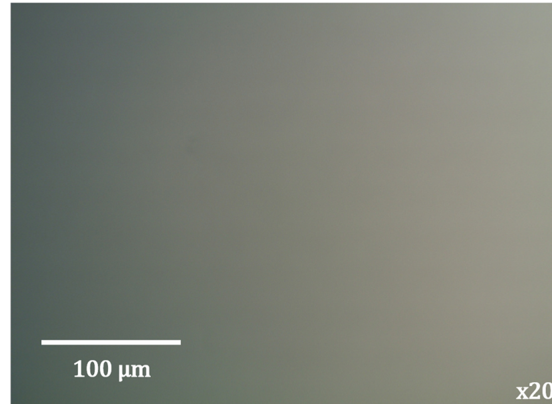


(b) $\times 20$ magnification

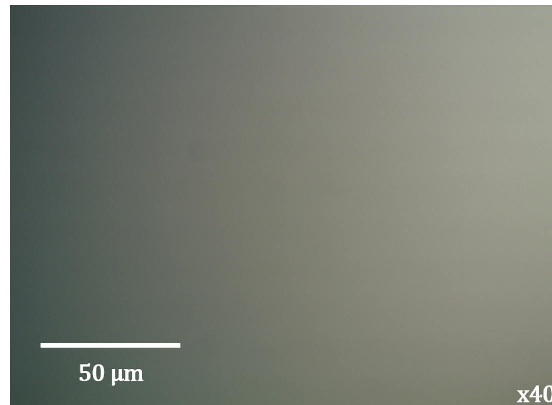


(c) $\times 40$ magnification

Figure 4.26: Nomarski micrographies for $Al/Si(111) - (\text{“}1 \times 1\text{”})$.

### 4.3.2 $Al$ epitaxy on $Si(111) - (7 \times 7)$

#### RHEED observations

The RHEED observations of $Al$ epitaxy on $7 \times 7$" reconstructed surface are very similar to the "$1 \times 1$" case as can be seen on Figure 4.27. Upon opening of the shutter, the RHEED pattern gradually transformed to the unreconstructed $Si$ diffraction pattern, indicating the good registry of the $Al$ overlayer with the substrate, matching 4 $Al$ atoms to 3 $Si$ atoms as described in Chapter 2. After 1ML, the lines started to faint until disappearing totally after 2ML. Meanwhile, two other sets of lines appeared from 1.5ML. In the [110] direction, these two sets of lines can clearly be seen on the RHEED image in Figure 4.27. The lattice parameters computed from the distance between the streaks were 4.3Åand 4.8Å(Table 4.3).

Table 4.3: Lattice parameters computed from RHEED observations. The 0° azimuth corresponds to the RHEED [211] direction.

| Thickness | Azimuth (°) | Reciprocal spacing (pixels) | Computed real spacing (Å) | Computed lattice parameter (Å) | Expected lattice parameter (Å) |
|---|---|---|---|---|---|
| 0ML | 0 | 31.2 | 22.0 | 6.3 | 6.3 ($Si(111)$) |
| 1ML | 0 | 210.8 | 3.2 | 6.5 | 6.3 ($Si(111)$) |
| 2ML | 0 | 160.4 | 4.3 | 4.3 | 4.1 ($Al(100)$) |
| | 0 | 283.4 | 2.4 | 4.8 | 4.7 ($Al(111)$) |
| 1100$\AA$ | 0 | 282.6 | 2.4 | 4.8 | 4.7 ($Al(111)$) |

Taking into account the error margin (±0.3Å), these values are respectively close to the expected lattice parameter of $Al(100)$ (4.1Å) and $Al(111)$ (4.7Å) which seems to indicate that both orientations were initially present. One of these sets of lines fainted gradually until disappearing after about 15ML and only the ones corresponding to a lattice parameter of 4.8Å remained until the end of the growth. It therefore seems that this growth also follows a Frank-Van-der-Merwe mode, as was the case for ("$1 \times 1$") but unlike the other substrates studied in this project. Similar streaks were observed at azimuths 60°, 120°, 180°, 240° and 300° away from the [211] RHEED direction, suggesting the formation of an $Al(111)$ phase. The fact that the spacing of the $Al$ streaks did not change from

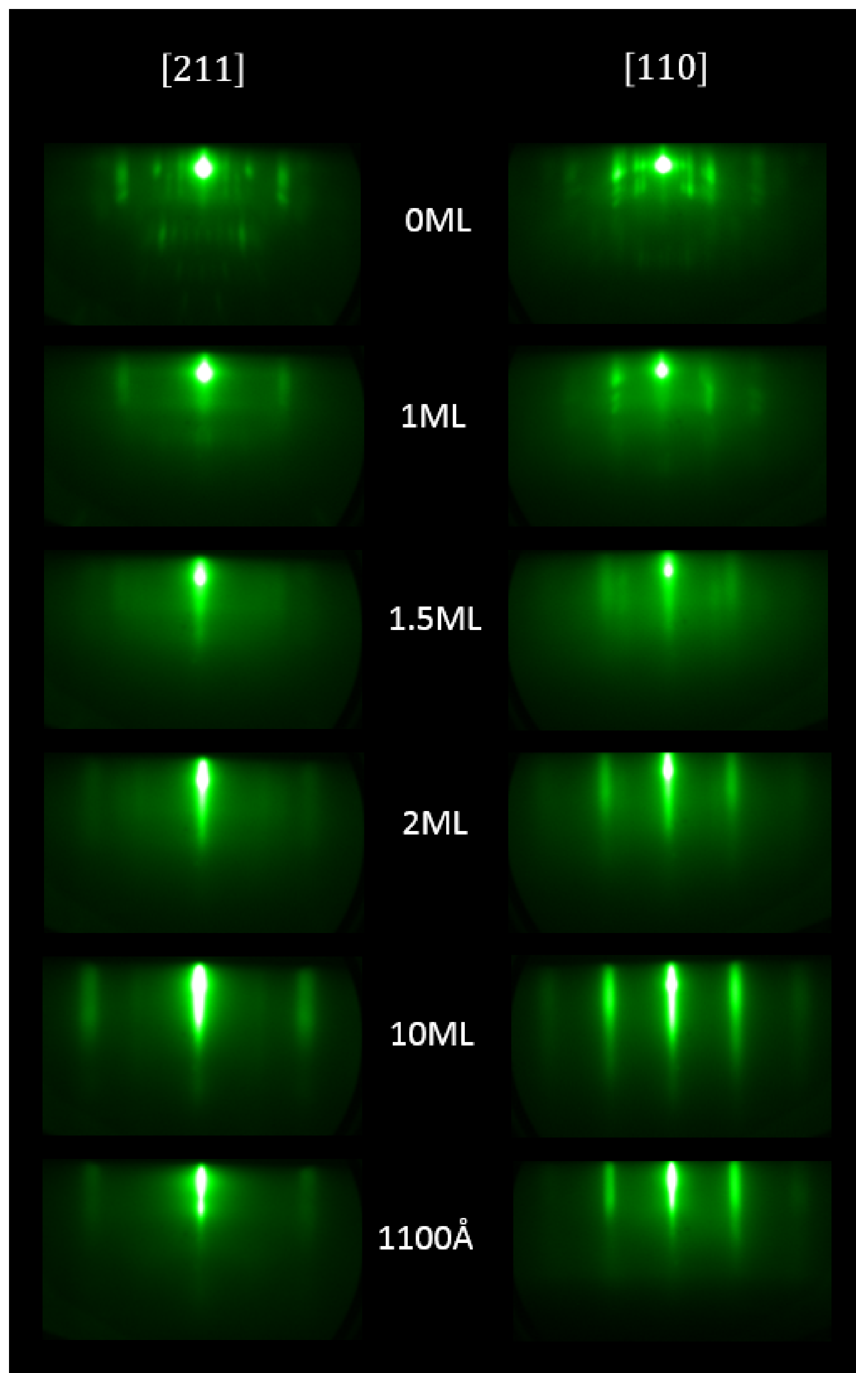


Figure 4.27: RHEED observations of the $Al$ epitaxy on a $Si(111) - 7 \times 7$ substrate in the $[211]Si$ direction (left) and in the $[110]Si$ direction (right).

the nucleation throughout the growth indicates that the $Al$ layers were relaxed from the beginning, as in the case of ("$1 \times 1$").

### HRXRD structural analysis

Only rocking curves were obtained for this sample (Figure 4.28) with the $QC3$ system. The $FWHM$ of the $Al(111)$ peak was estimated to $0.288°$ while the substrate's peak $FWHM$ was $0.017°$. These values are comparable to the ones obtained for the ("$1 \times 1$") substrate. The peak position of the rocking curve at $\omega = 19.1380°$ led to a calculated lattice parameter of $a = 4.0696$Å. This is close to what was found with the $Si(111) - $("$1 \times 1$") substrate ($a = 4.0540$Å) and to the bulk value of $Al$ : $a = 4.0495$Å. These layers are also relaxed.

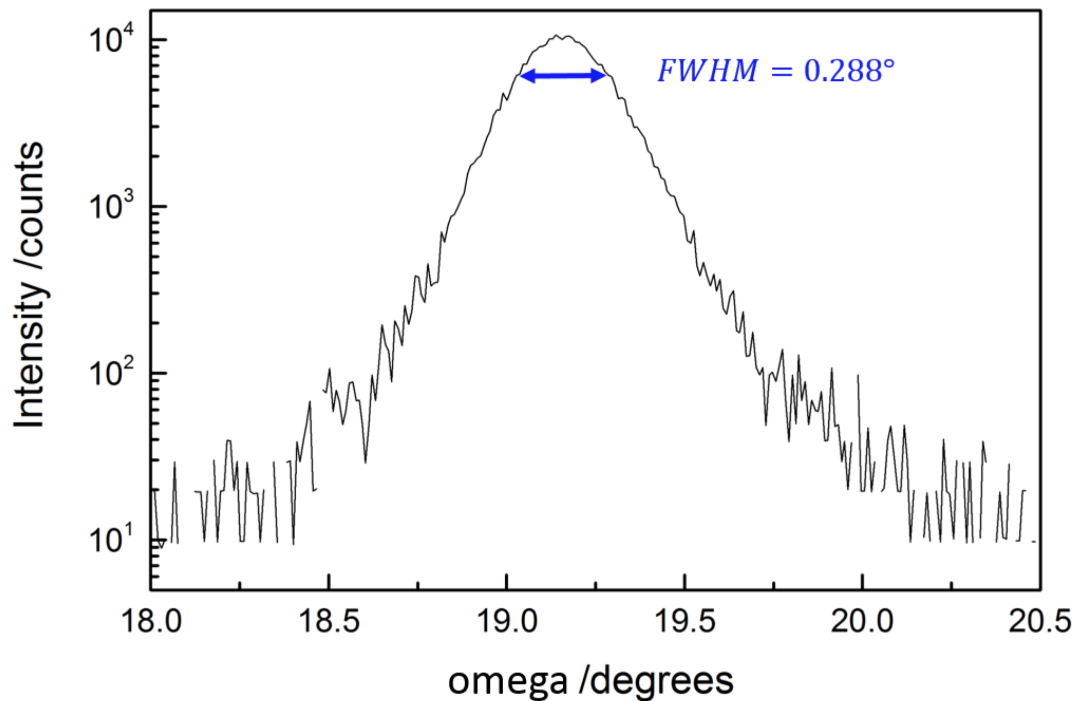


Figure 4.28: Measured XRD results for $Al/Si(111) - (7 \times 7)$ epitaxy: rocking curve of $Al(111)$.

### Morphological study

The layer grown on the $(7 \times 7)$ reconstructed $Si$ substrate was expected to be smoother since this starting surface is more stable and regular than the ("$1 \times 1$") counterpart. A $1 \times 1\mu$m AFM scan and a line section are presented in Figure 4.29. The estimated RMS roughness over a $1\mu\text{m}^2$ area was 0.519nm which is again close to what was found for $GaAs$ and the ("$1 \times 1$") reconstructed $Si(111)$ but not significantly better.

Under the Nomarski, the samples appeared to be rougher than any of the previously studied as can be seen on the micrographies depicted in Figure 4.30. However, this roughness is not related to the epitaxy but the surface preparation (most likely due to formation of pits on the surface during the oxide desorption). The overall point defect density throughout the layer was very comparable to that obtained for the growths on $Si(111)-$("$1 \times 1$") and on $GaAs$.

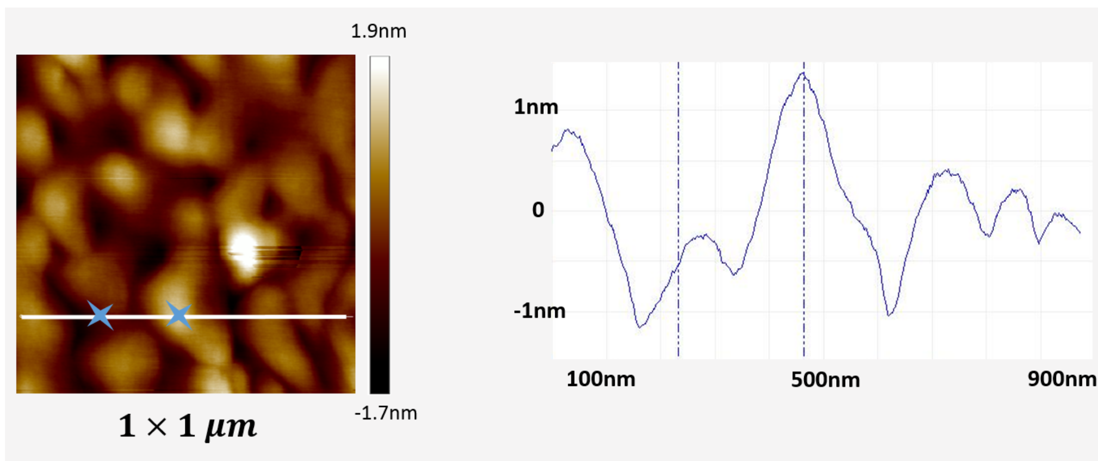


Figure 4.29: $1 \times 1 \mu m$ AFM scan of an $Al/Si(111)-(7 \times 7)$ sample and the associated line section. The depth profile on the right corresponds to the white line on the left scan and markers on this line are represented by dotted lines on the depth profile.

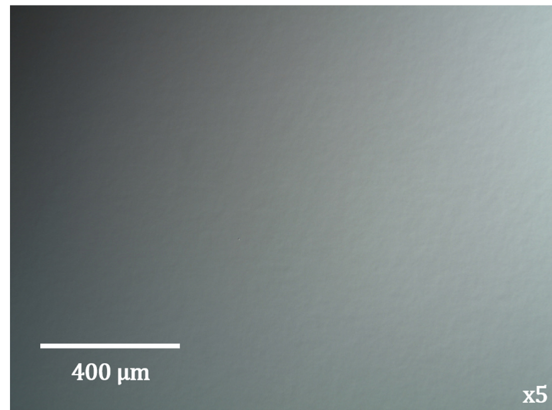


(a) ×5 magnification

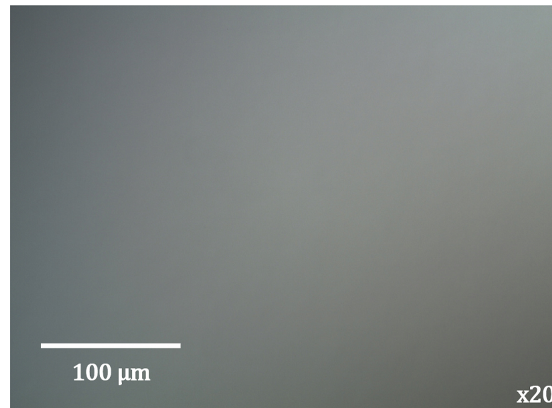


(b) ×20 magnification

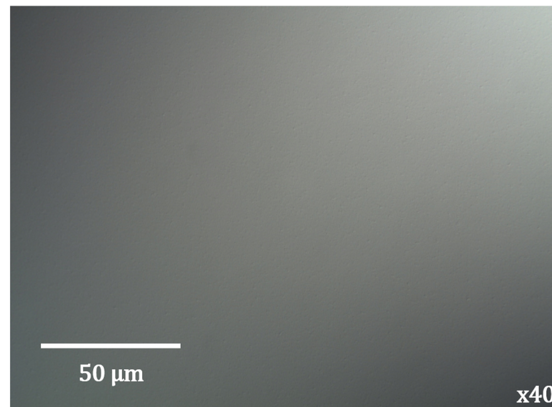


(c) ×40 magnification

Figure 4.30: Nomarski observations for $Al/Si(111) - (7 \times 7)$.

### 4.3.3 $Al$ epitaxy on $Si(001)-(2\times 1)$

#### RHEED observations

The RHEED observations for the $Al$ growth on $Si(001)$ substrates were very different from these grown on $Si(111)$ as can be seen on Figure 4.31. Upon opening of the shutter, the $Si$ RHEED streaks transformed to the unreconstructed $Si(001)$ pattern with a lattice parameter computed from the streaks spacing of 5.4Å(Table reftab:rheedspacingsi100). The streaks fainted right away until disappearing completely after 2ML. The fact that only fainting streaks were observed during the first 2ML deposition indicates the formation of disordered layers. With the third monolayer deposition, features indicative of $3D$ islands formation appeared and increased in intensity during the first 10ML deposition. This seems to correspond to a Volmer-Weber growth mode, rather than a Stranski-Krastanov as was observed for the epitaxy of $Al$ on $GaAs$ (no ordered wetting layer). The $3D$ pattern remained unchanged until the end of the growth in the [100] direction. On the other hand, in the orthogonal [110] direction, the pattern smoothed gradually although it did not achieve sharp streaks by the end of the growth. Two sets of lines were observed in the [110] direction. The calculated lattice parameters were 5.5Åand 3.8Å. This is consistent with the coexistence of two equivalent orientations of $Al(110)$: 5.7Åis the interplanar spacing of the $Al(110)$ planes along the [001] direction and 4.0Åis the interplanar spacing of the $Al(110)$ planes along the $[\bar{1}10]$ direction. Similar streaks were observed in the azimuths 90°, 180° and 270° away from the [110] RHEED direction. These observations are consistent with the literature reviewed in Chapter 2.

#### HRXRD structural analysis

The XRD analysis (see Figure 4.32) revealed the existence of an $Al(220)$ peak of low relative intensity. No other peaks were observed. This suggests that only (110) crystals grew on the surface but the low intensity of the peak and its width compared to the substrate peak indicates the presence of concurrent equivalent orientations, as was observed with the RHEED pattern analysis.

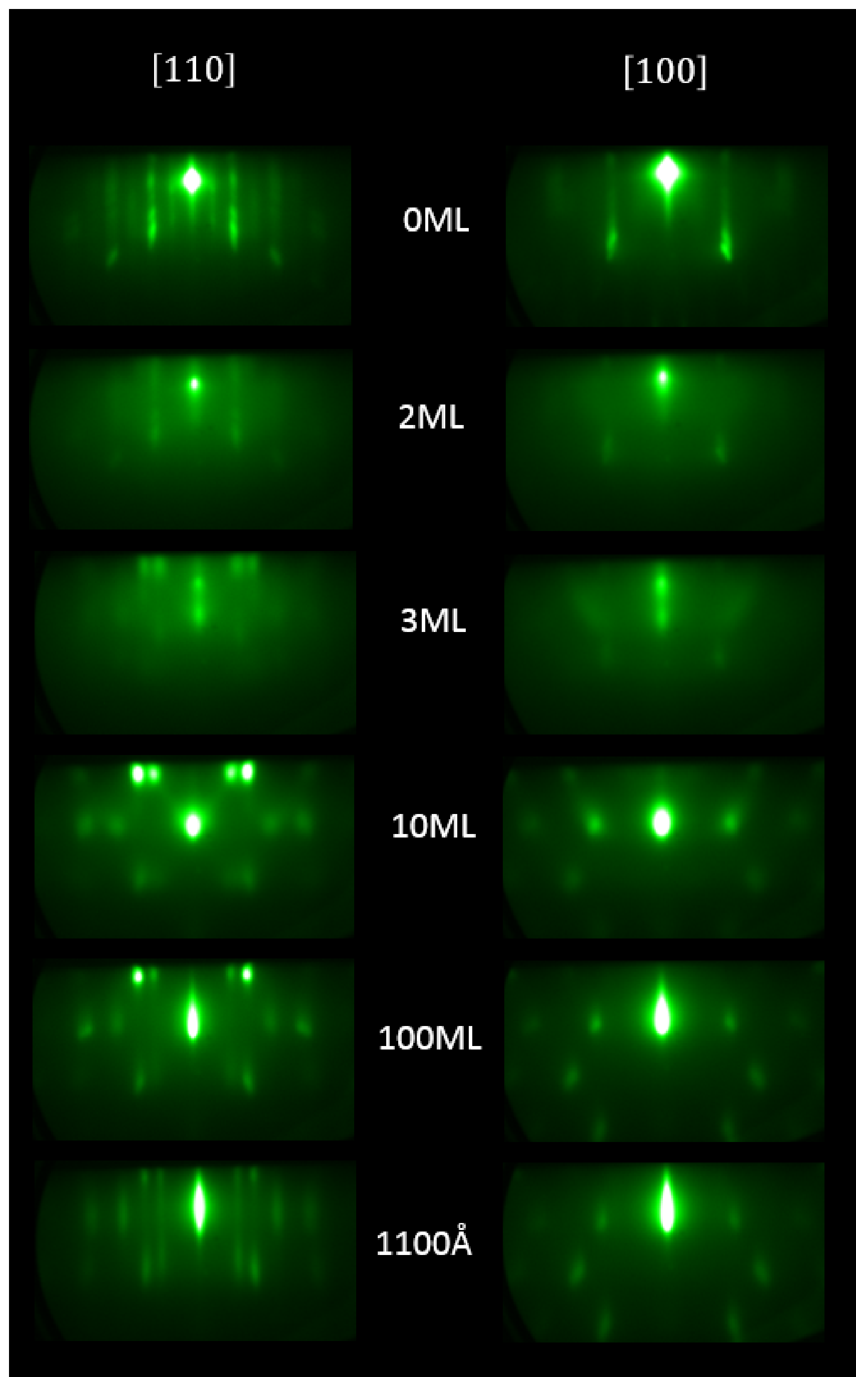


Figure 4.31: RHEED observations of the $Al$ epitaxy on a $Si(001)-(2\times1)$ substrate in the $[110]Si$ direction (left) and in the $[100]Si$ direction (right).

Table 4.4: Lattice parameters computed from RHEED observations. The 0° azimuth corresponds to the RHEED [110] direction.

| Thickness | Azimuth (°) | Reciprocal spacing (pixels) | Computed real spacing (Å) | Computed lattice parameter (Å) | Expected lattice parameter (Å) |
|---|---|---|---|---|---|
| 0ML | 0 | 50.3 | 10.9 | 5.4 | 5.4 ($Si$(001)) |
| 1ML | 0 | 101.9 | 5.4 | 5.4 | 5.4 ($Si$(001)) |
| 1100Å | 0 | 100.3 | 5.5 | 5.5 | 5.7 ($Al$(110) along the [$\bar{1}$10] direction) |
| | 0 | 142.0 | 3.8 | 3.8 | 4.1 ($Al$(110) along the [001] direction) |

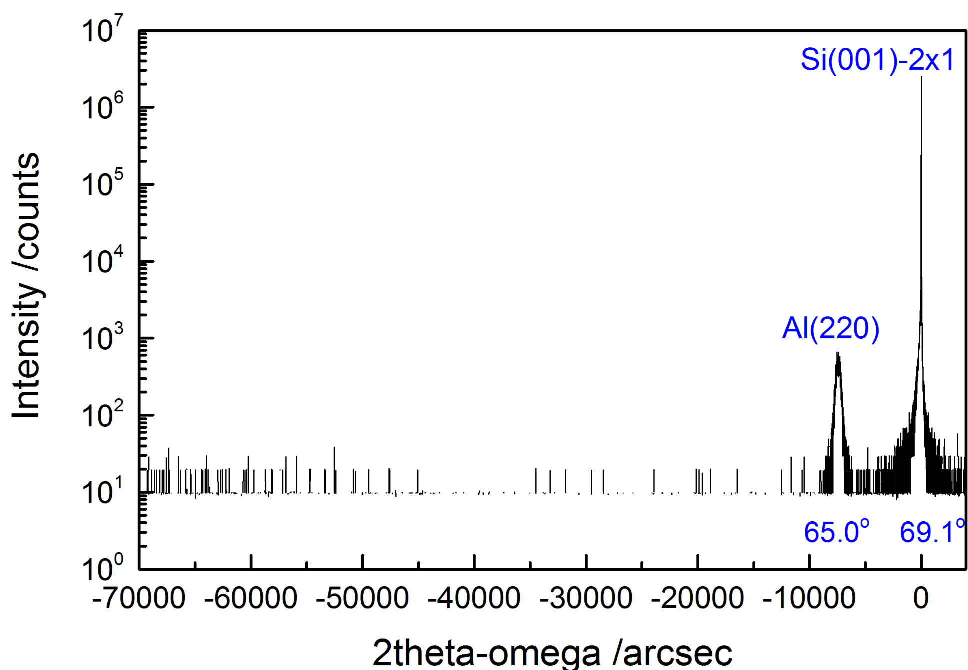


Figure 4.32: Measured XRD results for $Al/Si(001) - 2 \times 1$ epitaxy: Coupled scan of the sample.

### Morphological study

A $1 \times 1\mu$m AFM scan and a line section are presented in Figure 4.33. The estimated RMS roughness over a $5\mu\text{m}^2$ area was 1.10nm and 0.719nm over a $1\mu m$ area. These findings corroborate the RHEED spotty patterns, confirming that the $Si(001)$ substrates yield rougher films.

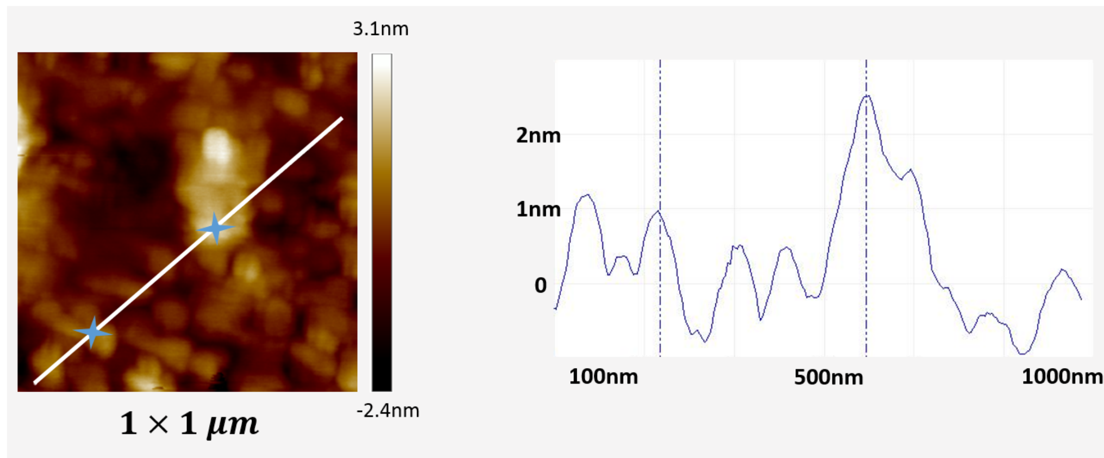


Figure 4.33: $1 \times 1\mu m$ AFM scan of an $Al/Si(001) - (2 \times 1)$ sample and the associated line section. The depth profile on the right corresponds to the white line on the left scan and markers on this line are represented by dotted lines on the depth profile.

This sample was the roughest observed with the Nomarski microscope, as can be seen on Figure 4.34. Once again this roughness might be related to the formation of pits on the substrate's surface during the oxide desorption.

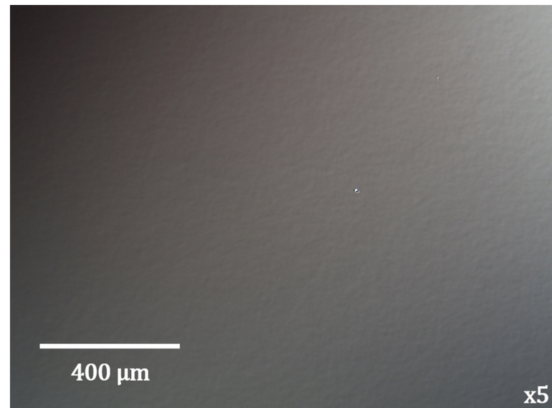

(a) ×5 magnification

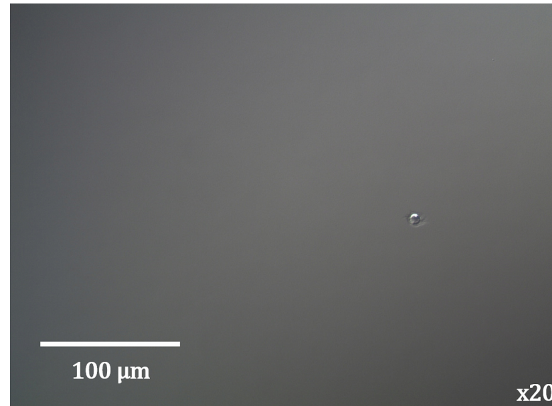

(b) ×20 magnification

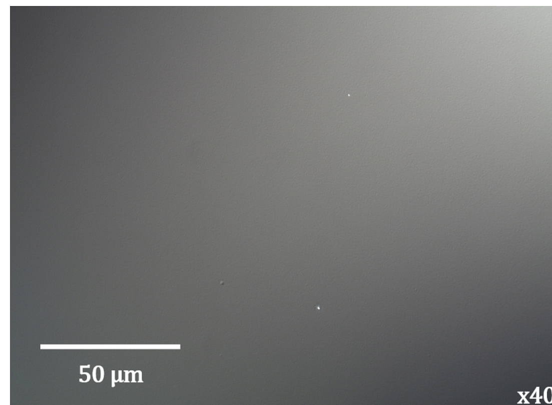

(c) ×40 magnification

Figure 4.34: Nomarski observations for $Al/Si(001)-(2\times 1)$.

### 4.3.4 Growth at higher temperature

A higher growth temperature, namely 100°C, was investigated on a $Si(001)$ substrate. The obtained surface noticeably rough on all Nomarski magnifications (Figure 4.35). The grown layer is believed to be amorphous since no other peak than the $Si$ substrate's one was found by the XRD. This validates the choice of low temperature epitaxy in order to yield single crystalline and flat materials.

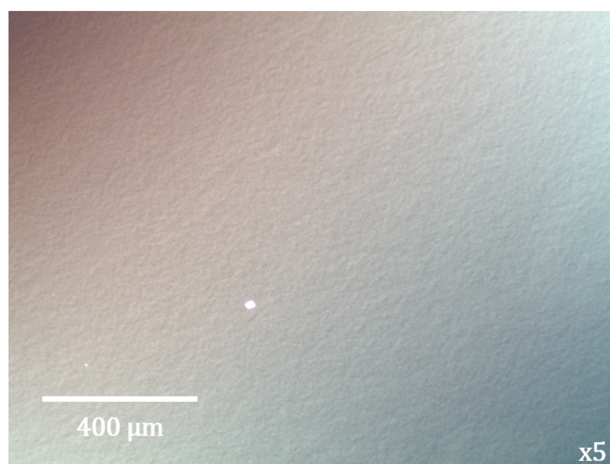


(a) ×5 magnification

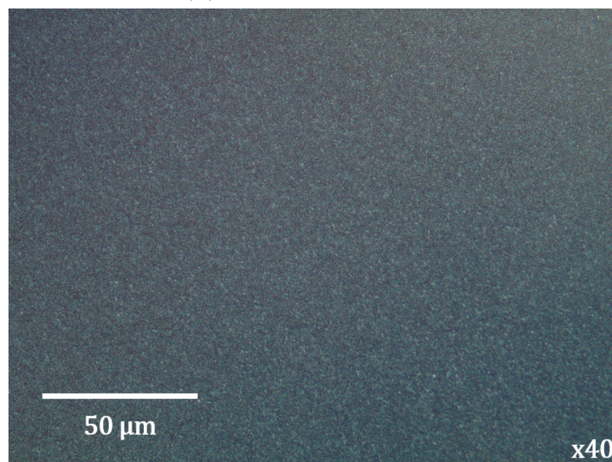


(b) ×40 magnification

Figure 4.35: Nomarski microscope observation of an $Al/Si$ sample grown at 100°C.

# Chapter 5

# Conclusion

## 5.1 Summary of findings

This project aimed at improving the three pivotal steps of superconducting resonators conception: selecting the best substrate, setting up the optimal preparation process of the materials and optimizing the growth conditions of $Al$ layers to obtain possibly low level of defects. By investigating different starting surface reconstructions for $GaAs$ and $Si$, it was shown that MBE growth of $Al$ layers at $-10°C$ on a $GaAs(001)-(2\times4)$ reconstructed surface gave the best results.

- Epitaxy on $GaAs(001)-(2\times4)$ substrates consistently led to single crystalline layers of $Al(110)$. A detailed *in-situ* RHEED study showed that the growth followed a Stranski-Krastanov mode by forming an ordered $(1\times4)$ wetting layer that broke the $As$ dimers of the reconstructed $GaAs$ surface. This was followed by the nucleation of elongated $3D$ islands which subsequently coalesced showing evidence of a higher mobility of the $Al$ atoms along the initial rows of $As$ dimers. These growth processes gave way to the final smooth surface with elongated features in the $[\bar{1}10]$ direction and RMS roughness 0.552nm.

- Epitaxy on $GaAs(001)-(4\times4)$ substrates produced inconsistent results with poly-crystalline layers of $Al(100)$, $Al(110)$ and $Al(111)$. While the level of point defects

was similar to the samples grown on $GaAs(001) - (2 \times 4)$, the estimated RMS roughness was higher (1.20nm).

- Epitaxy on $Si(111) - (``1 \times 1")$ substrates led to single-crystalline layers of $Al(111)$ with a Frank-Van-der-Merwe growth mode. A possible slight tilt of the $Al(200)$ planes which could induce strain and defects remains however to be further investigated by XRD analysis. This sample had a very smooth surface of RMS roughness of 0.487nm.

- Epitaxy on $Si(111) - (7 \times 7)$ substrates yielded single-crystalline layers of $Al(111)$ similar to the ones grown on $Si(111) - (``1 \times 1")$. The growth mode was also Frank-Van-der-Merwe. A detailed XRD study remains to be accomplished to confirm the single crystalline nature and, again, to investigate a possible tilt of the $Al(200)$ crystal planes. While the RMS roughness was very similar to the previously studied layers (0.519nm), this sample displayed some roughness under the Nomarski microscope, likely due to the formation of pits during the high temperature surface preparation. The $(7 \times 7)$ reconstruction indeed required a very slow cooling procedure which maintained the $Si$ wafer at elevated temperature for a longer time.

- Epitaxy on $Si(001) - (2 \times 1)$ substrates yielded bicrystals of $Al(110)$, as was demonstrated by the RHEED analysis. These samples were the roughest among the $Si$ substrates with an estimated RMS roughness of 0.719nm. This sample also exhibited the roughness attributed to the formation of pits on the surface during oxide desorption.

The surface morphology of almost all samples was atomically smooth with a roughness comparable to the best samples obtained on Sapphire substrates by Megrant *et al* [4].

The establishment of the preparation procedure revealed that wet cleaning and subsequent transport to the system tended to incorporate more contaminants than it was removing. Thermal annealing and oxide desorption in the growth reactor proved to yield satisfactory growth output by themselves. In the case of $GaAs$ wafers, this thermal oxide removal was supplemented with the growth of a buffer structure to provide a clean and atomically smooth starting surface for epitaxy.

This project also endeavored to provide reproducible growth results by careful monitoring and controlling of the growth conditions. As such it was demonstrated that the suppression of possible sources of contamination during the substrate cooling period preceding epitaxy was crucial to the success of the growth. This meant in the experiments powering off the ion gauge, powering off the heated viewports and placing the main shutter in front of the substrate.

The final test of this optimizing process is the measurement of the performance of the resonators which are presently being fabricated.

## 5.2 Future directions of research

### 5.2.1 Resonators performance

At the time these words are written, the first resonators are being patterned and getting ready for measurements. Although we inferred from structural and topological results which substrate should be best, the performance of the resonators is here the critical judge. The cooling down process inside the measurement fridge will also modify the metal-substrate interface, due to the difference in thermal expansion coefficients. This is one more parameter that can only be assessed by the resonator's performance measurement.

### 5.2.2 Estimation of the sharpness of the interfaces

Interdiffusion of the substrate and epilayer materials is unwanted for the application of high quality factor superconducting resonators. Indeed, as was discussed in Chapter 2, interdiffusion could lead to the formation of crystal defects. Moreover, by introducing steps at the interface, it could cause the nucleation of different *Al* orientations (by adding strain in the direction normal to the surface). In order to minimize the TLS hence the losses in the resonators, the interfaces must be as sharp as possible. A variety of characterization techniques exist to assess this parameter, however not always suitable for a specific application. TEM in principle, can provide valuable insight on the sharpness of the interfaces

but the specimen preparation process and/or the electron beam can introduce artifacts, particularly for relatively soft materials as ultra-pure $Al$ is. An alternative for suitably equipped MBE systems could be *in-situ* AES or XPS which, even though the contaminants levels are expected to be well below the detection limit, could assess the amount of interdiffusion [30] and the formation of $AlAs$ [89].

### 5.2.3 Cleaning study

Thanks to the possibility of forming a clean and smooth $GaAs$ layer *in-situ*, surface cleaning prior to growth is not an important factor when using epi-ready $GaAs$ wafers as substrates for $Al$ resonators. However, this alternative is not available for $Si$ substrates in absence of suitable $Si$ source (high temperature effusion cell or e-beam evaporator). Preliminary results of a parallel study on the effect of the RCA surface cleaning, reported in Chapter 4, suggest that this method actually deteriorates the quality of epi-ready $Si$ wafers. Nevertheless, other methods of surface cleaning (e.g. UV/ozone cleaning, $HF$ dip, $H$ plasma, and combinations thereof) should be considered to this end. It seems that the method used by Madiomanana *et al* [47] consisting of cycles of HF dips and $O$-plasma treatments also reached excellent results and should be investigated. The $O$-plasma could be replaced by a UV/Ozone oven. Hence, a detailed study of the effect of $Si$ surface pre-cleaning on the quality of the $Si$ starting surface, the $Al$ epitaxy and, more importantly, the quality of the resonators is of paramount importance and should be conducted. This seems to be the next logical step in this project, having determined that $GaAs(001)$ and $Si(111)$ were suitable substrate choices.

# APPENDICES

# Appendix A

# MATLAB Calculator

This script computes the dimensions of microstrip resonators made on $Si$, $GaAs$ and Sapphire, targeting a characteristic impedance $Z_0 = 50\Omega$ and a resonant frequency $f_0 = 6GHz$. Microstrip resonators behave very similarly to CPW resonators and can be used as a first approximation for simulations. The considered substrate has a thickness of $500\mu m$ which corresponds to the wafers used in this project.

Listing A.1: MATLAB script for microstrip resonators made on $Si$, $GaAs$ and Sapphire.

```
clear all;

% ---------------------------------------------------------
% General declarations
% ---------------------------------------------------------

%Physical constants
mu0=1.256637061e-6;              %[N/A^2]
eps0=8.854187817e-12;            %[F/m]
c=299792458;                     %[m/s]

%Parameters
Z0=50;                           %[Ohm] - desired impedance
d=500e-6;                        %[m] - substrate's thickness
```

```
15 sigma_Al=1e30;                     %[S/m] - Aluminum conductivity ...
       (superconductor)
16
17 %Grids
18 f=4:0.1:10;                        %[GHz] - considered range of frequencies
19 f_res=6e9;                         %[Hz] - desired resonant frequency
20 omega=2*pi./(f.*10^9);             %[/s]
21
22 Rs=sqrt((omega.*mu0)./(2*sigma_Al));
23
24 % ----------------------------------------------------------
25 % Microstrip Al/Si
26 % ----------------------------------------------------------
27
28 %Material parameters
29 eps_r_Si=11.9;                     %[] - dielectric constant of Silicon
30 tan_Δ_Si=5e-6;                 %[] - loss tangent of Silicon
31
32 %First threshold frequency
33 ft1_Si=c/(2*pi*d)*sqrt(2/(eps_r_Si-1))*atan(eps_r_Si);      %[GHz]
34
35 %Resonator dimensions computing
36 A=Z0/60*sqrt((eps_r_Si+1)/2)+((eps_r_Si-1)/(eps_r_Si+1))*(0.23+0.11 ...
       /eps_r_Si);
37 B=377*pi/(2*Z0*sqrt(eps_r_Si));
38 temp=8*exp(A)/(exp(2*A)-2);      %[]
39 if temp>2
40     temp=2/pi*(B-1-log(2*B-1)+(eps_r_Si-1)/(2*eps_r_Si)*(log(B-1) ...
           +0.39-0.61/eps_r_Si));
41 end
42 W_Si=d*temp;                       %[m]
43
44 %Losses and quality factor
45 eps_e_Si=(eps_r_Si+1)/2+(eps_r_Si-1)/2*1/sqrt(1+12*d/W_Si);
46     %[] - effective permittivity
47 alpha_d_Si=f.*(10^9*2*pi/c*eps_r_Si*(eps_e_Si-1)*tan_Δ_Si ...
       /(2*sqrt(eps_e_Si)*(eps_r_Si-1)));
48     %[Np/m] - dielectric losses
```

```
49 alpha_d_Si_res=f_res*2*pi/c*eps_r_Si*(eps_e_Si-1)*tan_δ_Si ...
      /(2*sqrt(eps_e_Si)*(eps_r_Si-1));
50     %[Np/m] - dielectric losses at resonant frequency
51 alpha_c_Si=Rs./(Z0*W_Si);
52     %[Np/m] - conductor losses
53 alpha_c_Si_res=sqrt((2*pi/f_res*mu0)/(2*sigma_Al))/(Z0*W_Si);
54     %[Np/m] - conductor losses at resonant frequency
55 beta_Si=2*pi*f_res*sqrt(eps_e_Si)/c;
56     %[rad] - phase constant
57 Q_Si=beta_Si/(2*(alpha_d_Si_res+alpha_c_Si_res));
58     %[] - Quality factor
59
60 %Resonator length
61 l_Si=c/(2*f_res*sqrt(eps_e_Si)); %[m]
62
63 %Plots
64 plot(f,alpha_d_Si,'k-','linewidth',2); hold on;
65 set(gca,'fontsize',20);
66 xlabel('f(GHz)');
67 ylabel('losses(Np/m)');
68 title('Dielectric losses for Si, GaAs and Sapphire substrates');
69
70
71
72 % -------------------------------------------------------------
73 % Microstrip Al/GaAs
74 % -------------------------------------------------------------
75 %Material parameters
76 eps_r_GaAs=12.85;               %[] - dielectric constant of GaAs
77 tan_δ_GaAs=4e-4;            %[] - loss tangent of GaAs
78
79 %First threshold frequency
80 ft1_GaAs=c/(2*pi*d)*sqrt(2/(eps_r_GaAs-1))*atan(eps_r_GaAs);
81
82 %Resonator dimensions computing
83 A=Z0/60*sqrt((eps_r_GaAs+1)/2)+((eps_r_GaAs-1)/(eps_r_GaAs+1))*(0.23+0.11 ...
      /eps_r_GaAs);
84 B=377*pi/(2*Z0*sqrt(eps_r_GaAs));
```

```
85  temp=8*exp(A)/(exp(2*A)-2);      %[]
86  if temp>2
87      temp=2/pi*(B-1-log(2*B-1)+(eps_r_GaAs-1)/(2*eps_r_GaAs)*(log(B-1) ...
            +0.39-0.61/eps_r_GaAs));
88  end
89  W_GaAs=d*temp;                    %[m]
90
91  %Losses and quality factor
92  eps_e_GaAs=(eps_r_GaAs+1)/2+(eps_r_GaAs-1)/2*1/sqrt(1+12*d/W_GaAs);
93      %[] - effective permittivity
94  alpha_d_GaAs=f.*(10^9*2*pi/c*eps_r_GaAs*(eps_e_GaAs-1)*tan_Δ_GaAs ...
        /(2*sqrt(eps_e_GaAs)*(eps_r_GaAs-1)));
95      %[Np/m] - dielectric losses
96  alpha_d_GaAs_res=f_res*2*pi/c*eps_r_GaAs*(eps_e_GaAs-1)*tan_Δ_GaAs ...
        /(2*sqrt(eps_e_GaAs)*(eps_r_GaAs-1));
97      %[Np/m] - dielectric losses at resonant frequency
98  alpha_c_GaAs=Rs./(Z0*W_GaAs);
99      %[Np/m] - conductor losses
100 alpha_c_GaAs_res=sqrt((2*pi/f_res*mu0)/(2*sigma_Al))/(Z0*W_GaAs);
101     %[Np/m] - conductor losses at resonant frequency
102 beta_GaAs=2*pi*f_res*sqrt(eps_e_GaAs)/c;
103     %[rad] - phase constant
104 Q_GaAs=beta_GaAs/(2*(alpha_d_GaAs_res+alpha_c_GaAs_res));
105     %[] - Quality factor
106
107 %Resonator length
108 l_GaAs=c/(2*f_res*sqrt(eps_e_GaAs)); %[m]
109
110 %Plots
111 plot(f,alpha_d_GaAs,'b-','linewidth',2); hold on;
112
113
114
115 % ------------------------------------------------------------
116 % Microstrip Al/Sapphire
117 % ------------------------------------------------------------
118 %Material parameters
119 eps_r_Sa=11.1;                     %[] - dielectric constant of Sapphire
```

```
120 tan_Δ_Sa=1e-5;                  %[] - loss tangent of Sapphire
121
122 %First threshold
123 ft1_Sa=c/(2*pi*d)*sqrt(2/(eps_r_Sa-1))*atan(eps_r_Sa);
124 A=Z0/60*sqrt((eps_r_Sa+1)/2)+((eps_r_Sa-1)/(eps_r_Sa+1))*(0.23+0.11 ...
       /eps_r_Sa);
125 B=377*pi/(2*Z0*sqrt(eps_r_Sa));
126
127 %Variables
128 temp=8*exp(A)/(exp(2*A)-2);      %[]
129 if temp>2
130     temp=2/pi*(B-1-log(2*B-1)+(eps_r_Sa-1)/(2*eps_r_Sa)*(log(B-1) ...
           +0.39-0.61/eps_r_Sa));
131 end
132 W_Sa=d*temp;                        %[m]
133
134 %Losses and quality factor
135 eps_e_Sa=(eps_r_Sa+1)/2+(eps_r_Sa-1)/2*1/sqrt(1+12*d/W_Sa);
136     %[] - effective permittivity
137 alpha_d_Sa=f.*(10^9*2*pi/c*eps_r_Sa*(eps_e_Sa-1)*tan_Δ_Sa ...
       /(2*sqrt(eps_e_Sa)*(eps_r_Sa-1)));
138     %[Np/m] - dielectric losses at
139 alpha_d_Sa_res=f_res*2*pi/c*eps_r_Sa*(eps_e_Sa-1)*tan_Δ_Sa ...
       /(2*sqrt(eps_e_Sa)*(eps_r_Sa-1));
140     %[Np/m] - dielectric losses at resonant frequency
141 alpha_c_Sa=Rs./(Z0*W_Sa);
142     %[Np/m] - conductor losses
143 alpha_c_Sa_res=sqrt((2*pi/f_res*mu0)/(2*sigma_Al))/(Z0*W_Sa);
144     %[Np/m] - conductor losses at resonant frequency
145 beta_Sa=2*pi*f_res*sqrt(eps_e_Sa)/c;
146     %[rad] - phase constant
147 Q_Sa=beta_Sa/(2*(alpha_d_Sa_res+alpha_c_Sa_res));
148     %[] - Quality factor
149
150 %Resonator length
151 l_Sa=c/(2*f_res*sqrt(eps_e_Sa));    %[m]
152
153 %Plots
```

```
154 plot(f,alpha_d_Sa,'y-','linewidth',2); hold on;
155 legend('alpha_d for Si', 'alpha_d for GaAs', 'alpha_d for Sapphire');
```

# Appendix B

# Miller indices and reciprocal space

In a crystal, the smallest unit cell which can be translated to form the whole lattice is called the primitive cell. Basis vectors of this unit cell are called the basis vectors of the crystal, labeled here $\mathbf{a_1}$, $\mathbf{a_2}$, and $\mathbf{a_3}$. The Miller indices are created for a plane of atoms by

- taking the intercepts of the plane with each basis vector
- taking the reciprocal (inverse) of theses intercepts
- multiplying each reciprocal by the smallest common denominator (in order to have integers and no more fractions)

The obtained integers are grouped in brackets. They are called the Miller indices. Common planes and their Miller indices are shown in Figure B.1

The vectors

$$\mathbf{a_1}* = 2\pi \frac{\mathbf{a_2} \times \mathbf{a_3}}{\mathbf{a_1} \cdot (\mathbf{a_2} \times \mathbf{a_3})}$$

$$\mathbf{a_2}* = 2\pi \frac{\mathbf{a_3} \times \mathbf{a_1}}{\mathbf{a_2} \cdot (\mathbf{a_3} \times \mathbf{a_1})}$$

$$\mathbf{a_3}* = 2\pi \frac{\mathbf{a_1} \times \mathbf{a_2}}{\mathbf{a_3} \cdot (\mathbf{a_1} \times \mathbf{a_2})}$$

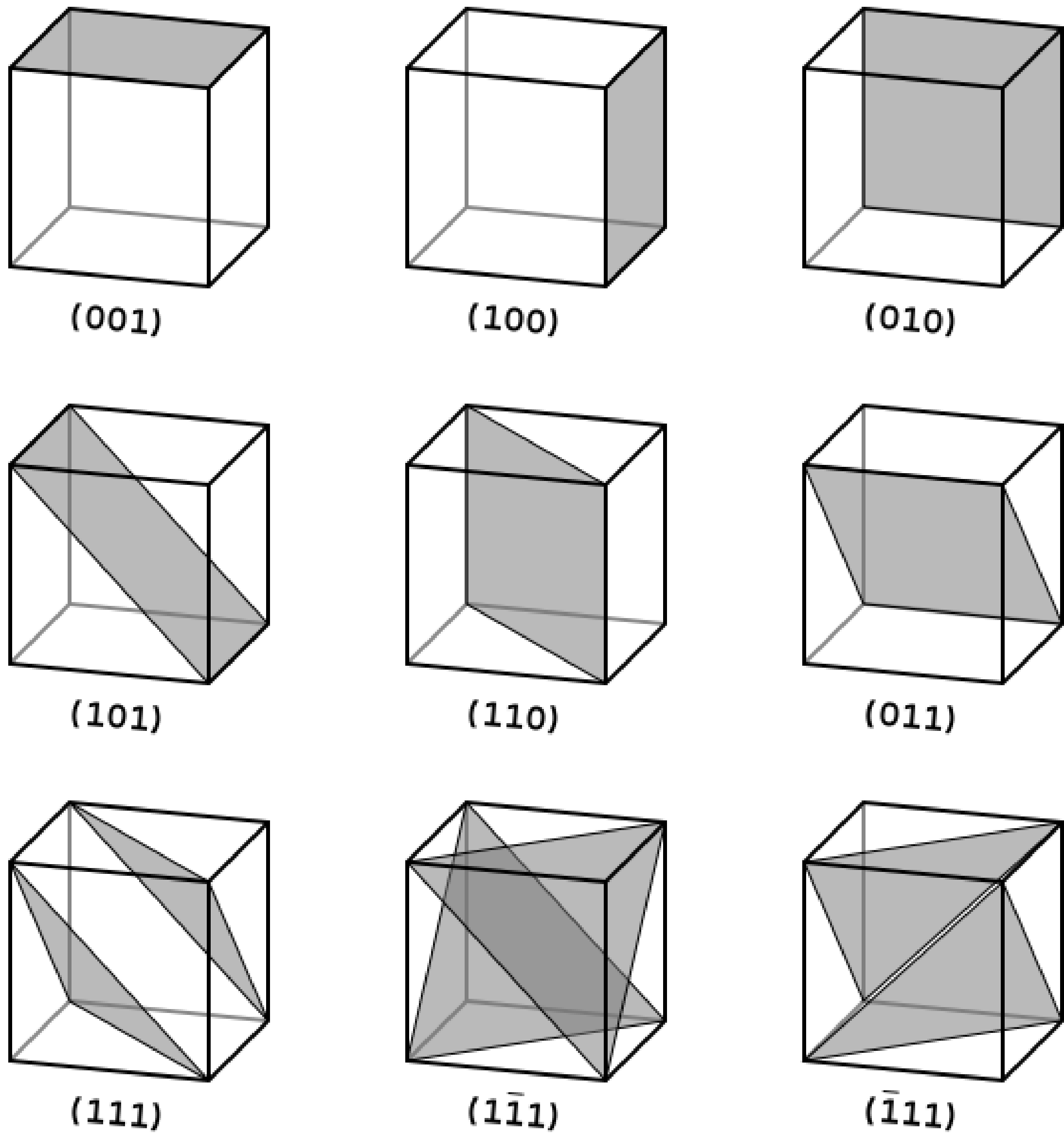


Figure B.1: Common planes and their Miller indices. Source: [90].

define a set of basis vectors for the so-called reciprocal space, satisfying

$$\mathbf{a_i}* \cdot \mathbf{a_j} = 2\pi\delta_{ij} \tag{B.1}$$

where $\delta_{ij}$ is the Kronecker notation, *i.e.* $\forall i, j \in \mathbb{N}, \delta_{ij} = \begin{cases} 1 \text{ if } i = j \\ 0 \text{ otherwise} \end{cases}$

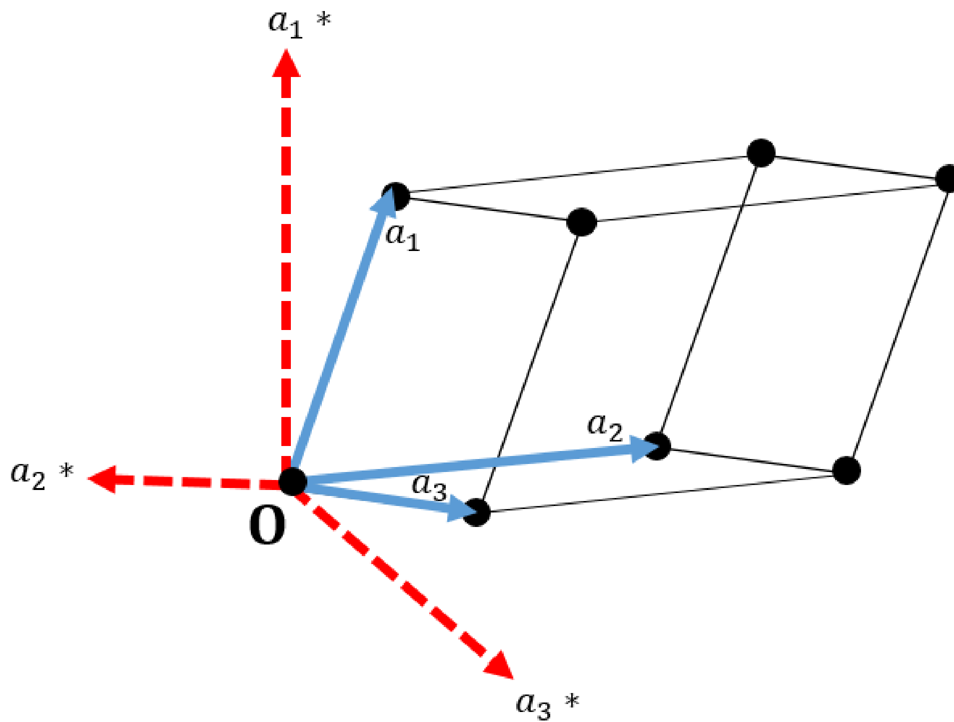


Figure B.2: Representation of the basis vectors of the crystal unit cell $a_i$ and of the reciprocal space $a_i*$.

Hence the reciprocal space lattice vector $h\mathbf{a_1}* + k\mathbf{a_2}* + l\mathbf{a_3}*$ is perpendicular to the real space $(h, k, l)$ plane. For a simple cubic lattice, the distance between two planes is given by:

$$d = \sqrt{\frac{a^2}{h^2 + k^2 + l^2}} \tag{B.2}$$

where $a$ is the lattice parameter (unit cell size).

The reciprocal lattice is made by the reciprocal vectors corresponding to the real planes of the crystal. Every point in this reciprocal lattice hence represents a set of parallel planes in the real space crystal (see Figure B.3).

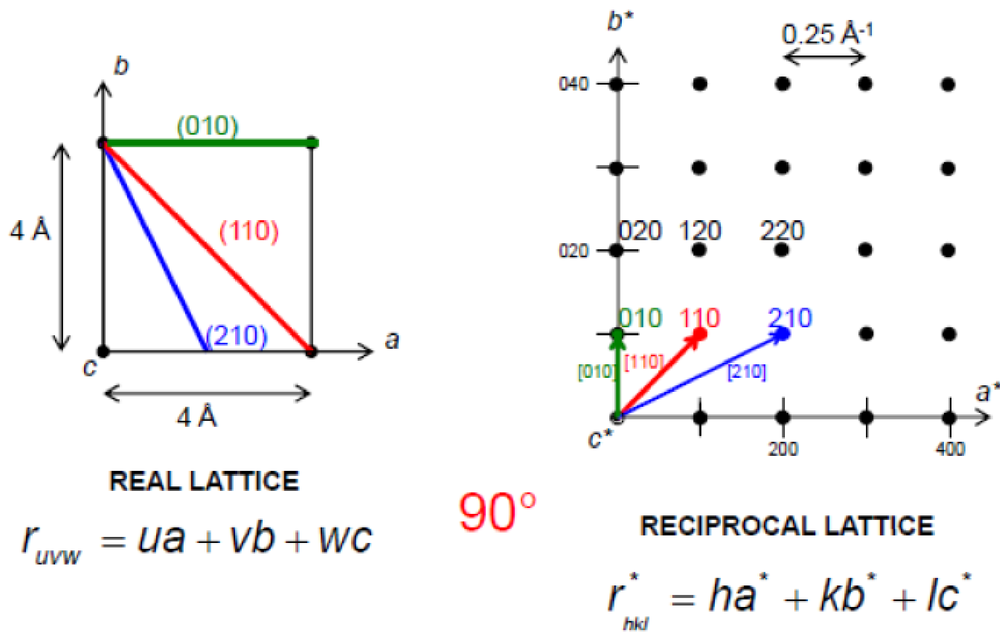


Figure B.3: Real and reciprocal lattice of a cubic structure. Adapted from [91].

# Appendix C

# Ewald sphere and RHEED streaks spacing

The Ewald sphere is a geometrical construction aiming at determining which (real) crystal plane will result in a diffracted signal for a given wavelength $\lambda$. In the case of elastic diffraction (no energy gained or lost during the process), the incident and scattered wave vector have the same length namely $\frac{2\pi}{\lambda}$. The diffracted vector must therefore lie at the surface at a sphere of radius $\frac{2\pi}{\lambda}$ to be observed. This sphere is called the Ewald sphere, from the name of the crystallographer who conceived it. As a geometrical representation, if the origin of the reciprocal space lies at the end of the incident wave vector, only planes whose corresponding point in reciprocal space lies on the sphere's surface will produce a scattered signal.

For RHEED the reciprocal vectors lying on the Ewald sphere and the Fluorescent screen are in a the configuration on Figure C.1.

By geometrical considerations:

$$\frac{g_{\perp}}{\sqrt{(k_0^2 - g_{\perp}^2)}} = \frac{t}{L} \tag{C.1}$$

$g$ being the reciprocal surface vector, $g_{\perp} = 2\pi/d_{\parallel}$ where $d_{\parallel}$ is the interplanar distance for

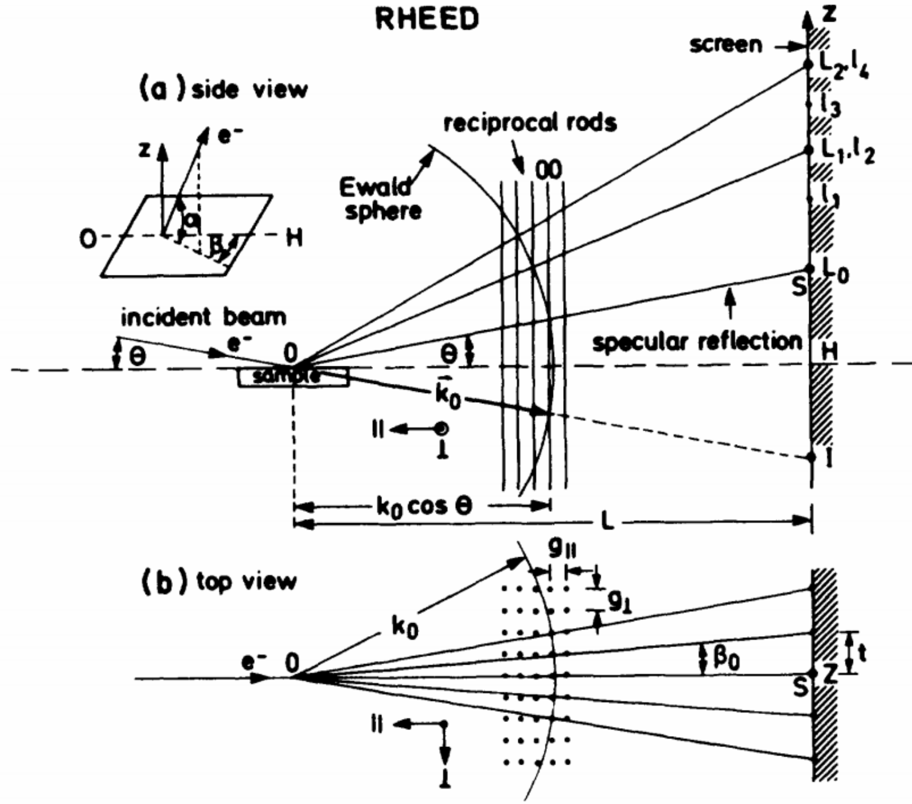


Figure C.1: Schematics of the Ewald sphere and RHEED projection on the fluorescent screen. $k_0$ is the scattered wave vector of length $\frac{2\pi}{\lambda}$, $\theta$ is the angle of the incident beam on the surface, $\beta_0$ is the lateral angle between the diffracted beam and the direct beam (not scattered), $g$ is the reciprocal surface vector, $L$ is the distance between the center of the substrate and the screen and $t$ is the spacing between the scattered streak and the central streak on the screen (streaks spacing). Adapted from [92]

row of atoms parallel to the incident beam. In typical RHEED experiments, $g/k_0 \sim 10^{-2}$ hence $g_{perp} \ll k_0$ and equation C.2 is equivalent to:

$$d_{\perp} = \frac{L * \lambda}{t} \tag{C.2}$$

$\alpha = L\lambda = d_{\perp} * t$ is constant for a given RHEED setup (including the electrons accelerating voltage). Therefore we can conclude that the interplanar spacing is inversely proportional to the spacing between the RHEED streaks. The observation of a known reconstruction, such as $GaAs(001) - (2 \times 4)$ for example, and the measurement of its streaks spacing can therefore allow to determine the value of $\alpha$ and use it to compute the interplanar spacing of other unknown surface configurations from their RHEED pattern. However, these estimations must be realized at constant accelerating voltage since $\lambda$ depends on it. For safety measures, they were recalculated at the beginning of each growth in the experiments reported in this thesis.

# Appendix D

# XRD Calculator

This script computes the lattice parameter of *Al* based on the observed peak position of the *Al* planes in the XRD coupled scan and rocking curve.

Listing D.1: MATLAB script for computing the lattice parameter from the XRD peak position.

```
1  clear all;
2
3  % ---------------------------------------------------------
4  % General declarations
5  % ---------------------------------------------------------
6
7  lambda=1.5406e-10;           %[m] - Xray wavelength (Cu-K-alpha1)
8  a=4.0495e-10;                        %[m] - Lattice parameter of Al
9
10 %Parameters for Bragg's law
11 n_200=2;                                %(200) planes
12 n_220=sqrt(8);                  %(220) planes
13 n_111=sqrt(3);                  %(111) planes
14
15 %Theoretical Bragg angles
16 theta_200_th=22.369;         %(200) planes
17 theta_220_th=32.567;         %(220) planes
```

```
18  theta_111_th=19.236;        %(111) planes
19
20  % ------------------------------------------------------------------
21  % 1 - Al/GaAs(2x4)
22  % ------------------------------------------------------------------
23  theta1_200_m=44.719/2;
24  theta1_220_m=64.992/2;
25
26  a1_200=lambda*n_200/(2*sind(theta1_200_m));
27  a1_220=lambda*n_220/(2*sind(theta1_220_m));
28
29  % ------------------------------------------------------------------
30  % 2 - Al/GaAs(4x4)
31  % ------------------------------------------------------------------
32  %Polycrystalline
33
34  % ------------------------------------------------------------------
35  % 3 - Al/Si(1x1)
36  % ------------------------------------------------------------------
37  theta3_200_m=44.738/2;
38  theta3_111_m=38.429/2;
39
40  a3_200=lambda*n_200/(2*sind(theta3_200_m));
41  a3_111=lambda*n_111/(2*sind(theta3_111_m));
42
43  % ------------------------------------------------------------------
44  % 4 - Al/Si(7x7)
45  % ------------------------------------------------------------------
46  theta4_111_m=19.138;
47
48  a4_111=lambda*n_111/(2*sind(theta4_111_m));
49
50  % ------------------------------------------------------------------
51  % 5 - Al/Si(2x1)
52  % ------------------------------------------------------------------
53  %Bicrystals
```

Follows the Powder Diffraction File for *Al*.

Listing D.2: PDF file for Aluminum.

```
1  PDF#04-0787: QM=Star(S); d=(Unknown); I=Diffractometer
2  Aluminum, syn
3  Al  Light gray metallic
4  Radiation=CuKa1 Lambda=1.54056  Filter=Ni
5  Calibration=    2T=38.472-137.455   I/Ic(RIR)=3.62
6  Ref: Swanson, Tatge.
7  Natl. Bur. Stand. (U.S.), Circ. 539, vI p11 (1953)
8  Cubic - Powder Diffraction,  Fm-3m (225)    Z=4 mp=
9  CELL: 4.0494 x 4.0494 x 4.0494 <90.0 x 90.0 x 90.0> P.S=cF4 (Cu)
10 Density(c)=2.697    Density(m)=2.70A    Mwt=26.98   Vol=66.40   ...
       F(9)=91.8(.0109,9/0)
11 Ref: Ibid.
12
13 Strong Lines: 2.34/X 2.02/5 1.22/2 1.43/2 0.93/1 0.91/1 0.83/1 1.17/1 ...
       1.01/1 0.00/1
14 NOTE:  The material used was a melting point standard sample of ...
       aluminum prepared at NBS, Gaithersburg, Maryland, USA.
15 The chemical analysis (percentage): Si 0.011, Cu 0.006, Fe 0.007, Ti ...
       0.0001, Zr 0.003, Ga 0.004, Mo 0.00002, S 0.0001, Al 99.9+ (by ...
       difference).
16 Pattern taken at 25 C.
17 Mineral species of doubtful validity, Am.
18 Mineral., 65 205 (1980).
19 See ICSD 64700 (PDF 01-085-1327).
20
21 2-Theta    d( )   I(f)   ( h k l)   Theta  1/(2d)   2pi/d  n^2
22  38.472  2.3380  100.0  ( 1 1 1)  19.236  0.2139  2.6874    3
23  44.738  2.0240   47.0  ( 2 0 0)  22.369  0.2470  3.1043    4
24  65.133  1.4310   22.0  ( 2 2 0)  32.567  0.3494  4.3908    8
25  78.227  1.2210   24.0  ( 3 1 1)  39.114  0.4095  5.1459   11
26  82.435  1.1690    7.0  ( 2 2 2)  41.218  0.4277  5.3748   12
27  99.078  1.0124    2.0  ( 4 0 0)  49.539  0.4939  6.2062   16
28 112.041  0.9289    8.0  ( 3 3 1)  56.021  0.5383  6.7641   19
```

```
29 116.569  0.9055    8.0  ( 4 2 0)  58.284  0.5522  6.9389   20
30 137.455  0.8266    8.0  ( 4 2 2)  68.727  0.6049  7.6012   24
```

# References


[1] Peter K. Day, Henry G. LeDuc, Benjamin A. Mazin, Anastasios Vayonakis, and Jonas Zmuidzinas. A broadband superconducting detector suitable for use in large arrays. *Nature*, 425(6960):817–821, 2003. 10.1038/nature02037.

[2] Benjamin A. Mazin, Bruce Bumble, Seth R. Meeker, Kieran O'Brien, Sean McHugh, and Eric Langman. A superconducting focal plane array for ultraviolet, optical, and near-infrared astrophysics. *Optics Express*, 20(2):1503–1511, 2012.

[3] Aaron D. O'Connell, M. Ansmann, R. C. Bialczak, M. Hofheinz, N. Katz, Erik Lucero, C. McKenney, M. Neeley, H. Wang, E. M. Weig, A. N. Cleland, and J. M. Martinis. Microwave dielectric loss at single photon energies and millikelvin temperatures. *Applied Physics Letters*, 92(11):112903, 2008.

[4] A. Megrant, C. Neill, R. Barends, B. Chiaro, Yu Chen, L. Feigl, J. Kelly, Erik Lucero, Matteo Mariantoni, P. J. J. OMalley, D. Sank, A. Vainsencher, J. Wenner, T. C. White, Y. Yin, J. Zhao, C. J. Palmstrom, John M. Martinis, and A. N. Cleland. Planar superconducting resonators with internal quality factors above one million. *Applied Physics Letters*, 100(11):113510, 2012.

[5] D. S. Wisbey, J. Gao, M. R. Vissers, F. C. S. da Silva, J. S. Kline, L. Vale, and D. Pappas. Effect of metal/substrate interfaces on radio-frequency loss in superconducting coplanar waveguides. *J. Appl. Phys.*, 108(093918), 2010.

[6] Sbyrnes321. Schematic of how atoms are arranged in crystalline, polycrystalline, and amorphous matter. http://en.wikipedia.org/wiki/File:Crystalline_polycrystalline_amorphous2.svg. Accessed: 2015-07-20.

[7] Edward Pleshakov. Schematic representation of polycrystalline material consisting of crystallites. http://en.wikipedia.org/wiki/File:Crystallite.jpg. Accessed: 2015-07-20.

[8] Boffrey P. M. Atom by atom, physicists create matter that nature has never known before. *The New York Times*, 1982, June 1.

[9] L. Esaki and R. Tsu. Superlattice and negative differential conductivity in semiconductors. *IBM J. Res. Dev.*, 14(1):61–65, 1970.

[10] L. L. Chang and L. Esaki. Semiconductor superlattices by mbe and their characterization. *Progress in Crystal Growth and Characterization*, 2(0):3–14, 1981.

[11] Cho A. Y. Film deposition by molecular-beam techniques. *Journal of Vacuum Science & Technology B*, 8(5):31–38, 1971.

[12] H. R. Mohebbi and H. Majedi. Cad model for circuit parameters of superconducting-based hybrid planar transmission lines. *Superconductor Science and Technology*, 22(12), 2009.

[13] S.G. Mao and M.Y. Chen. A novel periodic electromagnetic bandgap structure for finite-width conductor-backed coplanar waveguides. *Microwave and Wireless Components Letters, IEEE*, 11(6):261–263, 2001.

[14] G. Ghione. A cad-oriented analytical model for the losses of general asymmetric coplanar lines in hybrid and monolithic mics. *IEE Transactions on Microwave Theory and Techniques*, 41(9):1499–1510, 1993.

[15] Kolasinski K.W. *Surface Science: Foundations of Catalysis and Nanoscience Second Edition*. 2008.

[16] S. Franssila. *Attenuation constant for superconducting coplanar waveguides*. 2001.

[17] R. Barends, J. Kelly, A. Megrant, D. Sank, E. Jeffrey, Y. Chen, Y. Yin, B. Chiaro, J. Mutus, C. Neill, P. OMalley, P. Roushan, J. Wenner, T. C. White, A. N. Cleland, and John M. Martinis. Coherent josephson qubit suitable for scalable quantum integrated circuits. *Physical Review Letters*, 111(8):080502, 2013. PRL.

[18] Ha D.G., Hoo Kim S., Jun S. Y., Bo Shim S., Song W., Hwan Park J., Cho J., and Chong Y. Development of high quality superconducting resonators for quantum device applications, 2013.

[19] D. Pappas. Two level system loss in superconducting microwave resonators. 2011.

[20] John Martinis, S. Nam, J. Aumentado, and C. Urbina. Rabi oscillations in a large josephson-junction qubit. *Physical Review Letters*, 89(11), 2002.

[21] J. A. Venables. *Cleaning and sample preparation*. 2003.

[22] W. G. Schmidt, F. Bechstedt, K. Fleischer, C. Cobet, N. Esser, W. Richter, J. Bernholc, and G. Onida. Gaas(001): Surface structure and optical properties. *Physica status solidi (a)*, 188(4):1401–1409, 2001.

[23] Y. Fukaya, M. Maekawa, A. Kawasuso, I. Mochizuki, K. Wada, T. Shidara, A. Ichimiya, and T. Hyodo. Total reflection high-energy positron diffraction (trhepd) - an ideal diffraction technique for surface structure analysis. *Applied Physics Express*, 7(5):056601, 2014.

[24] J.E. Quinn. *LEED Studies of Atomic Structures of* $Si(111)-\sqrt{3x3}-30$ *metal Surface Phases*. PhD thesis, State University of New York, 1992.

[25] K Takayanagi, Y. Tanishiro, M. Takahashi, and S. Takahashi. Structural analysis of si(111)7x7 by uhvtransmission electron diffraction and microscopy. *Journal of Vacuum Science and Technology A*, 3(3):1502–1506, 1985.

[26] G. Binnig, H. Rohrer, Ch Gerber, and E. Weibel. 7x7 reconstruction on si(111) resolved in real space. *Phys. Rev. Letters*, 50(2):120–123, 1983.

[27] Karl D. Brommer, M. Needels, B. Larson, and J. D. Joannopoulos. Ab initio theory of the si(111)-(7x7) surface reconstruction: A challenge for massively parallel computation. *Phys. Rev. Lett.*, 68:1355–1358, Mar 1992.

[28] A. Zur and T. C. McGill. Lattice match: An application to heteroepitaxy. *Journal of Applied Physics*, 55(2):378–386, 1984.

[29] D. Keith Bowen and B. K. Tanner. *High Resolution X-ray diffractometry and topography.* Taylor and Francis, 2005.

[30] L. J. Brillson, M. L. Slade, A. D. Katnani, M. Kelly, and G. Margaritondo. Reduction of silicon aluminum interdiffusion by improved semiconductor surface ordering. *Applied Physics Letters*, 44(1):110–112, 1984.

[31] H. F. Liu, S. J. Chua, and N. Xiang. Growth-temperature- and thermal-anneal-induced crystalline reorientation of aluminum on gaas (100) grown by molecular beam epitaxy. *Journal of Applied Physics*, 101(5):–, 2007.

[32] F. K. Legoues, W. Krakow, and P. S. Ho. Atomic structure of the epitaxial alsi interface. *Philosophical Magazine A*, 53(6):833–841, 1986.

[33] F. C. Nix and D. MacNair. The thermal expansion of pure metals: copper, gold, aluminum, nickel and iron. *Physical Review*, 60(8):597–605, 1941.

[34] S.I. Novikova. A study of thermal expansion of gaas and znse. *Soviet Physics Solid State*, 3, 1961.

[35] Y. Okada and Y. Tokumaru. Precise determination of lattice parameter and thermal expansion coefficient of silicon between 300k and 1500k. *Journal of Applied Physics*, 56(2):314–320, 1984.

[36] W. Kern and D. A. Puotinen. Cleaning solutions based on hydrogen peroxide for use in silicon semiconductor technology. *RCA Review*, 31:187–206, 1970.

[37] W. Kern. Evolution of wafer cleaning technology. *Journal of Electrochemical Society*, 137(6), 1990.

[38] John R. Vig. Uv/ozone cleaning of surfaces. *Journal of Vacuum Science & Technology A*, 3(3):1027–1034, 1985.

[39] Akitoshi Ishizaka and Yasuhiro Shiraki. Low temperature surface cleaning of silicon and its application to silicon mbe. *Journal of The Electrochemical Society*, 133(4):666–671, 1986.

[40] T. J. Lander and J. Morrison. Low voltage electron diffraction study of the oxidation and reduction of silicon. *Applied Physics Letters*, 33:2089, 1962.

[41] E. Kasper, M. Bauer, and M. Oehme. Quantitative secondary ion mass spectrometry analysis of $sio_2$ desorption during in situ heat cleaning. *Thin Solid Films*, 321(12):148–152, 1998.

[42] H. Miki, K. Sakamoto, and T. Sakamoto. Surface preparation of si substrates for epitaxial growth. *Surface Science*, 406:312–327, 1998.

[43] S. Wright and H. Kroemer. Reduction of oxides on silicon by heating in a gallium molecular beam at 800°c. *Applied Physics Letters*, 36(3):210–211, 1980.

[44] H. T. Yang and P.M. Mooney. The characterization of indium desorbed si surfaces for low temperature surface cleaning in si molecular beam epitaxy. *Journal of Applied Physics*, 58(5):1854–1859, 1985.

[45] J. Castagne, E. Bedel, C. Fontaine, and A. Munoz-Yague. Si-substrate preparation for gaas/si molecular-beam epitaxy at low temperature under a si flux. *Journal of Applied Physics*, 64(1):246, 1988.

[46] M. S. Carroll, J. C. Sturm, and M. Yang. Lowtemperature preparation of oxygen and carbonfree silicon and silicongermanium surfaces for silicon and silicongermanium epitaxial growth by rapid thermal chemical vapor deposition. *Journal of The Electrochemical Society*, 147(12):4652–4659, 2000. 10.1149/1.1394118.

[47] K. Madiomanana, M. Bahri, J. B. Rodriguez, L. Largeau, L. Cerutti, O. Mauguin, A. Castellano, G. Patriarche, and E. Tourni. Silicon surface preparation for iii-v molecular beam epitaxy. *Journal of Crystal Growth*, 413(0):17–24, 2015.

[48] J. Ramm, E. Beck, A. Zueger, A. Dommann, and R.E. Pixley. Hydrogen cleaning of silicon wafers. investigation of the wafer surface after plasma treatment. *Thin Solid Films*, 228:23–26, 1993.

[49] N. Korner, E. Beck, A. Dommann, N. Onda, and J. Ramm. Hydrogen plasma chemical cleaning of metallic substrates and silicon wafers. *Surface and Coatings Technology*, 76:731–737, 1995.

[50] J. Ramm, E. Beck, A. Zuger, A. Dommann, and R.E. Pixley. Low-temperature in situ cleaning of silicon wafers with an ultra high vacuum compatible plasma source. *Thin Solid Films*, 222:126–131, 1992.

[51] M. Sobanska, K. Klosek, Z. R. Zytkiewicz, J. Borysiuk, B. S. Witkowski, E. Lusakowska, A. Reszka, and R. Jakiela. Plasma-assisted mbe growth of gan on si(111) substrates. *Crystal Research and Technology*, 47(3):307–312, 2012.

[52] R. Ludeke, L. L. Chang, and L. Esaki. Molecular beam epitaxy of alternating metalsemiconductor films. *Applied Physics Letters*, 23(4):201–203, 1973.

[53] G. Landgren, R. Ludeke, and C. Serrano. Epitaxial a1 films on gaas(100) surfaces. *Journal of Crystal Growth*, 60(2):393–402, 1982.

[54] A. Y. Cho and P. D. Dernier. Singlecrystalaluminum schottkybarrier diodes prepared by molecularbeam epitaxy (mbe) on gaas. *Journal of Applied Physics*, 49(6):3328–3332, 1978.

[55] C. Barret and J. Massies. On the dependence of schottky barrier height and interface states upon initial semiconductor surface parameters in gaas(001)/al junctions. *Journal of Vacuum Science & Technology B*, 1(3):819–824, 1983.

[56] M. Missous, E. H. Rhoderick, and K. E. Singer. Thermal stability of epitaxial al/gaas schottky barriers prepared by molecularbeam epitaxy. *Journal of Applied Physics*, 59(9):3189–3195, 1986.

[57] J. Massies, J. Chaplart, and N. T. Linh. New results in the study of the aluminium epitaxial growth on gallium arsenide (001). *Solid State Communications*, 32(8):707–709, 1979.

[58] S. J. Pilkington and M. Missous. The growth of epitaxial aluminium on as containing compound semiconductors. *Journal of Crystal Growth*, 196(1):1–12, 1999.

[59] S. K. Donner, Rik Blumenthal, J. L. Herman, Rajender Trehan, Ehud Furman, and Nicholas Winograd. Growth of al on gaas(001): Observation of interfacial submonolayer structure. *Applied Physics Letters*, 55(17):1753–1755, 1989.

[60] G. A. Prinz, J. M. Ferrari, and M. Goldenberg. Molecular beam epitaxial growth of singlecrystal al films on gaas (110). *Applied Physics Letters*, 40(2):155–157, 1982.

[61] J. E. Oh, P. K. Bhattacharya, J. Singh, W. Dos Passos, R. Clarke, N. Mestres, R. Merlin, K. H. Chang, and R. Gibala. Epitaxial growth and characterization of gaas/al/gaas heterostructures. *Surface Science*, 228(13):16–19, 1990.

[62] Lin Shi-Wei, Wu Jau-Yang, Lin Sheng-Di, Lo Ming-Cheng, Lin Ming-Huei, and Liang Chi-Te. Characterization of single-crystalline aluminum thin film on (100) gaas substrate. *Japanese Journal of Applied Physics*, 52(4R):045801, 2013.

[63] M. Missous, E. H. Rhoderick, and K. E. Singer. The effects of vacuum conditions on epitaxial al/gaas contacts formed by molecularbeam epitaxy. *Journal of Applied Physics*, 60(7):2439–2444, 1986.

[64] P. M. Petroff, L. C. Feldman, A. Y. Cho, and R. S. Williams. Properties of aluminum epitaxial growth on gaas. *Journal of Applied Physics*, 52(12):7317–7320, 1981.

[65] M. V. Lovygin, N. I. Borgardt, I. P. Kazakov, and M. Seibt. Electron microscopy of an aluminum layer grown on the vicinal surface of a gallium arsenide substrate. *Semiconductors*, 49(3):337–344, 2015.

[66] F. dHeurle, L. Berenbaum, and Rosenberg R. On the structure of aluminum films. *Transactions of the Metallurgical Society of AIME*, 242:502, 1968.

[67] I. Yamada, H. Inokawa, and T. Takagi. Epitaxial growth of al on si(111) and si(100) by ionizedcluster beam. *Journal of Applied Physics*, 56(10):2746–2750, 1984.

[68] M. A. Hasan, G Radnoczi, Sundgren J.-E, and Hansson G.V. Epitaxial growth of al on si by thermal evaporation in ultra-high vacuum growth on si 2x1 single and double domain surfaces at room temperature. *Surface Science*, 236:53–76, 1990.

[69] A. W. Fortuin, P. F. A. Alkemade, A. H. Verbruggen, A. J. Steinfort, H. Zandbergen, and S. Radelaar. Characterization of single-crystalline al films grown on si(111). *Surface Science*, 366(2):285–294, 1996.

[70] M. F. Doerner and S. Brennan. Strain distribution in thin aluminum films using x-ray depth profiling. *Journal of Applied Physics*, 63(1):126, 1988.

[71] Y. Miura, S. Fujieda, and K. Hirose. Singlecrystal al growth on si(111) by lowtemperature molecular beam epitaxy. *Applied Physics Letters*, 62(15):1751–1753, 1993.

[72] Hong Liu, Y. F. Zhang, D. Y. Wang, M. H. Pan, J. F. Jia, and Q. K. Xue. Two-dimensional growth of al films on si(111)-7x7 at low-temperature. *Surface Science*, 571(13):5–11, 2004.

[73] Zhenyu Zhang, Qian Niu, and Chih-Kang Shih. "electronic growth" of metallic overlayers on semiconductor substrates. *Physical Review Letters*, 80(24):5381–5384, 1998. PRL.

[74] Marek Sosnowski, Samuel Ramac, Walter L. Brown, and Young O. Kim. Importance of steps in heteroepitaxy: The case of aluminum on silicon. *Applied Physics Letters*, 65(23):2943–2945, 1994.

[75] Herman M.A. and Sitter H. *Molecular Beam Epitaxy fundamentals and current status.* 2012.

[76] J. Tsao. *Material Fundamentals of Molecular Beam Epitaxy.* Academic Press, 2012.

[77] R.F.C. Farrow. *Molecular Beam Epitaxy: Application to key materials.* Elsevier Science, 2012.

[78] M. Henini. *Molecular Beam Epitaxy: from research to Mass Production.* Newnes, 2012.

[79] Z. R. Wasilewski, G. C. Aers, A. J. SpringThorpe, and C. J. Miner. Studies and modeling of growth uniformity in molecular beam epitaxy. *Journal of Vacuum Science and Technology B*, 9(1):120–131, 1991.

[80] Nikhil P. Concept drawing of a molecular beam epitaxy growth chamber. http://commons.wikimedia.org/wiki/File:Molecular_Beam_Epitaxy.png. Accessed: 2015-07-20.

[81] Truscott W. S. Chilton P. A. and Wen Y. F. Elimination of the flux transients from molecular beam epitaxy source cells following shutter operation. *Journal of Vacuum Science & Technology B*, 6(4):1099–1104, 1988.

[82] Harris J. J., Joyce B., and Dobson P. J. Oscillations in the surface structure of sn-doped gaas during growth by mbe. *Surface Science*, 103(1):90–96, 1981.

[83] D. Keith Bowen and B. K. Tanner. *X-ray metrology in semiconductor manufacturing.* CRC Press, 2006.

[84] B. D. Cullity. *Elements of X-ray diffraction, 3rd edition.* Upper Saddle River Prentice Hall, 2001.

[85] OverlordQ. Atomic force microscope block diagram. http://commons.wikimedia.org/wiki/File:Atomic_force_microscope_block_diagram.svg. Accessed: 2015-07-20.

[86] P. Pianetta, I. Lindau, C. M. Garner, and W. E. Spicer. Oxidation properties of gaas (110) surfaces. *Physical Review Letters*, 37(17):1166–1169, 1976.

[87] R. J. Archer and G. W. Gobeli. Measurement of oxygen adsorption on silicon by ellipsometry. *Journal of Physics and Chemistry of Solids*, 26(2):343–351, 1965.

[88] V. P. LaBella, H. Yang, D. W. Bullock, P. M. Thibado, Peter Kratzer, and Matthias Scheffler. Atomic structure of the GaAs$(001)-(2\times4)$ surface resolved using scanning

tunneling microscopy and first-principles theory. *Phys. Rev. Lett.*, 83:2989–2992, Oct 1999.

[89] R. Ludeke. Interface behavior and crystallographic relationships of aluminum on gaas(100) surfaces. *Journal of Vacuum Science and Technology*, 19(3):667, 1981.

[90] McSush. Example of crystallographic planes and miller indices for a cubic structure. https://commons.wikimedia.org/wiki/File:Miller_Indices_Cubes.svg. Accessed: 2015-07-20.

[91] R. J. D. Tilley. *Lattice planes and directions.* 2006.

[92] I. Hernandez-Calderon and H. Hochst. New method for the analysis of reflection high energy electron diffraction: $\alpha$-sn(001) and insb(001) surfaces. *Physical Review B*, 27(8):4961–4965, 1983.